



**This electronic thesis or dissertation has been  
downloaded from Explore Bristol Research,  
<http://research-information.bristol.ac.uk>**

*Author:*

**Araiza Illan, Gloria A**

*Title:*

**Model-based Transcutaneous Electrical Nerve Stimulation for Tactile Sensations**

**General rights**

Access to the thesis is subject to the Creative Commons Attribution - NonCommercial-No Derivatives 4.0 International Public License. A copy of this may be found at <https://creativecommons.org/licenses/by-nc-nd/4.0/legalcode>. This license sets out your rights and the restrictions that apply to your access to the thesis so it is important you read this before proceeding.

**Take down policy**

Some pages of this thesis may have been removed for copyright restrictions prior to having it been deposited in Explore Bristol Research. However, if you have discovered material within the thesis that you consider to be unlawful e.g. breaches of copyright (either yours or that of a third party) or any other law, including but not limited to those relating to patent, trademark, confidentiality, data protection, obscenity, defamation, libel, then please contact [collections-metadata@bristol.ac.uk](mailto:collections-metadata@bristol.ac.uk) and include the following information in your message:

- Your contact details
- Bibliographic details for the item, including a URL
- An outline nature of the complaint

Your claim will be investigated and, where appropriate, the item in question will be removed from public view as soon as possible.

---

---

# Model-based Transcutaneous Electrical Nerve Stimulation for Tactile Sensations

---

---

By

GLORIA ALEJANDRA ARAIZA ILLAN



Department of Aerospace  
UNIVERSITY OF BRISTOL

A dissertation submitted to the University of Bristol in accordance with the requirements of the degree of DOCTOR OF PHILOSOPHY IN ROBOTICS in the Faculty of Engineering.

SEPTEMBER 2019

Word count: twenty-three thousand, seven hundred and four



## ABSTRACT

In this work, a transcutaneous electrical nerve stimulation system for a human finger was developed and compared to a mechanical stimulation system in both a simulated environment and through psychophysical tests using the respective hardware implementations to evaluate the similarity of the resulting tactile sensations. It was observed that the selective stimulation of fibres located at different depths (modelled as one shallower and one deeper fibre) is directly dependent on the TENS design, particularly on the excitation patterns given by the individual electrode currents, which has not been documented in literature.

The simulation environment allowed the design of particular electrical stimulation patterns for an eight electrode array. These stimuli belonged to two classes, one designed to selectively stimulate a shallower fibre (representing one SA1 fibre) and the other designed to selectively stimulate a deeper fibre (representing one PC fibre). The stimuli were tested using the hardware implementation of the TENS system, resulting in the participants showing a better performance in the psychophysical tests when discriminating between classes than within classes in two of the three tested frequencies (10 and 50 Hz). This shows that different tactile sensations were perceived when using the designed classes of stimuli.



## DEDICATION AND ACKNOWLEDGEMENTS

**T**o my previous self, who had enough faith in her future self to close cycles.

I would like to express my gratitude to all of my supervisors, friends and family, who supported and advised me whenever I required guidance. I would also like to give special mention to Ian Horsfield, whose kindness will never be forgotten; to Jennifer Riley, who offered me her home when I surely needed it; and to all the Samba family, who kept me sane for the last four years.



## AUTHOR'S DECLARATION

I declare that the work in this dissertation was carried out in accordance with the requirements of the University's Regulations and Code of Practice for Research Degree Programmes and that it has not been submitted for any other academic award. Except where indicated by specific reference in the text, the work is the candidate's own work. Work done in collaboration with, or with the assistance of, others, is indicated as such. Any views expressed in the dissertation are those of the author.

SIGNED: ..... DATE: .....





## TABLE OF CONTENTS

	<b>Page</b>
<b>List of Tables</b>	<b>xi</b>
<b>List of Figures</b>	<b>xiii</b>
<b>1 Introduction</b>	<b>1</b>
<b>2 Simulation Environment for a TENS System</b>	<b>5</b>
2.1 Tactile Sensations . . . . .	5
2.1.1 Anatomy and Physiology of the Tactile Sensations . . . . .	6
2.2 Modelling Neurons . . . . .	9
2.2.1 Excitation Models . . . . .	9
2.3 TENS Simulation Models . . . . .	11
2.4 Materials and Methods . . . . .	12
2.4.1 Electrical Field Model . . . . .	12
2.4.2 Nerve Response Model . . . . .	15
2.5 Results . . . . .	20
2.5.1 Overall Validation of Simulation Environment . . . . .	20
2.5.2 Selective Stimulation . . . . .	22
2.6 Discussion . . . . .	34
2.7 Conclusion . . . . .	38
<b>3 Hardware of TENS Systems</b>	<b>39</b>
3.1 Tactile Displays . . . . .	39
3.2 Design and Implementation of the Hardware for the Modelled TENS System . . . . .	44
3.2.1 Digital-to-Analog Converter Channels . . . . .	45
3.2.2 Voltage-to-Current Converter . . . . .	47
3.2.3 Board Design of the Power Supply . . . . .	54
3.2.4 Electrode Design . . . . .	55
<b>4 Psychophysical Experiments Using the TENS System</b>	<b>59</b>
4.1 Psychophysics . . . . .	59

## TABLE OF CONTENTS

---

4.2	Signal Detection Theory . . . . .	60
4.3	Materials and Methods - Psychophysical Experiments . . . . .	62
4.3.1	Current Calibration . . . . .	62
4.3.2	Saturation . . . . .	64
4.3.3	Same-Different Paired Comparison . . . . .	64
4.4	Results . . . . .	66
4.4.1	Saturation Test . . . . .	67
4.4.2	Discrimination Between all Presented Stimuli . . . . .	67
4.4.3	Discrimination Between Stimuli Classes . . . . .	71
4.4.4	Discrimination Within Stimuli Classes . . . . .	72
4.5	Discussion . . . . .	75
4.6	Conclusion . . . . .	79
<b>5</b>	<b>Comparison Between Electrical and Mechanical Stimulation Simulation Environments</b>	<b>81</b>
5.1	Mechanical Stimulation Simulation Environment . . . . .	81
5.2	Spike Train Metrics . . . . .	83
5.3	Materials and Methods . . . . .	85
5.3.1	MS Simulation Environment Implementation . . . . .	85
5.3.2	Spike Train Comparison Using GVP Metric . . . . .	87
5.4	Results . . . . .	91
5.4.1	Verification of the MS Simulation Environment Implementation . . . . .	91
5.4.2	Spike Train Comparison . . . . .	94
5.5	Discussion . . . . .	97
5.6	Conclusion . . . . .	98
<b>6</b>	<b>Comparison Between Electrical and Mechanical Stimulation Hardware Systems</b>	<b>99</b>
6.1	Materials and Methods . . . . .	100
6.1.1	Mechanical Stimulators . . . . .	100
6.1.2	Hardware Characterisation . . . . .	102
6.1.3	Method of Triads . . . . .	103
6.2	Results . . . . .	105
6.2.1	Hardware Characterisation . . . . .	105
6.2.2	Method of Triads . . . . .	107
6.3	Discussion . . . . .	112
6.4	Conclusion . . . . .	114
<b>7</b>	<b>Conclusions</b>	<b>117</b>

7.1 Future Work . . . . .	118
<b>A Hardware Schematics and Ethical Approval</b>	<b>121</b>
<b>References</b>	<b>129</b>



## LIST OF TABLES

TABLE	Page
2.1 Dimensions used in the finger FEM [84]. . . . .	13
2.2 Conductivity values of the human finger [29, 30]. . . . .	13
2.3 Variables for the electrical network representation of a myelinated fibre. . .	15
2.4 HH model parameters for human nerve fibres [25, 70, 80, 102, 103]. . . . .	16
2.5 HH model parameters for human nerve fibres [80]. . . . .	16
3.1 Resistor values used in the amplifier circuit. . . . .	47
3.2 Resistor values used in the VI circuit. . . . .	53
4.1 Electrode currents for the selected ES (all shown in mA). . . . .	63
4.2 Timing of all six saturation tests. . . . .	64
4.3 Set of 24 pairs used for the same-different paired comparison. . . . .	66
4.4 "Same" pairs for discrimination between all stimuli. . . . .	68
4.5 "Different" pairs for discrimination between all stimuli. . . . .	68
4.6 Signal detection model parameters from discriminating between all stimuli.	68
4.7 "Different" pairs for discrimination between stimuli classes. . . . .	71
4.8 Signal detection model parameters from discriminating between stimuli classes. . . . .	71
4.9 "Different" pairs for discrimination within stimuli classes. . . . .	72
4.10 Signal detection model parameters from discriminating within stimuli classes.	72
5.1 Parameters of the mechanical stimuli set for the modelled SA1 fibre ( $MS_{SA1}$ ). 86	86
5.2 Parameters of the mechanical stimuli set for the modelled PC fibre ( $MS_{PC}$ ). 87	87
5.3 Electrode currents for the set $ES_s$ (all shown in mA). . . . .	89
5.4 Electrode currents for the set $ES_d$ (all shown in mA). . . . .	90
5.5 Mechanical stimuli used to test the modelled SA1 fibre response. . . . .	91
5.6 Mechanical stimuli used to test the modelled PC fibre response. . . . .	91
5.7 Fittest pairs of MS and ES when matching $MS_{SA1}$ to $ES_s$ . . . . .	94
5.8 Fittest pairs of MS and ES when matching $MS_{PC}$ to $ES_d$ . . . . .	95

<b>6.1</b>	<b>Parameters of the selected pairs of mechanical and electrical stimuli to use in the method of triads. . . . .</b>	<b>104</b>
<b>6.2</b>	<b>Triads with answer "one" for discrimination between stimuli classes. . . . .</b>	<b>108</b>
<b>6.3</b>	<b>Triads with answer "two" for discrimination between stimuli classes. . . . .</b>	<b>109</b>
<b>6.4</b>	<b>Signal detection model parameters from discriminating between stimuli classes. . . . .</b>	<b>109</b>
<b>6.5</b>	<b>"One" triads for discrimination of true stimuli pairs. . . . .</b>	<b>110</b>
<b>6.6</b>	<b>"Two" triads for discrimination of true stimuli pairs. . . . .</b>	<b>112</b>
<b>6.7</b>	<b>Signal detection model parameters from discriminating the true stimuli pairs. . . . .</b>	<b>112</b>

## LIST OF FIGURES

FIGURE	Page
1.1 Project overview comprising the comparison of both mechanical and electrical stimulation systems. . . . .	3
2.1 Cutaneous somatosensory receptors in mammals. Receptors can be RA rapidly adapting or SA slowly adapting, with a low threshold (LT) or a high one (HT). Taken from [14]. . . . .	7
2.2 Typical action potential. Taken from [26]. . . . .	8
2.3 Physiologic classifications and functions of nerve fibres. Taken from [26]. . . . .	10
2.4 FEM developed for a human finger with an 8-electrode array located on the finger pad. A drawing of a real finger is shown at top left, with its pad on the electrode array. At top right is shown a simplified model of the finger, used to develop the FEM illustrated at bottom right (with the finger inverted to show the electrode array on the finger pad). One example of the currents flowing from array to finger is indicated in the top left image and also shown in the graph at bottom left, in which the horizontal axis represents distance along the nerve fibre, running from the fingertip towards the CNS. Taken from [2], used with permission under Creative Commons license. . . . .	14
2.5 Electrical network representation of a myelinated fibre. Taken from [2], used with permission under Creative Commons license. . . . .	15
2.6 ES simulation of a nerve fibre located at 1.5 mm depth using two electrodes, 1 ms after stimulus onset. (a) corresponds to the electrode currents, (b) to the extracellular potential $V_{e,n}$ and (c) to the membrane potential $V_n$ with depth $z = 1.5$ mm. . . . .	22
2.7 ES simulation of a nerve fibre located at 1.5 mm depth using eight electrodes, 1 ms after stimulus onset. (a) corresponds to the electrode currents, (b) to the extracellular potential $V_{e,n}$ and (c) to the membrane potential $V_n$ with depth $z = 1.5$ mm. . . . .	23
2.8 Distribution of the superficial corial plexus, divided into a part with perpendicular orientation that supplies Meissner corpuscles and a second part with parallel orientation that supplies Merkel discs. Taken from [9]. . . . .	24



2.9 Anodic ES simulation of a nerve fibre running parallel to the skin at 1.5 mm depth ( $N_1$ ) and a nerve fibre running perpendicular from 1 to 1.5 mm depth and then parallel to the skin at 1.5 mm depth ( $N_2$ ) at 1 ms after stimulus onset. (a) corresponds to the electrode currents, (b) and (c) to the extracellular potentials  $V_{e,n}$  and (d) and (e) to the membrane potentials  $V_n$  as functions of distance (millimetres). Figure shows the efficient depolarisation of  $N_2$  and inhibition of  $N_1$ . In panels (b), (c), (d) and (e), the horizontal axis represents distance along the nerve, for  $N_1$  shown in (b) and (d), distance along the nerve corresponds to distance along the skin, as in panel (a); but for  $N_2$  in panels (c) and (e), which originates under the 4th electrode and runs first perpendicular to and then parallel to the skin, distance along the nerve is offset with respect to distance along the skin in (a). . . . . 26

2.10 Anodic ES simulation of a nerve fibre running parallel to the skin at 1.5 mm depth ( $N_1$ ) and a nerve fibre running perpendicular from 1 to 1.5 mm depth and then parallel to the skin at 1.5 mm depth ( $N_2$ ) showing the responses through time. (a) shows the lack of an action potential in the membrane potential  $V_n$  of  $N_1$  (hence considered inhibited). (b) corresponds to the membrane potential  $V_n$  of  $N_2$ , highlighting the excitation and travelling of the spike towards the end of the modelled nerve fibre (propagating towards the CNS, thus considered activated). . . . . 27

2.11 Anodic ES simulation of a nerve fibre running parallel to the skin at 1.5 mm depth ( $N_1$ ) and a nerve fibre running perpendicular from 1 to 1.5 mm depth and then parallel to the skin at 1.5 mm depth ( $N_2$ ) showing the response of the fibres in the last node (end towards the CNS) through time. (a) shows the lack of an action potential in the last node of the membrane potential  $V_n$  of  $N_1$  (hence considered inhibited). (b) corresponds to the membrane potential  $V_n$  of the last node of  $N_2$ , where the shape of the action potential is shown, thus indicating the activation of the fibre due to the propagation of the spike towards the CNS. . . . . 27

2.12 Cathodic ES simulation of a nerve fibre running parallel to the skin at 1.5 mm depth ( $N_1$ ) and a nerve fibre running perpendicular from 1 to 1.5 mm depth and then parallel to the skin at 1.5 mm depth ( $N_2$ ) at 1 ms after stimulus onset. (a) corresponds to the electrode currents, (b) and (c) to the extracellular potentials  $V_{e,n}$  and (d) and (e) to the membrane potentials  $V_n$  as functions of distance (millimetres). Figure shows the depolarisation of  $N_1$  and  $N_2$ . In panels (b), (c), (d) and (e), the horizontal axis represents distance along the nerve, for  $N_1$  shown in (b) and (d), distance along the nerve corresponds to distance along the skin, as in panel (a); but for  $N_2$  in panels (c) and (e), which originates under the 4th electrode and runs first perpendicular to and then parallel to the skin, distance along the nerve is offset with respect to distance along the skin in (a). . . . . 28

- 2.13 Cathodic ES simulation of a nerve fibre running parallel to the skin at 1.5 mm depth ( $N_1$ ) and a nerve fibre running perpendicular from 1 to 1.5 mm depth and then parallel to the skin at 1.5 mm depth ( $N_2$ ) showing the responses through time. (a) corresponds to the membrane potential  $V_n$  of  $N_1$  and (b) to the membrane potential  $V_n$  of  $N_2$ . The excitations and the traveling of the spikes towards the end of both nerve fibres (towards the CNS, hence considered activated) are highlighted. . . . . 29
- 2.14 Cathodic ES simulation of a nerve fibre running parallel to the skin at 1.5 mm depth ( $N_1$ ) and a nerve fibre running perpendicular from 1 to 1.5 mm depth and then parallel to the skin at 1.5 mm depth ( $N_2$ ) showing the responses of the fibres in the last node (end towards the CNS) through time. (a) corresponds to the membrane potential  $V_n$  of the last node of  $N_1$  and (b) to the membrane potential  $V_n$  of the last node of  $N_2$ . In both panels it can be seen an action potential, which denotes the activation of the fibres. 29
- 2.15 First example of selective stimulation of the shallower nerve fibre  $N_1$ . (a) shows the electrode currents. (b) and (c) illustrate the membrane potential  $V_n$  of  $N_1$  and  $N_3$ , respectively, 1 ms after stimulus onset. (d) and (e) correspond to the time courses of the excitations; it can be seen (region indicated by dotted lines) that an excitation (shown in red) propagates towards the nerve ending (CNS) in  $N_1$  (thus considered activated), as shown in (d), but not in  $N_3$  illustrated in (e) (thus considered inhibited). 31
- 2.16 Second example of selective stimulation of the shallower nerve fibre  $N_1$ . (a) shows the electrode currents. (b) and (c) illustrate the membrane potential  $V_n$  of  $N_1$  and  $N_3$ , respectively, 1 ms after stimulus onset. (d) and (e) correspond to the time courses of the excitations; it is shown in the region indicated by dotted lines in (d), that an excitation (shown in red) propagates towards the nerve ending (CNS) in  $N_1$  (thus considered activated), but not in  $N_3$ , illustrated in (e) (thus considered inhibited). . . 32
- 2.17 Third example of selective stimulation of the shallower nerve fibre  $N_1$ . (a) shows the electrode currents. (b) and (c) illustrate the membrane potential  $V_n$  of  $N_1$  and  $N_3$ , respectively, 1 ms after stimulus onset. (d) and (e) correspond to the time courses of the excitations; the region indicated by dotted lines in (d) demonstrates that an excitation (shown in red) propagates towards the nerve ending (CNS) in  $N_1$  (thus considered activated), but not in  $N_3$ , illustrated in (e) (thus considered inhibited). . . 33
- 2.18 First example of selective stimulation of the deeper nerve fibre  $N_3$ . (a) shows the electrode currents. (b) and (c) illustrate the membrane potential  $V_n$  of  $N_1$  and  $N_3$ , respectively, 1 ms after stimulus onset. (d) and (e) correspond to the time courses of the excitations; it can be seen (region indicated by dotted lines) that an excitation (shown in red) propagates towards the nerve ending (CNS) in  $N_3$  as shown in (e) (thus considered activated), but not in  $N_1$  illustrated in (d) (thus considered inhibited). . . 35

2.19	Second example of selective stimulation of the deeper nerve fibre $N_3$ . (a) shows the electrode currents. (b) and (c) illustrate the membrane potential $V_n$ of $N_1$ and $N_3$ , respectively, 1 ms after stimulus onset. (d) and (e) correspond to the time courses of the excitations; the region indicated by dotted lines in (d) shows that an excitation (in red) propagates towards the nerve ending (CNS) in $N_1$ (thus considered activated), but not in $N_3$ , depicted in (e) (thus considered inhibited). . . . .	36
3.1	Internal structure of the taxel from the multi-dimensional tactile array. Taken from [45].	40
3.2	3-Degree-of-Freedom tactile device. Taken from [71]. . . . .	40
3.3	18x18 array of airborne ultrasound transducers. Taken from [33]. . . . .	41
3.4	Assembled tactile display with ultrasonic actuators. Taken from [46]. . . . .	41
3.5	Schematic description of the surface acoustic wave tactile display. Taken from [66]. . . . .	41
3.6	1-point and 4-point nozzle mounts for the tactile display using airflows. Taken from [59].	42
3.7	Hardware implementation of the magneto-rheological tactile display. Taken from [58], used with permission under Creative Commons license. . . . .	42
3.8	TENS system structure documented by Kajimoto et al. [39]. . . . .	43
3.9	Electrotactile stimulation system developed by Kaczmarek et al. [38]. . . . .	44
3.10	Electrotactile display structure from Yoshimoto et al. [101]. . . . .	44
3.11	Block diagram of the electrical stimulation hardware. . . . .	45
3.12	Implemented TENS hardware. . . . .	46
3.13	Voltage amplifier circuit connected to the Arduino Due boards to condition the output of the DAC units to a range of -6 to 6 V. . . . .	47
3.14	Circuit board of the two voltage amplifiers connected to the Arduino Due board to condition the output of the DAC units to a range of -6 to 6 V. The implemented board is shown at the top and the circuit board drawing at the bottom. . . . .	48
3.15	First version of the VI converter electrical circuit, comprising a voltage-controlled current source (in green) and two current mirrors (in red and blue). . . . .	49
3.16	Simple NPN current mirror configuration. Modified from [97]. . . . .	50
3.17	Three-transistor Wilson NPN current mirror configuration. Modified from [97]. . . . .	51
3.18	Four-transistor Wilson NPN current mirror configuration. Modified from [97]. . . . .	52
3.19	Final version of the VI converter electrical circuit, comprising a voltage-controlled current source with transistors in parallel and ballast resistors (in green) and two modified Wilson current mirrors (in red and blue). . . . .	53
3.20	Circuit board comprising two VI units. The implemented board is shown at the top and the circuit board drawing at the bottom. . . . .	54
3.21	Assembled hardware for the VI converter. It includes the power supply board (marked in red), the four VI boards (marked in yellow) and the three fans (marked in blue). . . . .	55
3.22	Power supply board for the VI converter. The implemented board is shown at the top and the circuit board drawing at the bottom. . . . .	56

3.23	VI boards connected to the power supply board via pin header connectors (marked in red). . . . .	56
3.24	Electrode array. The circuit board drawing is shown on the left and the final electrode is on the right. . . . .	57
4.1	Relationships between psychophysical laws, psychological laws and sensory response laws. Modified from [23]. . . . .	60
4.2	Noise and signal-plus-noise theoretical frequency distributions for three different values of signal strength. Panel (a) shows the strongest signal strength, while panel (c) shows the weakest signal strength. Modified from [23]. . . . .	61
4.3	Time ranges before reaching nerve saturation for all four fingers when four stimuli were presented at 10 Hz during the six saturation tests (table 4.2). Panel (a) shows the response of the fingers to stimulus A, panel (b) to stimulus B, panel (c) to stimulus C and panel (d) to stimulus D. . . . .	67
4.4	Probability density distributions of the discrimination performances between all four stimuli of the five participants ( $P_1$ to $P_5$ ). Panels (a), (b) and (c) correspond to the responses of $P_1$ , panels (d), (e) and (f) to $P_2$ , panels (g), (h) and (i) to $P_3$ , panels (j), (k) and (l) to $P_4$ , and panels (m), (n) and (o) to $P_5$ . Each column refer to the stimuli at 10, 50 and 200 Hz. All computed decision criterions ( $c_a$ ) and their standard errors are marked in red in each panel. The corresponding T score values to the Z score values are shown in each panel. . . . .	69
4.5	Number of hits, misses, false alarms and correct rejections of the best performances of the five participants when discriminating between all stimuli. Panels (a) and (c) correspond to the performance of $P_1$ for 10 and 200 Hz, respectively. Panel (b) illustrates the performance of $P_4$ for 50 Hz. . . . .	70
4.6	Probability density distributions of the added discrimination performances between all stimuli of the five participants ( $P_1$ to $P_5$ ). Panels (a), (b) and (c) correspond to the added responses at 10, 50 and 200 Hz, respectively. All computed decision criterions ( $c_a$ ) and their standard errors are marked in red in each panel. The corresponding T score values to the Z score values are shown in each panel. . . . .	70
4.7	Probability density distributions of the discrimination performances between stimuli classes of the five participants ( $P_1$ to $P_5$ ). Panels (a), (b) and (c) correspond to the responses of $P_1$ , panels (d), (e) and (f) to $P_2$ , panels (g), (h) and (i) to $P_3$ , panels (j), (k) and (l) to $P_4$ , and panels (m), (n) and (o) to $P_5$ . Each column refer to the stimuli at 10, 50 and 200 Hz. All computed decision criterions ( $c_a$ ) and their standard errors are marked in red in each panel. The corresponding T score values to the Z score values are shown in each panel. . . . .	73

4.8	Number of hits, misses, false alarms and correct rejections of the best performances of the five participants when discriminating between stimuli classes. Panel (a) shows the performance of $P_3$ for 10 Hz, panel (b) of $P_2$ for 50 Hz and panel (c) of $P_1$ for 200 Hz.	74
4.9	Probability density distributions of the added discrimination performances between stimuli classes of the five participants ( $P_1$ to $P_5$ ). Panels (a), (b) and (c) correspond to the added responses at 10, 50 and 200 Hz, respectively. All computed decision criterions ( $c_a$ ) and their standard errors are marked in red in each panel. The corresponding T score values to the Z score values are shown in each panel. . . . .	74
4.10	Probability density distributions of the discrimination performances within stimuli classes of the five participants ( $P_1$ to $P_5$ ). Panels (a), (b) and (c) correspond to the responses of $P_1$ , panels (d), (e) and (f) to $P_2$ , panels (g), (h) and (i) to $P_3$ , panels (j), (k) and (l) to $P_4$ , and panels (m), (n) and (o) to $P_5$ . Each column refer to the stimuli at 10, 50 and 200 Hz. All computed decision criterions ( $c_a$ ) and their standard errors are marked in red in each panel. The corresponding T score values to the Z score values are shown in each panel. . . . .	76
4.11	Number of hits, misses, false alarms and correct rejections of the best performances of the five participants when discriminating within stimuli classes. Panels (a), (b) and (c) correspond to the performance of $P_1$ for 10, 50 and 200 Hz, respectively. . . . .	77
4.12	Probability density distributions of the added discrimination performances within stimuli classes of the five participants ( $P_1$ to $P_5$ ). Panels (a), (b) and (c) correspond to the added responses at 10, 50 and 200 Hz, respectively. All computed decision criterions ( $c_a$ ) and their standard errors are marked in red in each panel. The corresponding T score values to the Z score values are shown in each panel. . . . .	77
5.1	Mechanical stimulation model. Firstly, the displacement stimulus (position) is converted into velocity and acceleration signals. Each of the three signals is then separated into positive and negative components, rectified and multiplied by individual weights $\omega_i$ . The resulting signals are then summed and passed through a saturation filter. The output of the saturation filter constitutes the current input for the integrate-and-fire model, where a spike is produced when the input current results in a depolarisation of the membrane potential beyond a defined threshold to then go back to the membrane resting potential. Reproduced from [16]. . . . .	82
5.2	Flow chart representing the basic genetic algorithm structure. . . . .	88
5.3	Mechanical stimuli presented for verification of the modelled membrane potential of a SA1 fibre. Panels (a) and (c) show the mechanical stimulus waveforms, and panels (b) and (d) the corresponding membrane potential, with $V_{rest}$ shown in green. . . . .	92
5.4	Mechanical stimuli presented for verification of the modelled membrane potential of a SA1 fibre. Panels (a) and (c) show the mechanical stimulus waveforms, and panels (b) and (d) the corresponding membrane potential, with $V_{rest}$ shown in green. . . . .	93

5.5	Optimisation results when matching mechanical stimulus 5 from $MS_{SA1}$ to electrical stimulus 25 from $ES_s$ . The colour of the data points corresponds to the iterations of the optimiser. The largest cluster of fittest individuals is highlighted in red. . . . .	96
5.6	Optimised ES frequencies and amplitudes when matching mechanical stimulus 5 from $MS_{SA1}$ to electrical stimulus 25 from $ES_s$ . . . . .	96
5.7	Optimisation results when matching mechanical stimulus 6 from $MS_{PC}$ with electrical stimulus 3 from $ES_d$ . The colour of the data points corresponds to the iterations of the optimiser. The largest cluster of fittest individuals is highlighted in red. . . . .	97
5.8	Optimised ES frequencies and amplitudes when matching mechanical stimulus 6 from $MS_{PC}$ to electrical stimulus 3 from $ES_d$ . . . . .	97
6.1	Hardware implementation to compare the intensity sensation of electrical and mechanical stimulation. Panel (a) shows the electrotactile display with the 3x3 electrode matrix. Panel (b) shows the experiment setup, where the index and middle fingers of the right hand were presented with mechanical and electrical stimulation, respectively. Taken from [99]. . . . .	100
6.2	Brüel & Kjær mechanical stimulation system. Panel (a) shows the mechanical stimulator and panel (b) shows the corresponding amplifier to drive the stimulator. Taken from [49, 50]. . . . .	101
6.3	Brüel & Kjær Power Amplifier output voltage when using an input signal of 10 Vpp at 50 Hz. Channel 1 corresponds to the output and channel 2 to the input signal. . . . .	101
6.4	Dancer Design Tactor (mechanical stimulator). Taken from [15], used with the author's permission. . . . .	102
6.5	Design Dancer Amplifier output voltage when using an input signal of 10 Vpp at 50 Hz. Channel 1 (orange) corresponds to the output and channel 2 (blue) to the input signal. . . . .	102
6.6	Bode diagram for the displacement of the Minishaker using a frequency sweep of [2, 200] Hz. . . . .	105
6.7	Bode diagram for the displacement of the Tactor using a frequency sweep of [2, 200] Hz. . . . .	106
6.8	Measured forces of the Tactor using a frequency sweep of [2, 200] Hz. The data in blue corresponds to the measured force where there was a 1 mm gap between the load cell and the end-effector of the Tactor. The data in green represents the case where the load cell was barely making contact with the end-effector, and the data in red corresponds to when the load cell was fully making contact with all the end-effector and base of the Tactor. . . . .	107
6.9	Triads where the correct discrimination is given by the participant answering "one", for the first ES corresponds to the same class as the MS firstly presented. . . . .	108
6.10	Triads where the correct discrimination is given by the participant answering "two", for the second ES corresponds to the same class as the MS firstly presented. . . . .	108

6.11	Number of hits, misses, false alarms and correct rejections of $P_1$ , with the best performance of the five participants when discriminating between stimuli classes. . .	110
6.12	Probability density distributions of the discrimination performances between stimuli classes and of true stimuli pairs of the five participants ( $P_1$ to $P_5$ ). Panels (a), (c), (e), (g) and (i) correspond to the responses of $P_1$ to $P_5$ regarding the comparison between stimuli classes. Panels (b), (d), (f), (h) and (j) represent the responses of $P_1$ to $P_5$ when comparing true stimuli pairs. All computed decision criterions ( $c_a$ ) and their standard errors are marked in red in each panel. The corresponding T score values to the Z score values are shown in each panel. . . . .	111
6.13	Number of hits, misses, false alarms and correct rejections of $P_5$ , with the best performance of the five participants when discriminating between true stimuli pairs.	113
6.14	Probability density distributions of the added discrimination performances using the method of triads of the five participants ( $P_1$ to $P_5$ ). Panel (a) illustrates the discrimination between stimuli classes and panel (b) the discrimination of true stimuli pairs. All computed decision criterions ( $c_a$ ) and their standard errors are marked in red in each panel. The corresponding T score values to the Z score values are shown in each panel. . . . .	113
A.1	Full schematic of the DAC circuit board. . . . .	121
A.2	Full schematic of the VI converter circuit board. . . . .	122
A.3	Full schematic of the power supply circuit board. . . . .	123
A.4	Full schematic of the electrode array. . . . .	124
A.5	Logged ethical approval from the University of Bristol. . . . .	125

## ABBREVIATIONS

ADC	Analog-to-digital converter
AF	Activating Function
AP	Action Potential
CNS	Central Nervous System
CTR	Current transfer ratio
DAC	Digital-to-analog converter
ES	Electrical stimulation
FH	Frankenhaeuser-Huxley
HH	Hodking-Huxley
IF	Integrate-and-fire
MS	Mechanical stimulation
PC	Pacinian
RA	Rapidly adaptive
SA1	Slowly adapting type 1
SPC	Spikes per cycle
TENS	Transcutaneous electrical nerve stimulation
VI	Voltage to current
VP	Victor-Purpura





## INTRODUCTION

The majority of current systems providing haptic feedback for numerous applications regarding robotics are based on mechanical stimulation, which typically involves a complex hardware design that is expensive to produce and maintain [69, 85]. An alternative to mechanical stimulation is electrical stimulation; nevertheless, its use involving the production of different tactile sensations has not been widely studied. Targeting specific nerve fibres through electrical stimulation could result in the presentation of diverse tactile sensations.

Tactile sensations, such as texture, pressure and vibration, result from the stimulation and activation of cutaneous mechanoreceptors such as Merkel cells, Meissner, Pacinian and Ruffini corpuscles, which transform the mechanical stimuli on the skin into electrical signals. In the human body, they are distributed in the skin, muscles, joint capsules, viscera and tendons [14]. It is known that practically all interactions with objects involve the excitation of a large number of sensory units [53, 96]. The mechanical stimulus produces a change in the electric membrane potential of both the receptor and the nerve fibre connected to it. If the membrane potential rises above the excitation threshold, an action potential (AP) is induced, which will then lead to the transmission of the signal towards the Central Nervous System (CNS).

Electrical stimulation, or electrostimulation (ES) is a method used to induce certain sensations to the nervous system through electrical pulses. Electrotactile stimulation is one of the ES applications, where the nerve fibres connected to mechanoreceptors are activated. This can be achieved with the use of three types of electrodes: intracellular (invasively implanted very close to the nervous fibre), subcutaneous (less invasive than intracellular) and transcutaneous (non invasive, since they are applied on the skin).

Transcutaneous electrical nerve stimulation (TENS) is an established technique used as a research tool in domains such as neuroscience [27]. TENS can produce tactile sensations, stimulating nerve fibres connected to the skin mechanoreceptors, but has not yet found its

way into consumer applications as the relationship between more complex stimulation patterns and achieved sensation is not fully understood yet. It has been implemented to produce tactile sensations on the fingers [83], tongue [36] and hands [22], and was applied to arm muscles to induce their contraction and relaxation [54]. It has also been employed for the treatment of pain [7, 27, 44] and in relation to the auditory system, to treat tinnitus or improve sound perception [31]. Devices based on TENS would give the opportunity to increase the amount of information that systems could supply for medical, teleoperation, industrial and gaming applications, i.e. providing haptic feedback and controlling nerve selectivity. TENS can offer advantages over the alternative of mechanical stimulation (MS) systems [69, 85], such as a simpler hardware design and cheaper production and maintenance costs.

In order to investigate TENS and its dependence on electrode layout and excitation patterns, it is necessary to have a theoretical description of the electrical behaviour of the human skin, nerves and related tissues. Various models describing nerve excitation have been developed since the second half of the 19th century, showing the theoretical nerve response to a stimulus and its propagation through time and space. Commonly used nerve representations are the cable model [64] and the Hodgkin and Huxley model [32], which explain the electrical dynamics of nerve fibres through a set of differential equations. In addition, electrical properties of human skin and underlying tissues have been analysed and documented in diverse histological studies, providing further information that is required to successfully model a TENS system.

This work involves the development of a TENS system for a human finger and its comparison with a mechanical stimulation system, in both a simulated environment and through psychophysical tests to evaluate the performance of the hardware implementation, as illustrated in Figure 1.1. The main objective is to study the dependency on the TENS design, particularly on the electrode layout and excitation patterns (ES) related to selective nerve stimulation and the production of different tactile sensations, which has not been documented in literature. The principal research question regards if electrical stimulation can produce different tactile sensations, followed by a second question involving the comparison between the aforementioned tactile sensations resulting from ES to those resulting from MS.

The particular aims are:

- To build a simulation environment representing a multi-layered human finger tissue with the electrode array for ES.
- To implement and compare a MS simulation environment to the electrical simulation environment.
- To integrate the hardware for the comparison between the mechanical and electrical stimulation systems.
- To design and run psychophysical experiments to obtain subjective evaluation and comparison of the mechanical and electrical stimulation systems.

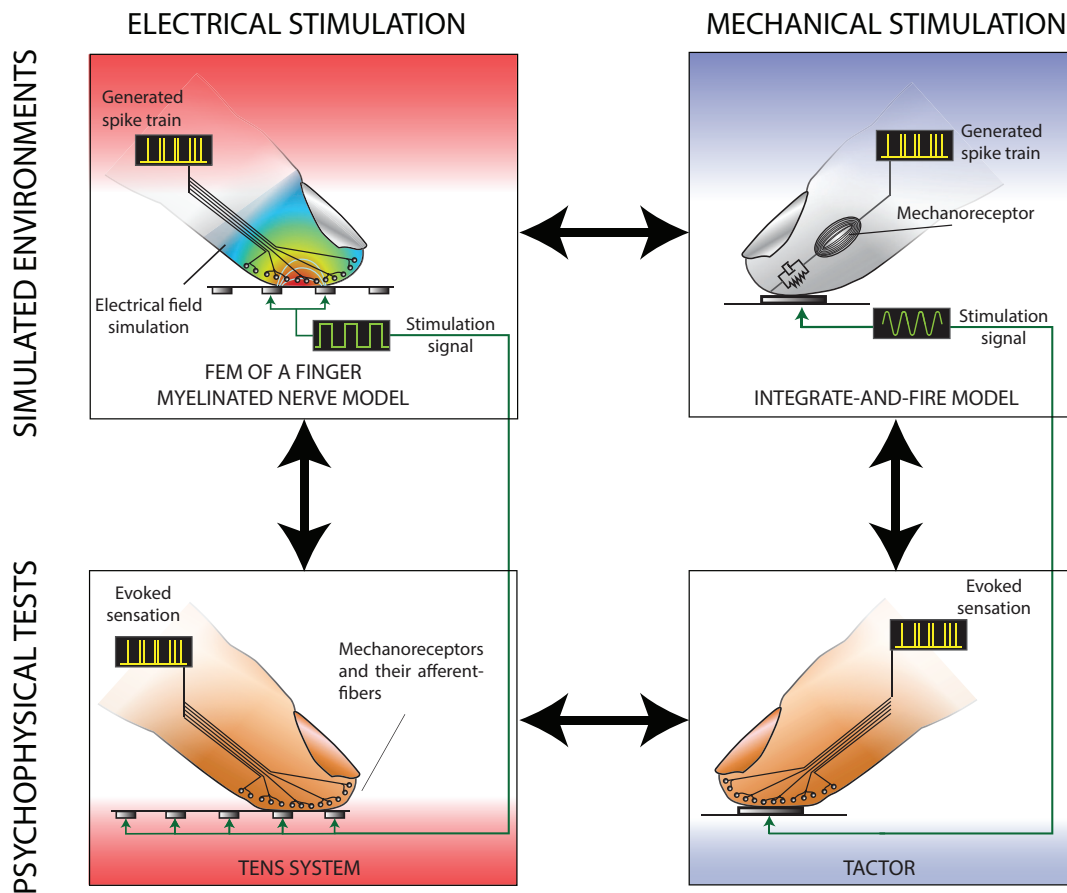


Figure 1.1: Project overview comprising the comparison of both mechanical and electrical stimulation systems.

This thesis consists of five main chapters. In chapter 2 the ES simulation environment representing a human finger in contact with an electrode array for TENS is introduced. Multiple simulation-based scenarios are shown as examples of the framework use regarding mathematical modelling of observed experimental findings and allowing the formulation of new simulation-based hypotheses, involving the selective stimulation of specific nerves located at different depths. In chapter 3 the hardware for the previously modelled TENS system is presented, followed by chapter 4, where the implementation of psychophysical tests to evaluate the tactile sensations created by the TENS hardware is described. The implementation of the MS simulation environment representing different nerves' response and its comparison to the ES simulation environment is discussed in chapter 5. The characterisation of the MS hardware and the psychophysical tests used to compare the tactile sensations produced by the MS to those resulting from the ES system are included in chapter 6. Finally, chapter 7 presents the main conclusions and future directions of this thesis.



## SIMULATION ENVIRONMENT FOR A TENS SYSTEM

This chapter begins with the anatomy and physiology of the human mechanoreceptors and the nerve fibres connected to them, through which the encoded tactile sensations travel towards the Central Nervous System (CNS). It is then analysed how the nerves can be electrically modelled in order to represent their response to stimuli, and different TENS simulation models are presented. Finally, the development of a simulated environment for electrical stimulation is described and the results of tests evaluating its performance are discussed. The simulated environment has been published in [2].

### 2.1 Tactile Sensations

Living organisms need to interact with their physical world. In order to create this interaction, they have sensory receptors. Sensory receptors can be classified into two main groups, one comprising those associated with somatic senses of temperature, pressure, touch and pain; and the second involving specialised sensory organs that provide the smell, taste, hearing, vision and equilibrium senses.

There are five basic types of sensory receptors [26] particularly responsive to a precise environmental change:

- Mechanoreceptors, which detect mechanical stretching or compression of the receptor or the tissue adjacent to it.
- Thermoreceptors used to perceive changes in temperature.
- Nociceptors or pain receptors that serve to identify when the tissue has been damaged either physically or chemically.

- Chemoreceptors, which are responsible for the detection of tasting and smelling, as well as for the detection of oxygen levels in the arterial flow and carbon dioxide concentration, among other examples.

Tactile and proprioception sensations are part of the mechanoreceptive somatic senses. Touch, pressure, vibration and tickle senses are included in the tactile sensations, whereas static position and rate of movement senses are in the proprioception class. In this case, the area of interest involves tactile sensations.

Even though touch, pressure and vibration can be considered separated sensations, they all use the same kind of receptors. The difference between them is the way those receptors are stimulated. For the case of touch, the stimulation comes from a direct contact with the skin or in the tissues right under it; on the other hand, pressure is generally caused by the deformation of deeper tissues and vibration results from a fast repetitive stimulation signal. This is called differential sensitivity; i.e., each receptor is highly sensitive to a specific stimulus and it is less responsive to others [26].

Practically all interactions with objects involve the excitation of a large number of sensory units [53, 96]. Tactile receptors work based on the concept of mechanotransduction, which refers to the conversion of a mechanical stimulus or force into an electrical signal. This process starts at the sensory nerve ending, where the mechanical force is received and converted into an electrical signal, inducing the propagation of the stimulation towards the CNS.

### **2.1.1 Anatomy and Physiology of the Tactile Sensations**

Mechanoreceptors are selective peripheral encoding tools that gather information from the parameters of the mechanical stimulus and send to the CNS a detailed representation of what is being sensed. They are distributed in the skin, tendons, muscles, joints and viscera. In the case of mammals, the mechanoreceptors in the skin include those illustrated in Figure 2.1, whose characteristics are listed as follows [14]:

- Hair follicles detect movement in the surface of the body and any initial contact with it.
- Meissner's corpuscles respond in a selective way to dynamic skin deformation.
- Pacinian corpuscles are the most sensitive encapsulated cutaneous mechanoreceptors in the skin that can follow high frequencies of vibratory stimuli and allow perception of distant events through transmitted vibrations. They are located immediately beneath the skin and deep in the fascial tissues.
- Merkel's discs are responsible for the steady-state signals that help to determine continuous touch of objects against the subject's skin. They transmit a precise spatial image of tactile stimuli and are responsible for the perception of the form and texture of objects.

- Ruffini receptors are important for the signalling of continuous states of deformation of tissues (prolonged pressure and touch signals). They signal skin stretch and allow the perception of the direction of object motion using the pattern of skin stretch.
- C-fibres and nociceptors identify touch and pressure. It has been proposed that inflammation or trauma may change the sensed stimuli from pleasant touch to pain.

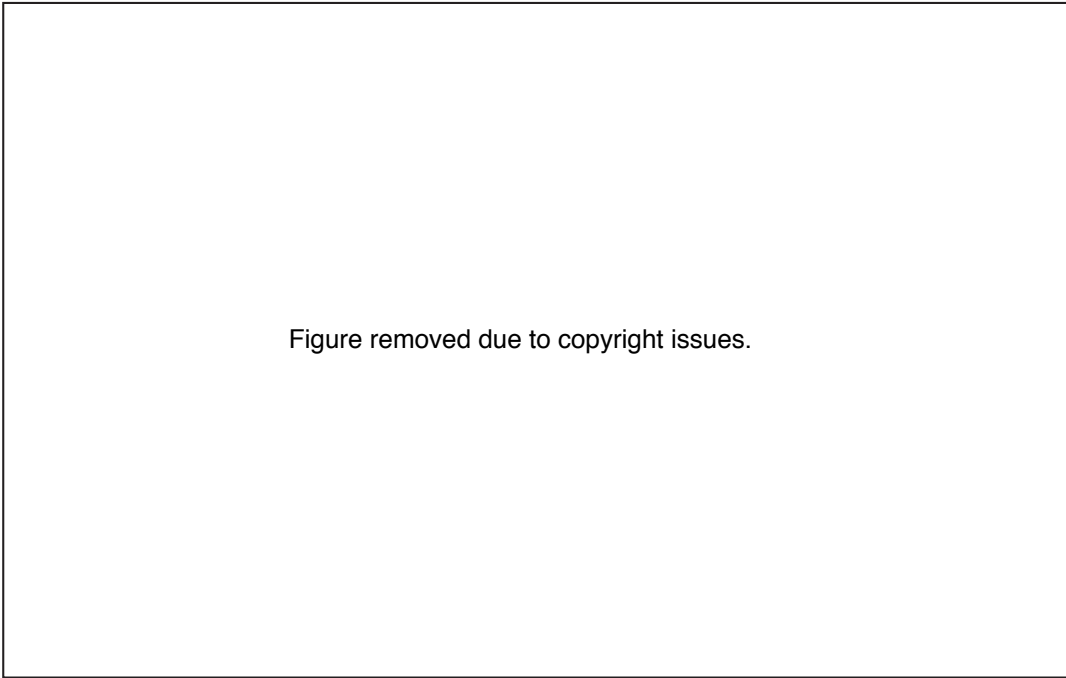


Figure removed due to copyright issues.

Figure 2.1: Cutaneous somatosensory receptors in mammals. Receptors can be RA rapidly adapting or SA slowly adapting, with a low threshold (LT) or a high one (HT). Taken from [14].

All sensory receptors have in common that, regardless of the type of stimulus that excites them, the membrane electrical potential of both the receptor and the nerve fibre connected to it will change. This is called a receptor potential. Once the receptor is stimulated, the membrane electrical potential of the nerve fibre (axon) connected to the receptor will change as well. If this amplitude variation overcomes a threshold, it will induce an action potential (AP), which will then lead to the transmission of the signal to the CNS, where it will be processed. An AP is divided into three main stages [26], as illustrated in Figure 2.2:

1. Resting: this first stage is where the membrane potential of the nerve is before excitation. The membrane is then said to be polarised, presenting a potential of around -90 to -70 mV; i.e., the potential inside the fibre is more negative than the one in the extracellular fluid outside the nerve fibre.



2. Depolarisation: once the stimulus arrives to the membrane, the permeability to sodium ions changes in the membrane, causing the diffusion of these ions to the positive direction. Thus, the previous negative voltage is neutralised by the inflowing positively charged ions. This phenomenon is called depolarisation. In large nerve fibres, this potential change may result in a positive voltage, called overshoot (reaching values around 100 mV).
3. Repolarisation: after the fibre is depolarised, potassium channels open allowing rapid diffusion of these ions to the exterior, which results in having a negative membrane potential again (repolarisation). The ion channels and the pumps can produce a hyperpolarisation at the end of the repolarisation stage, where the membrane potential reaches its maximum negative value before going back to rest.

The excitatory state of a fibre is defined as the summated degree of excitatory drive to it. It is said that the fibre is in an excitatory state if there is a higher degree of excitation than inhibition. In the same way, if there is more inhibition than excitation, then it is considered an inhibitory state [26].



Figure 2.2: Typical action potential. Taken from [26].

All of these receptors are connected to specific nerve fibres. The particularities of the fibres will define how fast the stimulus can travel to the CNS and the way they will be adapted to the presented stimuli. These fibres can be divided into types A and C, having the type A subdivided into  $\alpha$ ,  $\beta$ ,  $\gamma$ , and  $\delta$  fibres. Type A are the common large and medium-sized myelinated fibres of spinal nerves (covered by layers of an insulating material called myelin), whilst type C are the small unmyelinated nerve fibres that conduct impulses at lower velocities. Their sizes, conduction velocity and functions are also given in Figure 2.3. It is important to point out that different nerve fibres can transmit diverse sensations due to the specific area in the CNS to which they

lead to. Almost all tactile receptors transmit their signalling through type  $A\beta$  nerve fibres; free nerve ending tactile receptors can either use  $A\delta$  myelinated fibres or C unmyelinated fibres [26]. Therefore, in case of looking for a neuro-selective stimulation, it would not be possible to carry out based on the fibre type only.

Haptic perception is usually related to active manual exploration in order to process material features of objects and surfaces (such as texture, compliance and thermal quality), combining both tactile and proprioceptive afferent information. Haptic perception involves the peripheral receptors that receive and signal information regarding the features of surfaces and objects, as well as the determination of where on the body a stimulus is applied and where in the external environment a stimulus is touched [57].

## 2.2 Modelling Neurons

Describing the electrical characteristics of neurons can be done through circuit models; therefore, understanding how a single neuron works is fundamental. The membrane consists of a double layer lipid with low conductivity to charges, functioning as a capacitance within which proteins are embedded. These proteins work as ion channels whose opening and closing can be described by the conductance of ion currents. Modelling the nerve is important in this work because the main interest is the study of the electrical stimulation of the nerves, which involves the simulation of the stimulus and its effect on a nervous fibre before looking for a physical implementation.

### 2.2.1 Excitation Models

In the early 1950's, Hodgkin and Huxley successfully modelled the dynamics of the membrane of a giant axon of a squid (HH model) [32], Frankenhaeuser and Huxley later modified the set of equations in the HH model using a myelinated frog nerve, creating the FH model [18]. It should be noted that the dynamics described by both models have been documented to be applicable to mammals [75], adjusting the corresponding values for the variables presented in the equations. After these models were documented, new studies modelled mammalian myelinated axons using rabbits and rats [11, 79]. Finally, it was in 1976 when McNeal published the first model for excitation on myelinated nerves, using the cable equation to represent small axon segments connected together with axoplasm resistances and whose behaviour was described by the FH model [64]. The myelinated nerve has non-myelinated areas called Ranvier nodes, where the excitation and action potentials occur and are registered. All these models have been the basis of multiple researches with different axon membrane data to simulate and predict the nerve response to electrical stimulation [86]. Nevertheless, it was documented by Rattay in [74] that, when using anodic and cathodic stimulation to simulate the response of the HH and FH models, the FH model do not allow the simulation of a cathodic block when using

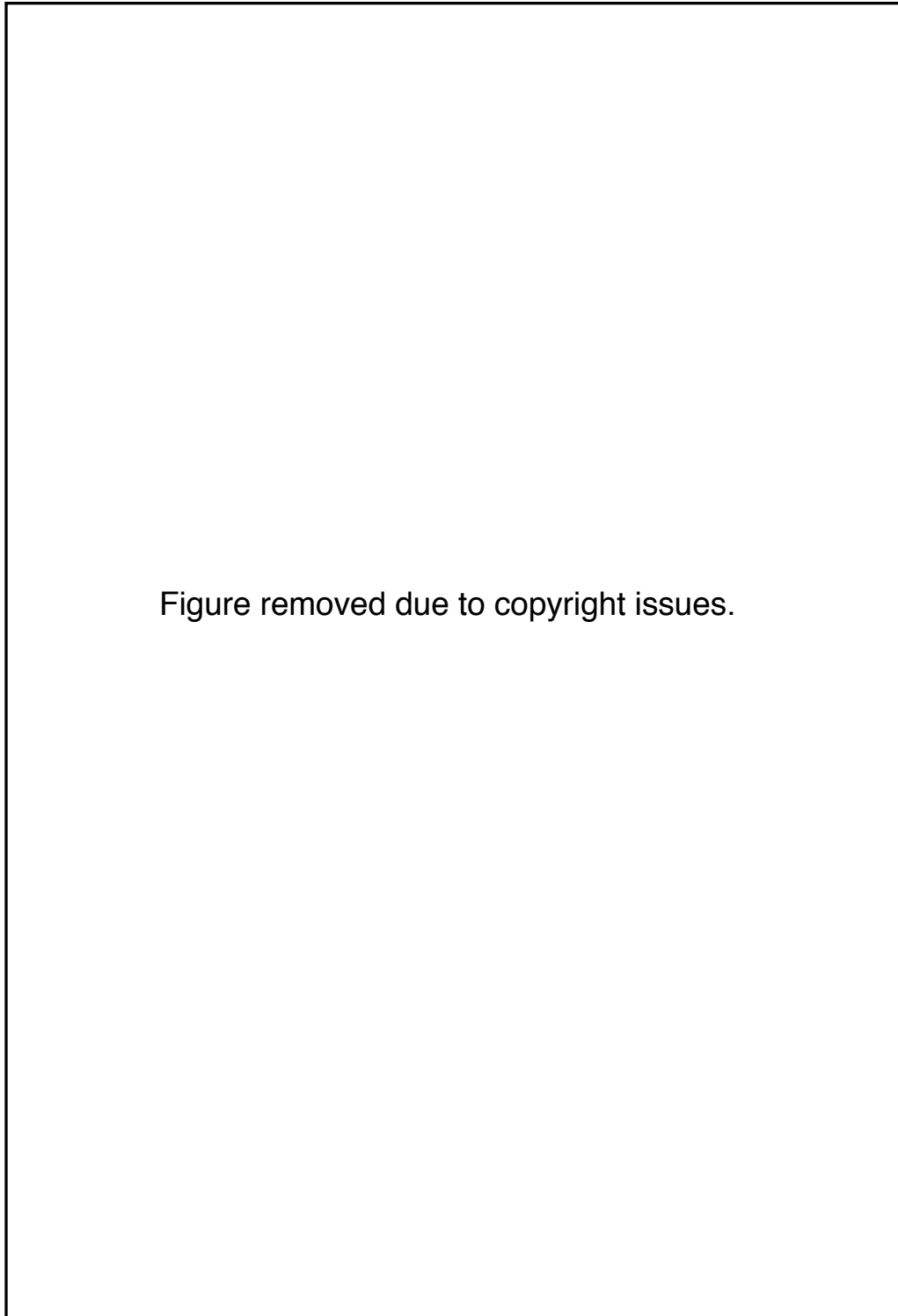


Figure 2.3: Physiologic classifications and functions of nerve fibres. Taken from [26].

electrical stimulation, whereas the HH model (implemented with the corresponding modifications to represent myelinated fibres [80]) can indeed simulate a cathodic block.

## 2.3 TENS Simulation Models

ES is a technique to artificially activate fibres through electrical current pulses to the body. These current pulses flow between two electrodes, the cathode or active one and the anode or indifferent one, inducing the depolarisation of cellular membranes in specific tissues. TENS is one application of this type of stimulation. In order to study its effects in an excitable fibre, the system and the stimulation must be modelled and simulated or directly observed in testing TENS with real subjects.

TENS has been used to study the effects of defined stimulation patterns applied to specific nerves in different body parts. It has been implemented to produce tactile sensations on the fingers [83], tongue [36] and hands [22], and was applied to arm muscles to induce their contraction and relaxation [54]. It has also been employed for the treatment of pain [7, 27, 44] and in relation to the auditory system, to treat tinnitus or improve sound perception [31].

In simulated environments regarding nerve stimulation, two stages are generally found, following McNeal's structure [64]. The first one corresponds to the electrical field distribution caused in the specific area by the electrodes and the second one involves the nerve response to the change in the extracellular potential. In this project, the area of stimulation that will be used is the human finger.

Research groups have also been studying and developing systems to excite nerves which carry information from mechanoreceptors in the skin. Kajimoto et al. [40, 41] developed a system with the intention of selectively stimulating three different types of mechanoreceptors. The nerve fibres were represented by a cable model and the predicted response was compared to users' subjective perception of the various stimuli. They showed in their simulation that when deeper nerve fibres were targeted for stimulation, unwanted stimulation of shallower fibres was also produced.

Rattay used a semi-infinite homogeneous conductive medium for the human finger, considering a thin layer of skin between the electrode and the medium. He assumed a constant voltage on the surface of the medium within an electrode-shaped area. He also proposed an analytical solution of the electrical field for circular electrodes, as well as the model for the activating function (AF), which would work as a predictor of a nerve spiking [73, 74].

Likewise, use of a finite element model (FEM) of the skin and underlying tissues in conjunction with nerve fibre models, has been an area of interest. Kuhn [54–56] modelled a TENS system for the human arm, using a FEM to study the effect on nerve selectivity from changing the electrodynamic properties of the skin (such as resistivity and permittivity) and the size of the electrode array. He implemented five different nerve-fibre models linked to the FEM: a non-linear

cable model, a non-linear temperature-compensated cable model, a non-linear mammalian nerve fibre model, a non-linear double cable model and a linear double cable model. The results of each model were compared to the user's muscular activation when the stimulus was presented to motor nerves, together with electrode measurements of intramuscular potential and potential on the skin surface. It was concluded that a non-linear cable model, where the nodes of Ranvier, paranodal and internodal sections were included, was the most realistic.

The developed simulation environment, described in [2], is a representation of the human finger giving a setup that can be used to study TENS, more specifically to systematically design and test new TENS devices and evaluate the effect of using different stimulation patterns. The documented results of the testing of the environment show that by suitable choice of the electrode currents (stimulation pattern), a specific nerve fibre can be selectively stimulated at different depths without exciting other fibres. Using this environment, it is possible to replicate previous reported experimental findings and to propose and discuss new hypotheses regarding tactile perception and their relation to different stimulation patterns.

## 2.4 Materials and Methods

The environment consists of a finite element electrical model of the human finger connected to a representation of the nerve response, based on the cable model [2]. It can be used to analyse the specific behaviour of a nerve fibre in response to a particular distribution of stimulation currents at the surface of the skin. Advantages of the FEM include the generation of the modelled human finger's physical response at any location, taking account of local variations of electrical properties, which can sometimes be neglected by analytical approaches. The model also allows calculation of the time-varying activation of fibres in response to complex time-varying stimuli. Overall, it offers a rapid analysis of performance and evaluation of design parameters for virtual prototyping of TENS systems, by providing a visual representation and calculation of physical parameters simultaneously.

### 2.4.1 Electrical Field Model

A FEM of a human finger with a cylindrical geometry and a spherical fingertip is used to compute the current and electric field distributions generated by a TENS system. The FEM was developed using Elmer (<https://www.csc.fi/web/elmer>) and Gmsh (<http://www.gmsh.info>) software. The FEM is segmented into tetrahedral elements, each treated as a volume conductor with one of three values for conductivity  $\sigma_{\text{bone}}$ ,  $\sigma_{\text{fat}}$  or  $\sigma_{\text{skin}}$ , as appropriate (the pulp of the finger is taken to be fat throughout; in fact, it is composed of fibrous septa filled with fat [81, 98]). The skin is set to be dry. The model considers three nerve fibres, two running parallel to the skin and one running first perpendicular and then parallel to the skin, representing nerve fibres connected to Merkel, Pacinian and Meissner receptors respectively. Capacitive effects, which have been found

to have a minor influence on nerve activation in TENS [54], are neglected. This model is clearly an oversimplification since in practice the skin, tissue and bone have multiple compartments. However, these simplifications allow implementation of a computationally tractable model whose results are intended to approximate the real situation. Results from a model considering dermis and epidermis as separately specified layers (not presented here) were not significantly different to those obtained using the simplified single-layer skin model, as might be predicted from the work of Peters et al. [61].

The calculation of the electric potential in the FEM was achieved through the static current conduction solver with the biconjugate gradient stabilised method (BiCGStabl) and a convergence tolerance of  $10^{-12}$ . This process had to be executed once for each modelled nerve fibre ( $N_x$ ).  $N_1$  was located at 1.5 mm depth and  $N_3$  at 2 mm from the skin surface (top right panel in Fig. 2.4), both running parallel to the skin.  $N_2$  had a first portion running perpendicular to the skin from 1 to 1.5 mm depth, and then a second portion at 1.5 mm depth running parallel to the skin. The values for the finger dimensions and conductivity are listed in Tables 2.1 and 2.2. The fingernail area was connected to ground. The array of eight electrodes is modelled as a plane surface making direct contact with the finger (Fig. 2.4). The electrode spacing is 1 mm and each electrode has dimensions 1 mm  $\times$  8.5 mm. The area covered by the current electrode design targets the majority of the receptive fields of mechanoreceptors in the human fingertip (last two thirds of the distal segment) [35]. Its dimensions are based on anthropometric data for the human index finger, which suggests that the average index fingertip measures around 16 to 22 mm in length [4, 5]. A linear array was chosen because it allows the activation of some or all of the electrodes to study the effects on fibre activation from complex stimulation patterns.

Table 2.1: **Dimensions used in the finger FEM [84].**

Parameter	Value / m
Finger diameter	0.02
Bone diameter	0.005
Skin thickness	0.0009
Finger length	0.084
Electrode size	0.001 $\times$ 0.0085

Table 2.2: **Conductivity values of the human finger [29, 30].**

Material	Conductivity / S/m
$\sigma_{\text{skin}}$	0.0552
$\sigma_{\text{fat}}$	0.0417
$\sigma_{\text{bone}}$	0.0202

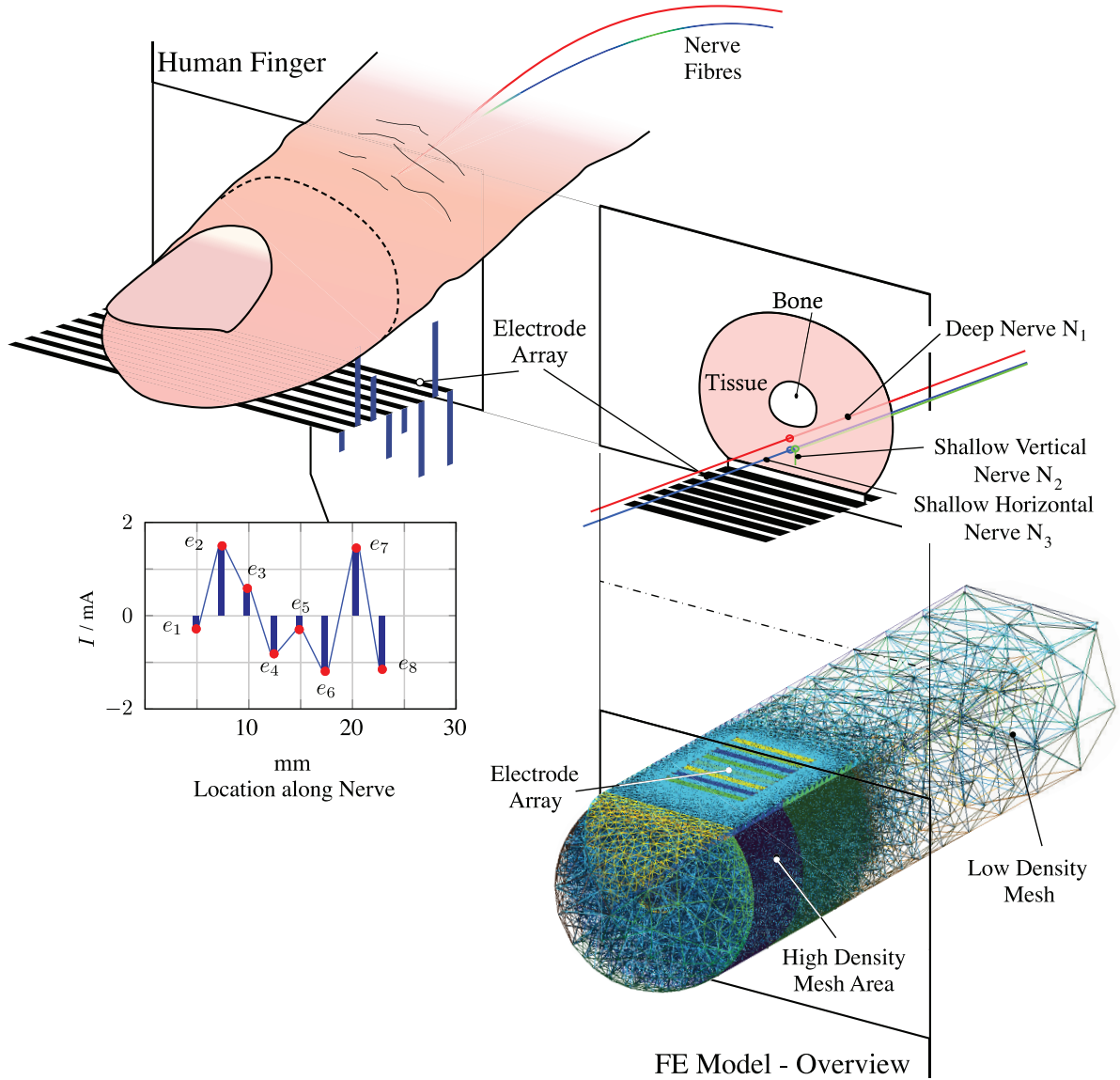


Figure 2.4: FEM developed for a human finger with an 8-electrode array located on the finger pad. A drawing of a real finger is shown at top left, with its pad on the electrode array. At top right is shown a simplified model of the finger, used to develop the FEM illustrated at bottom right (with the finger inverted to show the electrode array on the finger pad). One example of the currents flowing from array to finger is indicated in the top left image and also shown in the graph at bottom left, in which the horizontal axis represents distance along the nerve fibre, running from the fingertip towards the CNS. Taken from [2], used with permission under Creative Commons license.

### 2.4.2 Nerve Response Model

Each of the myelinated nerve fibres is represented by an electrical cable model in which the nerve membrane is described as an electrical circuit. The nerve fibre is considered as a cylinder divided into nodes of Ranvier separated by distance  $\Delta x$ , as shown in Fig. 2.5, where three nodes are represented. The corresponding parameters for the nerve modelling are listed in Table 2.3.

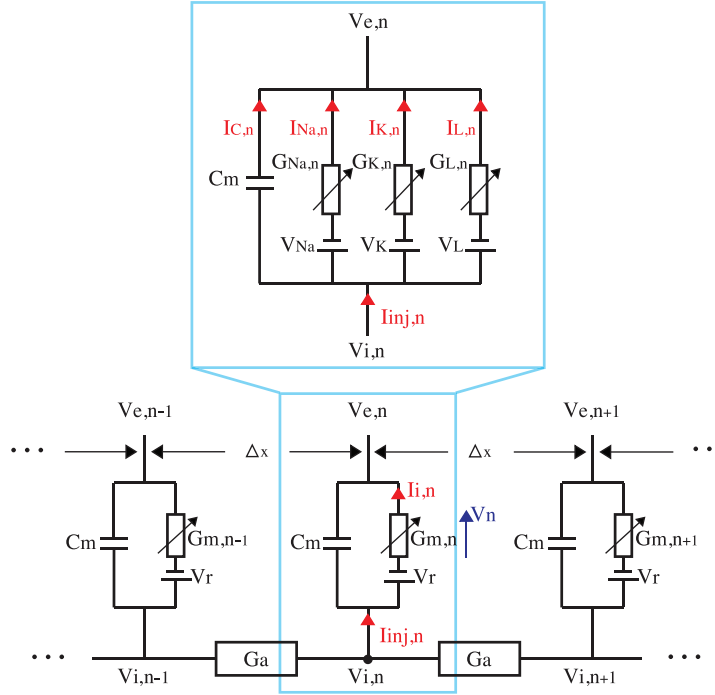


Figure 2.5: Electrical network representation of a myelinated fibre. Taken from [2], used with permission under Creative Commons license.

Table 2.3: **Variables for the electrical network representation of a myelinated fibre.**

Variables	Parameter represented
$V_{e,n}$	Extracellular potential at node $n$
$C_m$	Membrane capacity
$G_{m,n}$	Nodal membrane conductance
$G_a$	Axial internodal (axoplasm) conductance
$V_{i,n}$	Intracellular potential at node of Ranvier $n$
$I_{i,n}$	Total ionic current
$L$	Active length of the membrane
$\Delta x$	Segment length of the fibre
$d$	Fibre diameter

The injected membrane current at the  $n$ th node  $I_{inj,n}$  is the sum of the currents flowing through the capacitor  $C_m$  and the membrane conductance  $G_{m,n}$  as follows:



Table 2.4: **HH model parameters for human nerve fibres [25, 70, 80, 102, 103].**

Parameter	Value	$Q_{10}$	$T_0/^\circ\text{C}$
Membrane resting potential $V_r$	-79.4 mV	1.035	6.3
Gas constant R	8.315 J/Kmol	-	-
Faraday Constant F	$9.649 \times 10^4$ C/mol	-	-
$[\text{Na}^+]_o/[\text{Na}^+]_i$	7.210	-	-
$[\text{K}^+]_o/[\text{K}^+]_i$	0.036	-	-
$[\text{leakage}^+]_o/[\text{leakage}^+]_i$	0.0367	-	-
Sodium conductance $g_{\text{Na}}$	$6400 \text{ S/m}^2$	1.02	24
Potassium conductance $g_{\text{K}}$	$600 \text{ S/m}^2$	1.16	20
Leakage conductance $g_{\text{L}}$	$575 \text{ S/m}^2$	1.418	24
Axoplasmic intracellular resistivity $\rho_i$	$0.25 \text{ } \Omega\text{m}$	$1.35^{-1}$	37
Membrane capacitance $C_m$	$0.028 \text{ F/m}^2$	-	-
Fibre diameter $d$	$4 \text{ } \mu\text{m}$	-	-
Distance between nodes of Ranvier $\Delta x$	$78.461 \text{ } \mu\text{m}$	-	-
Nodal length $L$	$1.061 \text{ } \mu\text{m}$	-	-

 Table 2.5: **HH model parameters for human nerve fibres [80].**

Parameter	$Q_{10}$	$T_0/^\circ\text{C}$	A	B	C	D
$\alpha_m$	2.23	6.3	4.42	2.5	0.1	1
$\beta_m$	2.23	6.3	4.42	4.0	18	-
$\alpha_n$	1.5	6.3	1.47	0.07	20	-
$\beta_n$	1.5	6.3	1.47	3.0	0.1	-
$\alpha_h$	1.5	6.3	0.2	1.0	0.1	10
$\beta_h$	1.5	6.3	0.2	0.125	80	-

$$(2.1) \quad I_{\text{inj},n} = C_m \frac{dV_n}{dt} + I_{i,n},$$

where  $V_n$  is the reduced membrane potential (see Fig. 2.5) and the total ionic current is the sum of the sodium, potassium and leakage currents  $I_{i,n} = I_{\text{Na},n} + I_{\text{K},n} + I_{\text{L},n}$ . These ionic currents are described by the HH equations, which represent the dynamic behaviour (opening and closing) of the ion channels, controlled (see below) by the gating variables  $n$ ,  $m$ , and  $h \in (0,1)$ . This behaviour is determined by (2.2) to (2.4), in which the values of  $\alpha$  and  $\beta$  are computed according to equations (2.5) to (2.7) using documented values for the human nerve fibre for the constants  $A$ ,  $B$ ,  $C$ ,  $D$ ,  $Q_{10}$  factor (see Table 5) and environmental temperature  $T$ , as follows:

$$(2.2) \quad \dot{m}_n = [-(\alpha_m(V_n) + \beta_m(V_n))m_n + \alpha_m(V_n)],$$

$$(2.3) \quad \dot{n}_n = [-(\alpha_n(V_n) + \beta_n(V_n))n_n + \alpha_n(V_n)],$$

$$(2.4) \quad \dot{h}_n = [-(\alpha_h(V_n) + \beta_h(V_n))h_n + \alpha_h(V_n)],$$

$$(2.5) \quad \alpha_{m,n}(V_n) = 1000A Q_{10}^{(T-T_0)/10} \frac{B - 1000CV_n}{D e^{B-1000CV_n} - 1},$$

$$(2.6) \quad \beta_{m,n}(V_n), \alpha_h(V_n) = 1000A Q_{10}^{(T-T_0)/10} e^{-\frac{1000V_n}{C}},$$

$$(2.7) \quad \beta_h(V_n) = 1000A Q_{10}^{(T-T_0)/10} \frac{1}{e^{B-1000CV_n} + 1}.$$

The ion conductances and the maximum membrane conductances are then described by:

$$(2.8) \quad G_{Na_n} = m_n^3 h_n G_{Na,max},$$

$$(2.9) \quad G_{K_n} = n_n^4 G_{K,max},$$

where the conductances  $G_{ion,max}$  are calculated from known values  $g_{ion}$  of conductance per unit area of membrane (Table 4) using:

$$(2.10) \quad G_{ion,max} = \pi d L g_{ion} \text{ for } ion = Na, K, L.$$

Referring to the electrical equivalent circuit (Fig. 2.5), it can be seen that the ion currents are given by:

$$(2.11) \quad I_{Na,n} = G_{Na,n}(V_n - V_{Na,max}),$$

$$(2.12) \quad I_{K,n} = G_{K,n}(V_n - V_{K,max}),$$

$$(2.13) \quad I_{L,n} = G_{L,n}(V_n - V_{L,max}).$$

Thus, the HH model defines the total ionic current as:

$$(2.14) \quad I_{i,n} = G_{Na,max} m_n^3 h_n (V_n - V_{Na,max}) + G_{K,max} n_n^4 (V_n - V_{K,max}) + G_{L,max} (V_n - V_{L,max}).$$

In equation (2.14), the channel reversal potentials  $V_{Na,max}$ ,  $V_{K,max}$  and  $V_{L,max}$  come from the Nernst equation [32]:

$$(2.15) \quad V_{ion,max} = \frac{RT_k}{F} \ln \left( \frac{[ion]_o}{[ion]_i} \right) - V_r \text{ for } ion = Na, K, L,$$

where  $T_k$  is the temperature in Kelvin,  $R$  the universal gas constant,  $F$  the Faraday constant and  $[ion]_o/[ion]_i$  the extracellular to intracellular ion concentration ratio for sodium, potassium and leakage ions. The intracellular conductance  $G_a$  (see Fig. 2.5) is calculated from the specific resistivity  $\rho_i$ , as follows:

$$(2.16) \quad G_a = \frac{\pi d^2}{4\rho_i \Delta x}.$$

Considering all  $N$  nodes in the nerve fibre, the current flowing through each is described by:

$$(2.17) \quad I_{\text{inj},n} = \begin{cases} (V_{i,n+1} - V_{i,n})G_a & \text{for } n = 1, \\ (V_{i,n+1} - 2V_{i,n} + V_{i,n-1})G_a & \text{for } n \in (2, 3, \dots, N-1), \\ (V_{i,n} + V_{i,n-1})G_a & \text{for } n = N. \end{cases}$$

Combining (2.17) with (2.1) and (2.14), and using  $V_{i,n} = V_n + V_{e,n} + V_r$  (where  $V_r$  is the resting potential, see Fig. 2.5) [64], the potential along the fibre (for all the  $N$  nodes) is described by the non-linear equation (2.18), using the matrices (2.19), (2.20) and (2.21):

$$(2.18) \quad \mathbf{V} = \frac{1}{C_m} \int -\mathbf{I}_i + \mathbf{G}(\mathbf{V} + \mathbf{V}_e) dt,$$

$$(2.19) \quad \mathbf{V} = \begin{bmatrix} V_1 \\ \vdots \\ V_N \end{bmatrix}_{N \times 1},$$

$$(2.20) \quad \mathbf{G} = \begin{bmatrix} -G_a & G_a & 0 & 0 & \cdots & 0 \\ G_a & -2G_a & G_a & 0 & & 0 \\ 0 & G_a & -2G_a & \ddots & \ddots & \vdots \\ 0 & 0 & \ddots & \ddots & G_a & 0 \\ \vdots & & \ddots & G_a & -2G_a & G_a \\ 0 & \cdots & & 0 & G_a & -G_a \end{bmatrix}_{N \times N},$$

$$(2.21) \quad \mathbf{I}_i = \begin{bmatrix} [-G_{\text{Na,max}} m_1^3 h_1 (V_1 - V_{\text{Na,max}}) - G_{\text{K,max}} n_1^4 (V_1 - V_{\text{K,max}}) - G_{\text{L,max}} (V_1 - V_{\text{L,max}})] \\ \vdots \\ [-G_{\text{Na,max}} m_N^3 h_N (V_N - V_{\text{Na,max}}) - G_{\text{K,max}} n_N^4 (V_N - V_{\text{K,max}}) - G_{\text{L,max}} (V_N - V_{\text{L,max}})] \end{bmatrix}_{N \times 1},$$

Likewise, the gating variables are given by (2.22), (2.23) and (2.24):

$$(2.22) \quad \begin{aligned} \dot{\mathbf{m}} &= \begin{bmatrix} \dot{m}_1 \\ \vdots \\ \dot{m}_N \end{bmatrix}_{N \times 1} \\ &= \begin{bmatrix} -(\alpha_m(V_1) + \beta_m(V_1))m_1 + \alpha_m(V_1) \\ \vdots \\ -(\alpha_m(V_N) + \beta_m(V_N))m_N + \alpha_m(V_N) \end{bmatrix}_{N \times 1}, \end{aligned}$$

$$(2.23) \quad \begin{aligned} \dot{\mathbf{n}} &= \begin{bmatrix} \dot{n}_1 \\ \vdots \\ \dot{n}_N \end{bmatrix}_{N \times 1} \\ &= \begin{bmatrix} -(\alpha_n(V_1) + \beta_n(V_1))n_1 + \alpha_n(V_1) \\ \vdots \\ -(\alpha_n(V_N) + \beta_n(V_N))n_N + \alpha_n(V_N) \end{bmatrix}_{N \times 1}, \end{aligned}$$

$$(2.24) \quad \begin{aligned} \dot{\mathbf{h}} &= \begin{bmatrix} \dot{h}_1 \\ \vdots \\ \dot{h}_N \end{bmatrix}_{N \times 1} \\ &= \begin{bmatrix} -(\alpha_h(V_1) + \beta_h(V_1))h_1 + \alpha_h(V_1) \\ \vdots \\ -(\alpha_h(V_N) + \beta_h(V_N))h_N + \alpha_h(V_N) \end{bmatrix}_{N \times 1}. \end{aligned}$$

The constants  $C_m$ ,  $G_a$ ,  $V_{Na,max}$ ,  $V_{K,max}$ ,  $V_{L,max}$ ,  $G_{Na,n}$ ,  $G_{K,n}$  and  $G_{L,n}$  directly depend on the node size.

Each modelled node on the nerve fibre corresponded to a group of four nodes of Ranvier, in order to reduce computational cost and simplify the analysis of the nerve response. The dynamic behaviour of each nerve node was described by the HH model using documented parameters (Tables 2.4 and 2.5, with  $T = 20$  °C) from human nerve fibres for the constants in (2.5) to (2.7). The solution of the nerve response model equations was found using MATLAB (<https://uk.mathworks.com/>), with two main blocks representing each nerve fibre. One block corresponds to a compartment model based on the cable model, solving (2.17) and (2.1), using the ionic current obtained through the second block, which implements the HH model, solving (2.14) to calculate (2.18). Due to the high computational cost and the stiffness of the system, the ode23s solver was selected with variable step. The excitation signal was a monophasic square pulse presented after 0.01 s with 0.00045 s width, taking into account that axon chronaxies for small myelinated fibres are generally in the range 0.0002 to 0.0007 s [72]. All the amplitudes for the

electrodes were chosen within a range of  $-5$  to  $5$  mA, since it is known that larger currents would result in pain and discomfort for the user, possibly leading to injuries [6, 21].

The effect of each electrode current regarding a possible cathodic block of the nerve fibre is of particular interest here. The Frankenhaeuser-Huxley (FH) equations, generally used to describe myelinated fibres, do not allow simulation of such a block [74]. Hence, the Hodgkin and Huxley (HH) equations, which can simulate a cathodic block, were chosen for use in the model (they are normally used to represent unmyelinated fibres, but are here implemented with the corresponding modifications to describe a myelinated fibre [80]). A single node can be locally represented by the HH equations [32]. The expanded circuit at the top of Fig. 2.5 represents one node. It shows how the membrane conductance  $G_{m,n}$  of a node derives from the leakage conductance  $G_{L,n}$  representing ion diffusion through the membrane, and from the sodium and potassium conductances,  $G_{Na,n}$  and  $G_{K,n}$ , dependent on the particularities of each channel and on the probability of it being open. The injected membrane current at the  $n$ th node  $I_{inj,n}$  is the sum of the currents flowing through the capacitor  $C_m$  and the membrane conductance  $G_{m,n}$ .

## 2.5 Results

In the following subsections the simulation results are presented using the aforementioned model for an overall validation and the study of two cases of interest with respect to selective nerve stimulation. The first one corresponds to an experimentally documented case by Yem and Kajimoto [99]; their results suggest that cathodic stimulation excites fibres from both Merkel cells (running parallel to the skin) and Meissner corpuscles (running first perpendicular to the skin and then parallel to the skin), whereas anodic stimulation excites fibres from Meissner corpuscles only. The second scenario consists of two nerve fibres running parallel to the skin at different depths, simulating fibres connected to Merkel and Pacinian receptors, that are selectively stimulated through a specific pattern of injected currents. Both scenarios are used as examples for demonstrating the usage of the simulation environment in the context of two important steps of studying tactile perception: the mathematical modelling of observed experimental findings (case 1) and the formulation of new hypotheses (case 2), which form the basis for new experimental studies.

### 2.5.1 Overall Validation of Simulation Environment

To illustrate the performance of the simulation model, simulation results of a two and eight active electrode setup using one nerve fibre running parallel to the skin at constant depth are provided. For both setups, the effects evaluated at two stages are shown, as proposed by McNeal [64]:

1. The mapping of the currents  $I_{el}$  applied through the electrode array to the extracellular voltage  $V_{e,n}$ , evaluating the FEM.

2. The mapping of the extracellular voltage  $V_{e,n}$  to the membrane potential of a specific nerve fibre  $V_n$ , involving the link between the FEM and the nerve fibre model.

### 2.5.1.1 Two-electrode Setup

The nerve fibre was modelled at depth  $z = 1.5$  mm with two transcutaneous electrodes located at 7 and 9 mm from the fingertip (panel (a) in Fig. 2.6), with currents  $I_{el,1} = 3$  mA and  $I_{el,2} = -3$  mA. Panel (b) in Fig. 2.6 shows the results of stage one in form of the extracellular potential  $V_{e,n}$  as a function of distance (millimetres) along the nerve fibre.

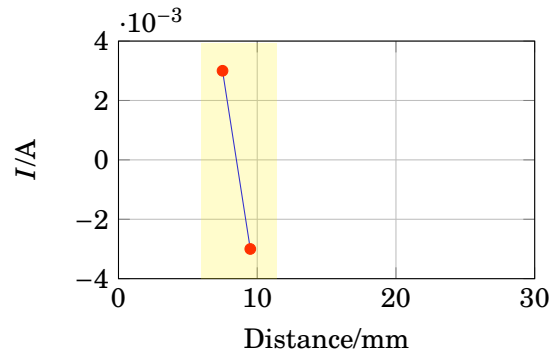
Since the exact position of the electrodes with respect to the nerves is known, the tracing of the change in voltage resulting from the electrode currents is straightforward. The extracellular potential  $V_{e,n}$  plot shows the expected result (proximity to the anodic stimulation, i.e. positive currents, increasing the extracellular potential  $V_{e,n}$  and proximity to cathodic stimulation decreasing  $V_{e,n}$ ) in the area of interest (marked in yellow in panels (a), (b) and (c) in Fig. 2.6).

The membrane potential is shown as a reduced voltage  $V_n$  (i.e., the static offset is subtracted); thus, positive values of the potential represent the fibre's depolarisation, and negative hyperpolarisation. It can be seen from Fig. 2.6 that there is a correspondence between the curves for  $V_n$  and the  $V_{e,n}$ , where negative currents produce the excitation of the fibre and positive currents an inhibition.

### 2.5.1.2 Eight-electrode Setup

This simulation involved the investigation of the behaviour of the same myelinated nerve fibre (depth  $z = 1.5$  mm) using all electrodes in the eight-electrode array. The electrode currents  $I_{el,1}$  to  $I_{el,8}$  were -0.43, -0.453, 0.36, 0.23, -0.024, 0.36, -0.047 and -0.004 mA. These values were randomly created using a uniform distribution within the interval  $(-5, 5)$  mA rejecting patterns whose sum was not approximately zero (taking into consideration the safety constraint), thus using more likely low currents than high currents. This ensures that no currents will flow deeply in the human body, which can cause tissue damage [42]. In the FEM, the overall effect of the eight-electrode array is determined using superposition.

The stated stimulus and the generated response are shown in Fig. 2.7, from which it may again be observed that proximity to an anodic stimulation (from the third, fourth and sixth electrodes) is associated with an increase in the extracellular potential  $V_{e,n}$  and a hyperpolarisation of the nerve fibre (green areas from 11 to 14 mm and 16 to 18 mm). Equivalently, proximity to a cathodic stimulation (from the other five electrodes) decreases  $V_{e,n}$ , depolarising the fibre (red areas covering the first, second, fifth, seventh and eighth electrode). The modelled membrane potential again matches  $V_{e,n}$ .



(a) Electrode currents

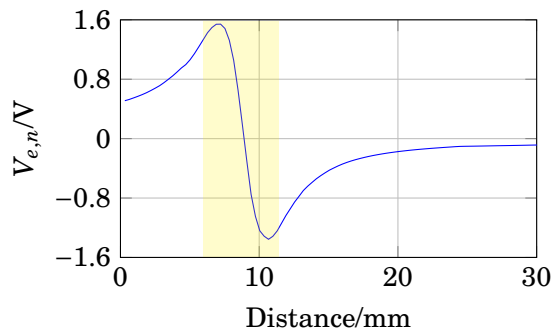
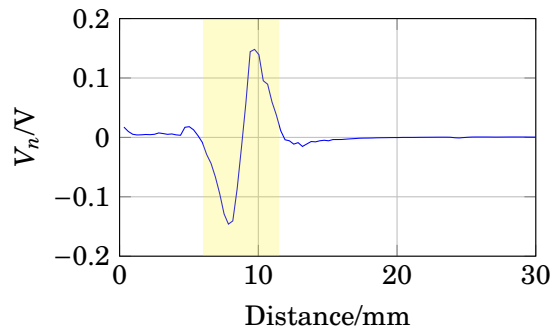

 (b) Extracellular potential  $V_{e,n}$ 

 (c) Membrane potential  $V_n$  with  $z = 1.5$  mm

Figure 2.6: ES simulation of a nerve fibre located at 1.5 mm depth using two electrodes, 1 ms after stimulus onset. (a) corresponds to the electrode currents, (b) to the extracellular potential  $V_{e,n}$  and (c) to the membrane potential  $V_n$  with depth  $z = 1.5$  mm.

### 2.5.2 Selective Stimulation

The first analysed case is based on the aforementioned experimental findings by Yem and Kajimoto [99], and aims at demonstrating that the present simulation environment has a sufficient level of detail to replicate their experimental results. Yem and Kajimoto showed in their experiments that an anodic stimulation mainly produced a vibration sensation, and that a cathodic stimulation provided both vibration and pressure sensations [99]. Physiological findings

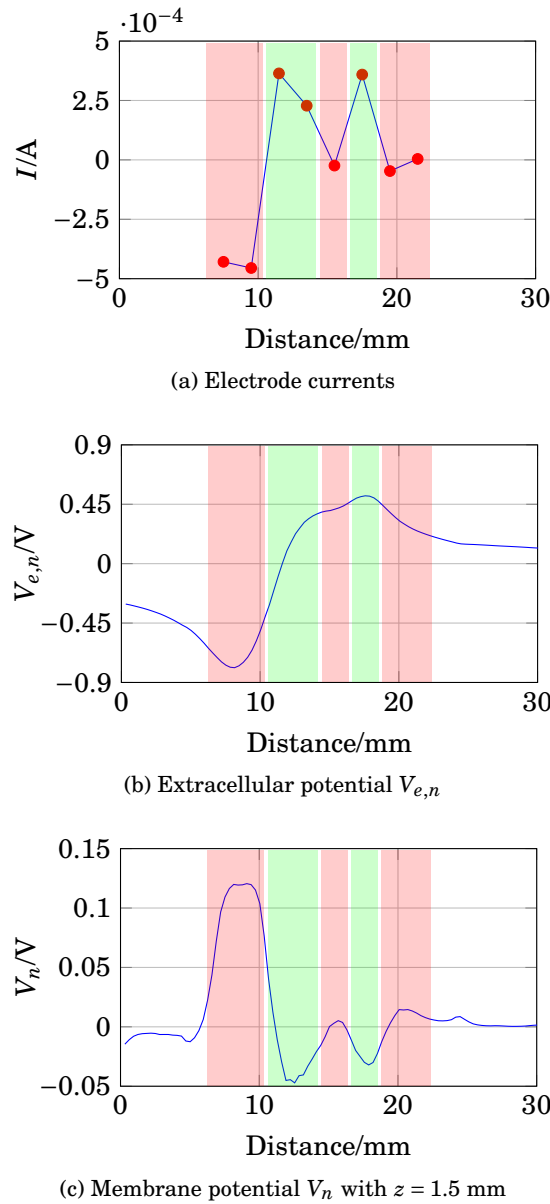


Figure 2.7: ES simulation of a nerve fibre located at 1.5 mm depth using eight electrodes, 1 ms after stimulus onset. (a) corresponds to the electrode currents, (b) to the extracellular potential  $V_{e,n}$  and (c) to the membrane potential  $V_n$  with depth  $z = 1.5$  mm.

indicate that Merkel cells respond to vibration and Meissner corpuscles to pressure, and that the nerves connected to Merkel cells run parallel to the skin and nerves connected to Meissner corpuscles run firstly perpendicular to the skin before changing to a parallel orientation [8, 9]. Fig. 2.8 illustrates the fibres connected to Meissner corpuscles in plane A (running perpendicular to the skin) and the fibres connected to Merkel discs in plane B (running parallel to the skin). Following these assumptions, one nerve fibre ( $N_1$ ) is simulated to run parallel to the skin at 1.5 mm depth (representing a fibre from a Merkel cell) and a second nerve fibre ( $N_2$ ) is simulated



to run perpendicular to the skin from 1 to 1.5 mm depth and then parallel to the skin at 1.5 mm depth (representing a fibre from a Meissner corpuscle) using eight active electrodes.  $N_2$  was located directly under the fourth electrode.

A nerve is considered activated if the AP generated at any location propagates towards the modelled nerve ending that simulates running towards the CNS. Similarly, a nerve is considered inhibited if there is no AP propagating towards the aforementioned nerve ending. The generated AP that propagates towards the mechanoreceptor (other modelled nerve ending) is not taken into account, since it does not reach the CNS to be processed and the specific effects that it could have on the mechanoreceptor have not been documented.



Figure 2.8: Distribution of the superficial corial plexus, divided into a part with perpendicular orientation that supplies Meissner corpuscles and a second part with parallel orientation that supplies Merkel discs. Taken from [9].

Further, and motivated by experiments performed by Kajimoto et al. that showed selective stimulation of three different types of mechanoreceptors [41], a second case consisting of two nerve fibres running parallel to the skin located at 1.5 mm depth ( $N_1$ ) and 2 mm depth ( $N_3$ ) is simulated, representing nerve fibres from a Merkel and a Pacinian receptor (assuming that fibres from Pacinian receptors run parallel to the skin, deeper than those from Merkel and Meissner receptors [9]). The main objective of this scenario (using eight active electrodes) was to check if the present simulation environment provides similar results when compared to the experimental findings by Kajimoto et al. [41]. The response of all fibres was traced in distance and time.

### 2.5.2.1 Selective Stimulation With a Parallel and a Perpendicular Nerve Fibre

Anodic or cathodic stimulation requires a small electrode to deliver the stimulation current and a large electrode to provide the return current path [99]. Thus, using the 8-electrode system

outlined above (Fig. 2.4), the fourth electrode was set as the main stimulation point and the other seven electrodes provided the return path, effectively acting as a larger return electrode.

Firstly, an anodic stimulation was simulated by setting the electrode currents  $I_{el,1}$  to  $I_{el,8}$  to -0.01, -0.01, -0.01, 0.07, -0.01, -0.01, -0.01 and -0.01 mA (panel (a) in Fig. 2.9). The extracellular potential  $V_{e,n}$  is illustrated in (b) and (c) as a function of distance (millimetres) along the parallel nerve fibre (panel (b) in Fig. 2.9) and perpendicular nerve fibre (panel (c) in Fig. 2.9). The membrane potential  $V_n$  is shown in (d) and (e) as a function of distance along  $N_1$  (panel (d) in Fig. 2.9) and  $N_2$  (panel (e) in Fig. 2.9). The results fit to the experimental findings of Yem and Kajimoto [99], showing the anodic stimulation to activate the perpendicular fibre  $N_2$  and to inhibit the parallel fibre  $N_1$ , as depicted in (d) and (e) in Fig. 2.9.  $N_2$  was considered activated due to the propagation of the excitation along the perpendicular and parallel portions of the nerve fibre towards the CNS, as shown in (b) in Fig. 2.10 and Fig. 2.11. Similarly, (a) in Fig. 2.10 and Fig. 2.11 show that there is no spike propagation along the parallel fibre  $N_1$  (thus, it is considered inhibited). Fig. 2.11 illustrates the shape of the action potential generated in  $N_2$  in the last node, denoting its propagation towards the CNS (categorising the fibre as activated). The second setup used 0.03, 0.03, 0.03, -0.21, 0.03, 0.03, 0.03 and 0.03 mA for the electrode currents  $I_{el,1}$  to  $I_{el,8}$ , presenting a cathodic stimulation around the fourth electrode (panel (a) in Fig. 2.12). The extracellular potential  $V_{e,n}$  is displayed in (b) and (c) as a function of distance (millimetres) along the parallel fibre  $N_1$  (panel (b) in Fig. 2.12) and the perpendicular fibre  $N_2$  (panel (c) in Fig. 2.12), and the membrane potential  $V_n$  is shown in (d) and (e) as a function of distance along  $N_1$  (panel (d) in Fig. 2.12) and  $N_2$  (panel (e) in Fig. 2.12). The responses are also consistent with Yem and Kajimoto's experimental results [99], showing the activation of both fibres (Fig. 2.13 and Fig. 2.14). Fig. 2.14 illustrates the shape of the action potentials generated in  $N_1$  and  $N_2$  in the last node, denoting their propagation towards the CNS (categorising the fibres as activated).

### 2.5.2.2 Selective Stimulation With Two Parallel Nerve Fibres

The effect of different excitation patterns was determined by testing 1000 randomised patterns for the injected currents. The patterns were generated using a uniform distribution within the interval  $(-5, 5)$  mA, rejecting patterns whose sum was not approximately zero (taking into consideration the safety constraint), thus using more likely low currents than high currents. A nerve activation was considered to be valid if the excitation propagated to that end of the fibre (at the location labelled 30 mm) which represents a connection to the CNS. Likewise, a nerve was considered inhibited when no action potential was found in the last node (end towards the CNS).

The selective stimulation of the shallower nerve  $N_1$  was achieved in three main scenarios: from the 1000 patterns, five tests showed that the stimulus was not sufficient to produce a significant excitation in  $N_3$  (the fibre showed minimal change in its membrane potential), but  $N_1$  was activated; 20 tests with the last electrode injecting a positive current produced an action potential in  $N_1$ , but resulted in a negative membrane potential in  $N_3$  which inhibited excitation

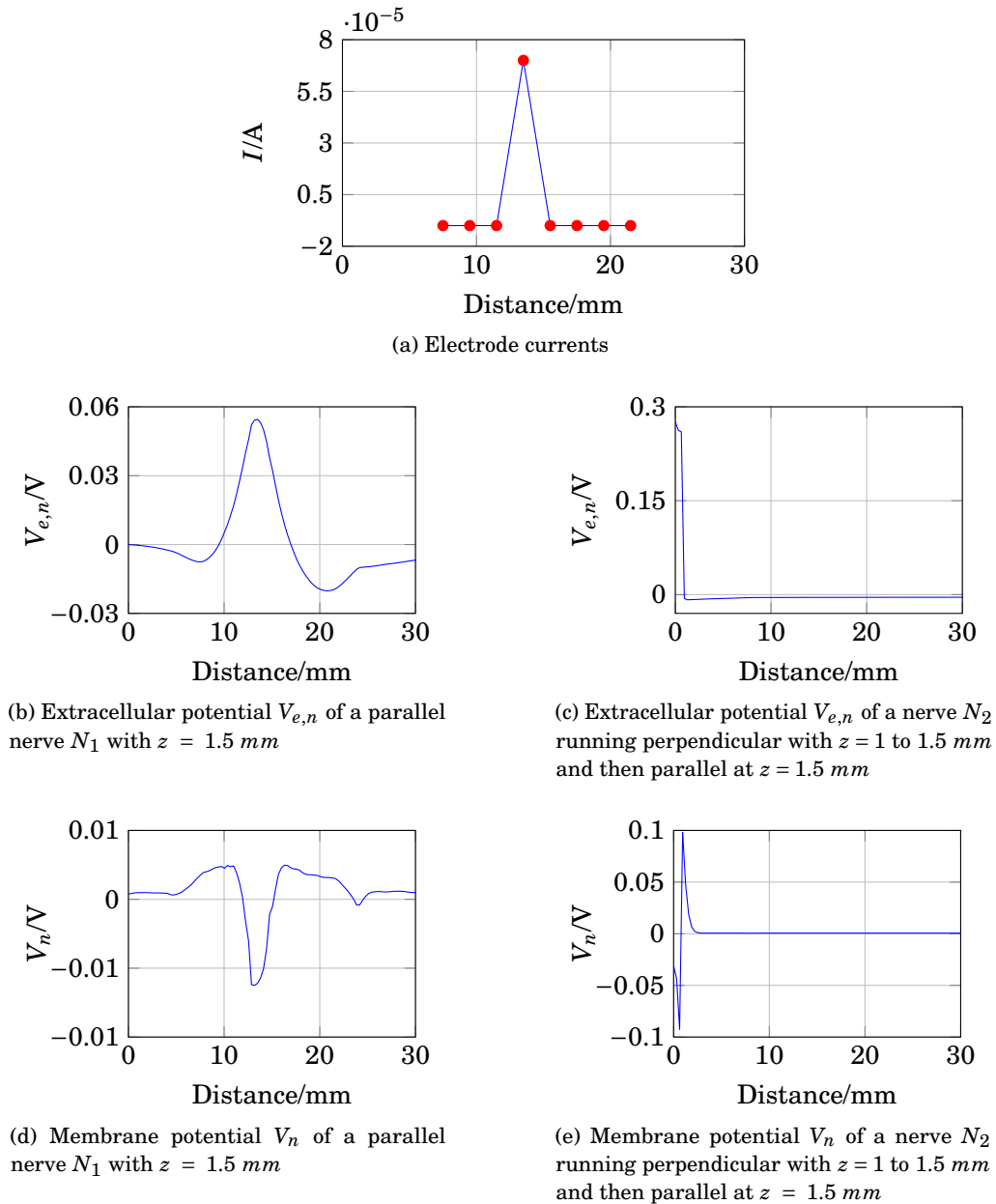


Figure 2.9: Anodic ES simulation of a nerve fibre running parallel to the skin at 1.5 mm depth ( $N_1$ ) and a nerve fibre running perpendicular from 1 to 1.5 mm depth and then parallel to the skin at 1.5 mm depth ( $N_2$ ) at 1 ms after stimulus onset. (a) corresponds to the electrode currents, (b) and (c) to the extracellular potentials  $V_{e,n}$  and (d) and (e) to the membrane potentials  $V_n$  as functions of distance (millimetres). Figure shows the efficient depolarisation of  $N_2$  and inhibition of  $N_1$ . In panels (b), (c), (d) and (e), the horizontal axis represents distance along the nerve, for  $N_1$  shown in (b) and (d), distance along the nerve corresponds to distance along the skin, as in panel (a); but for  $N_2$  in panels (c) and (e), which originates under the 4th electrode and runs first perpendicular to and then parallel to the skin, distance along the nerve is offset with respect to distance along the skin in (a).

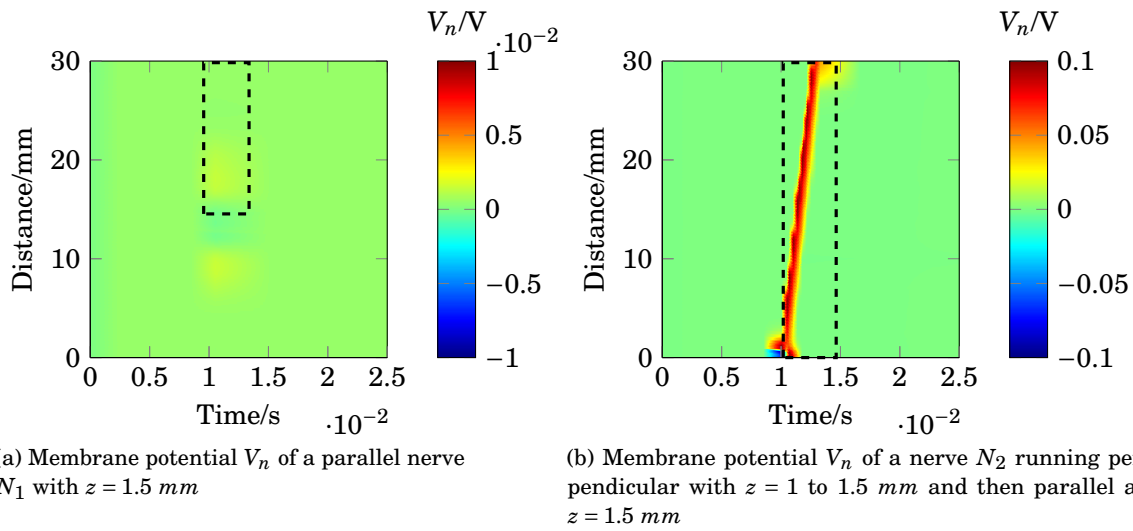


Figure 2.10: Anodic ES simulation of a nerve fibre running parallel to the skin at 1.5 mm depth ( $N_1$ ) and a nerve fibre running perpendicular from 1 to 1.5 mm depth and then parallel to the skin at 1.5 mm depth ( $N_2$ ) showing the responses through time. (a) shows the lack of an action potential in the membrane potential  $V_n$  of  $N_1$  (hence considered inhibited). (b) corresponds to the membrane potential  $V_n$  of  $N_2$ , highlighting the excitation and travelling of the spike towards the end of the modelled nerve fibre (propagating towards the CNS, thus considered activated).

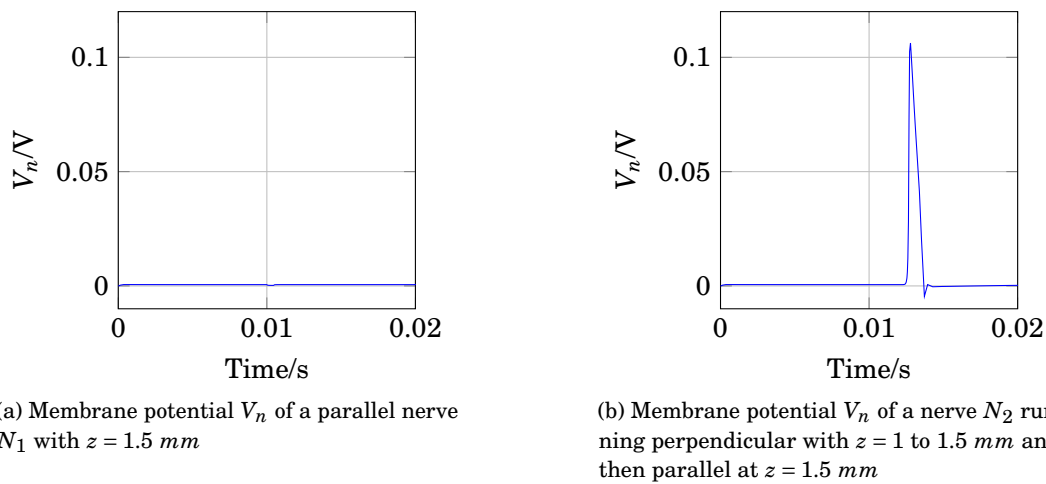


Figure 2.11: Anodic ES simulation of a nerve fibre running parallel to the skin at 1.5 mm depth ( $N_1$ ) and a nerve fibre running perpendicular from 1 to 1.5 mm depth and then parallel to the skin at 1.5 mm depth ( $N_2$ ) showing the response of the fibres in the last node (end towards the CNS) through time. (a) shows the lack of an action potential in the last node of the membrane potential  $V_n$  of  $N_1$  (hence considered inhibited). (b) corresponds to the membrane potential  $V_n$  of the last node of  $N_2$ , where the shape of the action potential is shown, thus indicating the activation of the fibre due to the propagation of the spike towards the CNS.

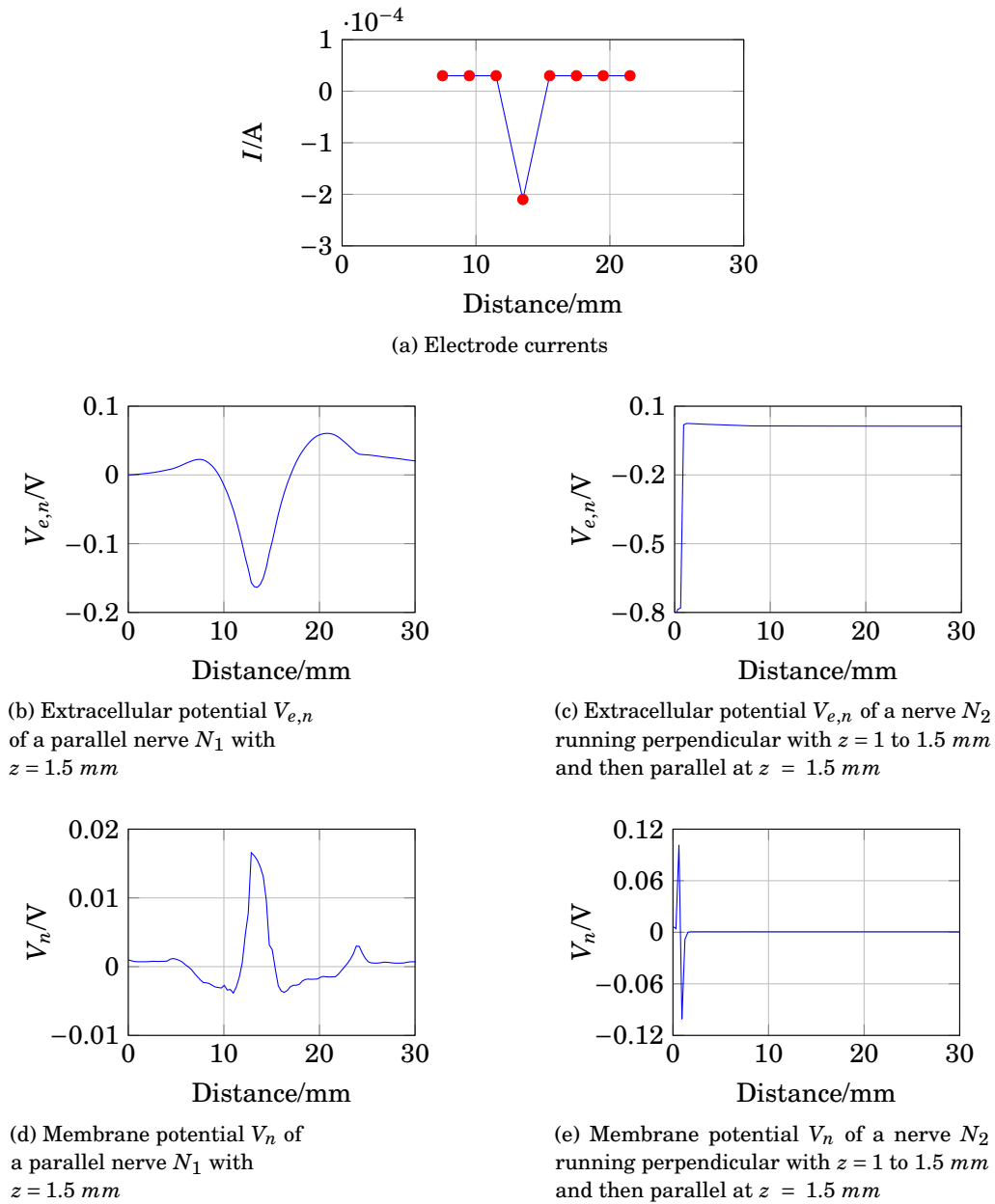


Figure 2.12: Cathodic ES simulation of a nerve fibre running parallel to the skin at 1.5 mm depth ( $N_1$ ) and a nerve fibre running perpendicular from 1 to 1.5 mm depth and then parallel to the skin at 1.5 mm depth ( $N_2$ ) at 1 ms after stimulus onset. (a) corresponds to the electrode currents, (b) and (c) to the extracellular potentials  $V_{e,n}$  and (d) and (e) to the membrane potentials  $V_n$  as functions of distance (millimetres). Figure shows the depolarisation of  $N_1$  and  $N_2$ . In panels (b), (c), (d) and (e), the horizontal axis represents distance along the nerve, for  $N_1$  shown in (b) and (d), distance along the nerve corresponds to distance along the skin, as in panel (a); but for  $N_2$  in panels (c) and (e), which originates under the 4th electrode and runs first perpendicular to and then parallel to the skin, distance along the nerve is offset with respect to distance along the skin in (a).

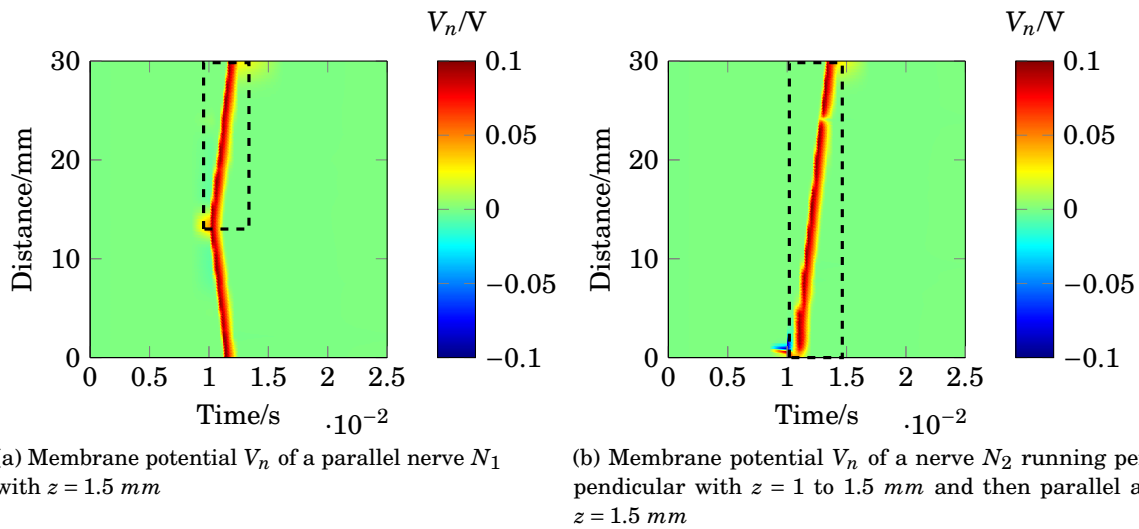


Figure 2.13: Cathodic ES simulation of a nerve fibre running parallel to the skin at 1.5 mm depth ( $N_1$ ) and a nerve fibre running perpendicular from 1 to 1.5 mm depth and then parallel to the skin at 1.5 mm depth ( $N_2$ ) showing the responses through time. (a) corresponds to the membrane potential  $V_n$  of  $N_1$  and (b) to the membrane potential  $V_n$  of  $N_2$ . The excitations and the traveling of the spikes towards the end of both nerve fibres (towards the CNS, hence considered activated) are highlighted.

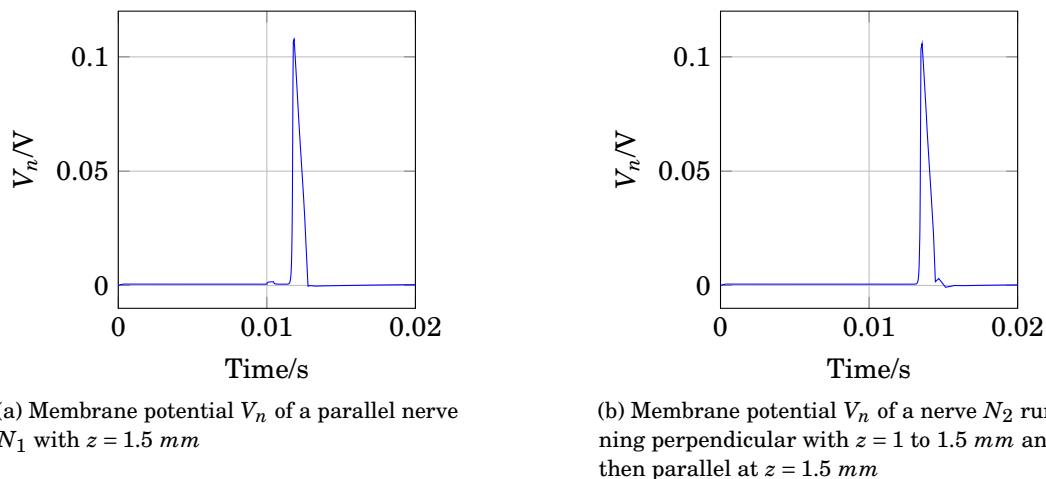


Figure 2.14: Cathodic ES simulation of a nerve fibre running parallel to the skin at 1.5 mm depth ( $N_1$ ) and a nerve fibre running perpendicular from 1 to 1.5 mm depth and then parallel to the skin at 1.5 mm depth ( $N_2$ ) showing the responses of the fibres in the last node (end towards the CNS) through time. (a) corresponds to the membrane potential  $V_n$  of the last node of  $N_1$  and (b) to the membrane potential  $V_n$  of the last node of  $N_2$ . In both panels it can be seen an action potential, which denotes the activation of the fibres.

of the fibre; and five tests with the last electrode injecting a negative current showed a cathodic block in  $N_3$  and an action potential in  $N_1$  as an “overshoot” [74] of the cathodic stimulation.

Fig. 2.15, Fig. 2.16 and Fig. 2.17 describe an example for each scenario. For all three cases, Fig. 2.15, Fig. 2.16 and Fig. 2.17 show the response of both nerve fibres, illustrating the applied currents the modelled membrane potential in the nodes, showing an action potential propagating towards the end of the fibre (around 30 mm) in all cases for  $N_1$  (thus considered activated), and no excitation in  $N_3$  (considered inhibited).

In Fig. 2.15 a positive membrane potential is observed in both fibres  $N_1$  and  $N_3$  around 21 to 23 mm, highlighted in red in panels (b) and (c), deriving from the negative current at the last electrode. However, this excitation results in an action potential only in  $N_1$ , which is shown in panel (d) in Fig. 2.15, propagating towards the end of the nerve (CNS).  $N_3$  is classified as inhibited as a result of the lack of action potential travelling to the CNS, as observed in panel (e).

The second example for selective stimulation of  $N_1$  is described in Fig. 2.16, which shows that the positive current at the last electrode produces a negative membrane potential in both fibres around 21 to 23 mm, highlighted in blue in panels (b) and (c), together with an adjacent positive “overshoot” [74] in the shallower nerve  $N_1$  around 24 mm. This results in an inhibition (no action potential) of  $N_3$  (depicted in panel (e) in Fig. 2.16), but the positive membrane potential in  $N_1$  originates an action potential that travels towards the CNS, detailed in panel (d).

Fig. 2.17 corresponds to the last case of selective stimulation of  $N_1$ , where a positive membrane potential is observed in both fibres  $N_1$  and  $N_3$  around 18 to 22 mm, highlighted in red in panels (b) and (c), together with an adjacent negative “overshoot” [74] at around 24 mm. These features derive from the negative current at the last two electrodes. As a result,  $N_3$  shows a cathodic block (no action potential is propagating towards the CNS, as depicted in panel (d)), but a positive membrane potential is generated in  $N_1$ , producing an action potential propagating towards the end of the nerve (CNS), shown in panel (e).

Regarding the selective stimulation of  $N_3$ , two scenarios were observed, both involving inhibition of all excitations in  $N_1$ , but not in  $N_3$ : 23 cases out of the 1000 tests were found with the last electrode injecting a positive current (producing a negative potential in both fibres that stopped any excitation generated in  $N_1$ , but was not sufficient to stop the travelling of the action potential generated in  $N_3$  from the previous electrodes); and two cases with the last electrode injecting negative current (inducing a cathodic block in  $N_1$ , stopping the excitation of the fibre, but the cathodic stimulation was not sufficient to stop the action potential generated in  $N_3$ ). Examples of the two scenarios are illustrated in Fig. 2.18 and Fig. 2.19, clearly showing an action potential in all cases for the last node in  $N_3$  (thus considered activated), and no activation in  $N_1$  (thus considered inhibited).

In Fig. 2.18 a negative membrane potential is observed in both fibres  $N_1$  and  $N_3$  around 21 to 23 mm, highlighted in blue in panels (b) and (c), deriving from the positive current at the last electrode. This results in an inhibition (the action potential generated from the previous

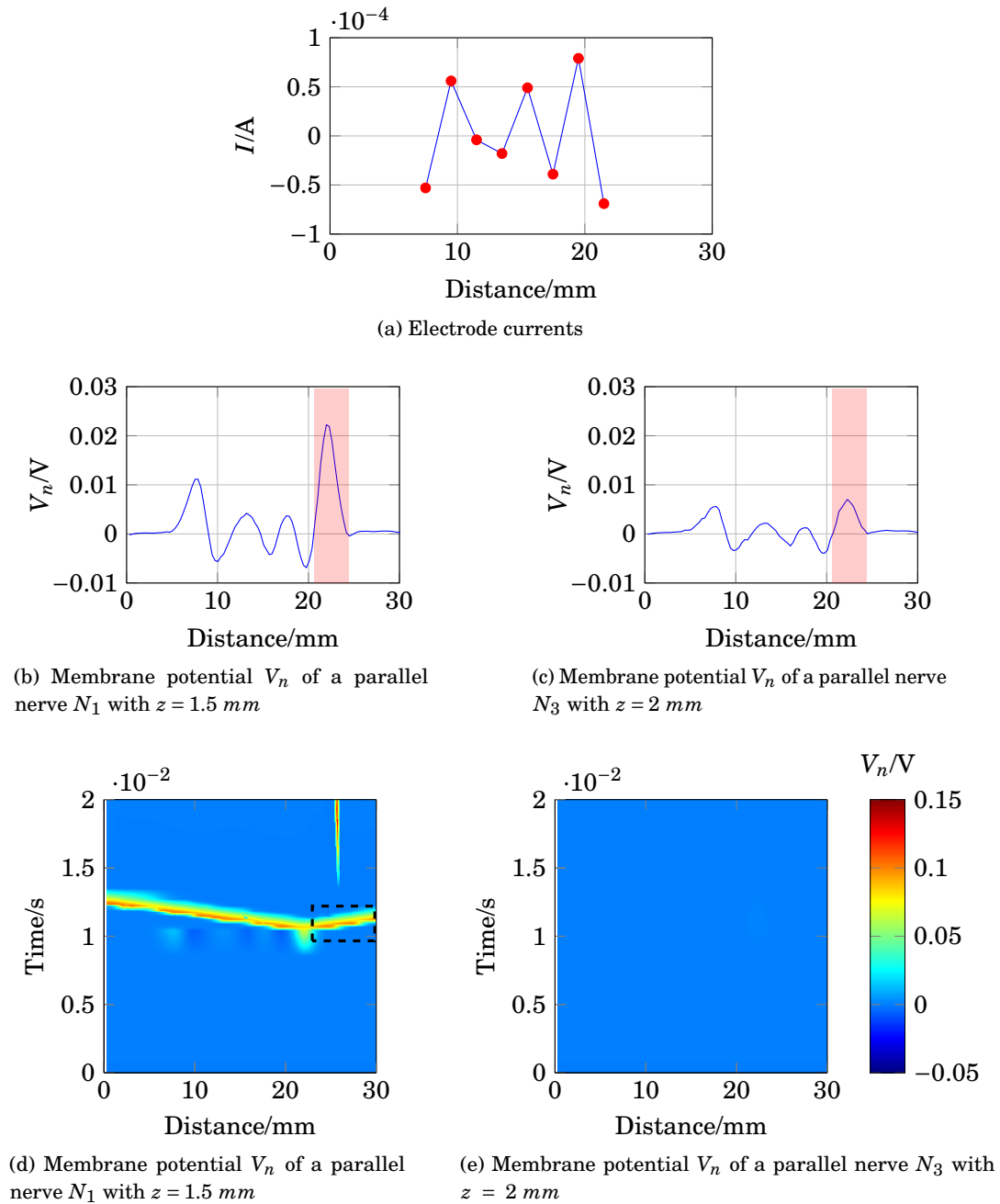


Figure 2.15: First example of selective stimulation of the shallower nerve fibre  $N_1$ . (a) shows the electrode currents. (b) and (c) illustrate the membrane potential  $V_n$  of  $N_1$  and  $N_3$ , respectively, 1 ms after stimulus onset. (d) and (e) correspond to the time courses of the excitations; it can be seen (region indicated by dotted lines) that an excitation (shown in red) propagates towards the nerve ending (CNS) in  $N_1$  (thus considered activated), as shown in (d), but not in  $N_3$  illustrated in (e) (thus considered inhibited).

electrode is stopped) only in  $N_1$ , shown in panel (d); while the action potential in  $N_3$  continues to propagate towards the end of the nerve, as depicted in panel (e).



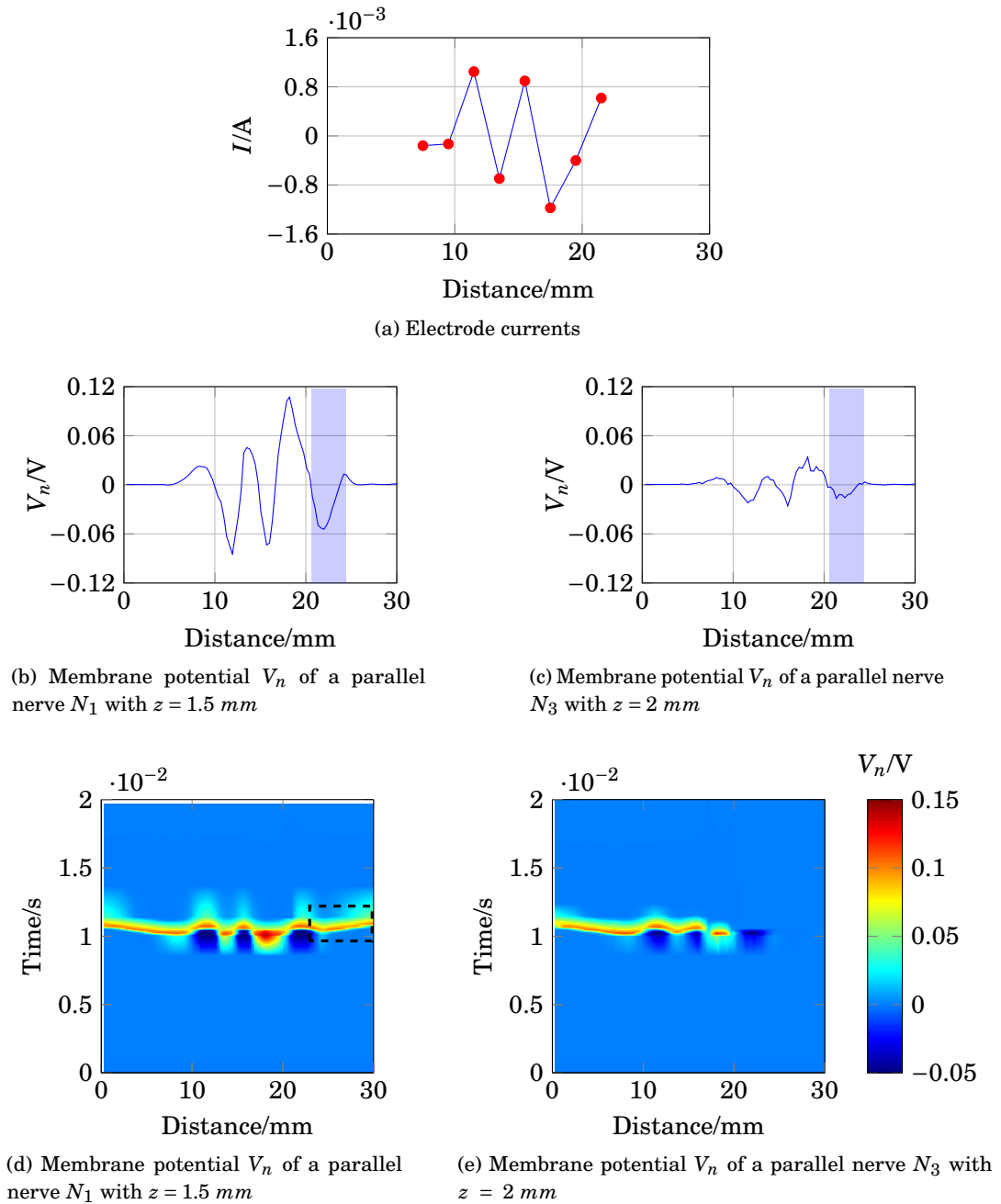


Figure 2.16: Second example of selective stimulation of the shallower nerve fibre  $N_1$ . (a) shows the electrode currents. (b) and (c) illustrate the membrane potential  $V_n$  of  $N_1$  and  $N_3$ , respectively, 1 ms after stimulus onset. (d) and (e) correspond to the time courses of the excitations; it is shown in the region indicated by dotted lines in (d), that an excitation (shown in red) propagates towards the nerve ending (CNS) in  $N_1$  (thus considered activated), but not in  $N_3$ , illustrated in (e) (thus considered inhibited).

The second example for selective stimulation of  $N_3$  is shown in Fig. 2.19, where a positive membrane potential is observed in both fibres  $N_1$  and  $N_3$  around 21 to 23 mm, highlighted in red

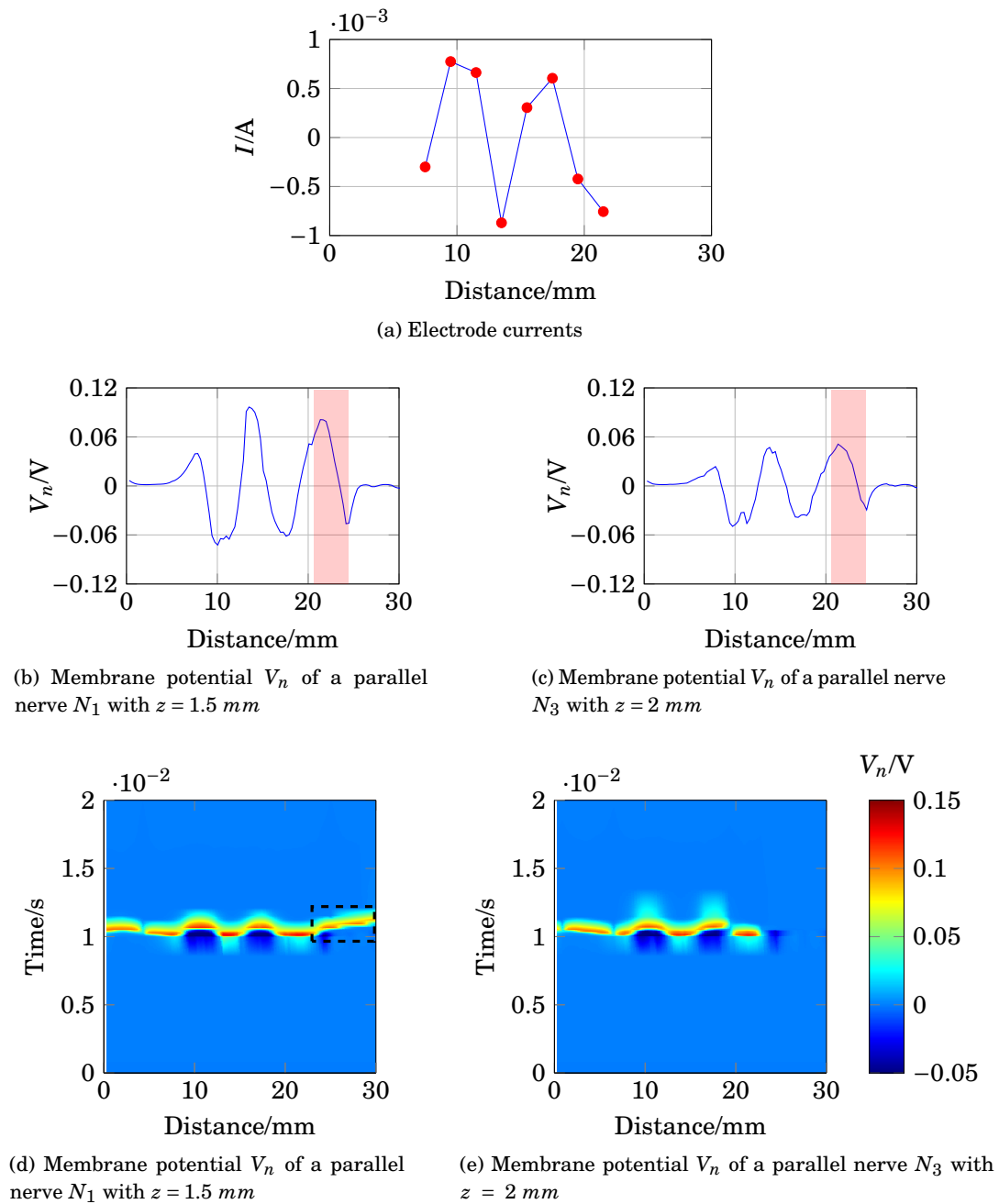


Figure 2.17: Third example of selective stimulation of the shallower nerve fibre  $N_1$ . (a) shows the electrode currents. (b) and (c) illustrate the membrane potential  $V_n$  of  $N_1$  and  $N_3$ , respectively, 1 ms after stimulus onset. (d) and (e) correspond to the time courses of the excitations; the region indicated by dotted lines in (d) demonstrates that an excitation (shown in red) propagates towards the nerve ending (CNS) in  $N_1$  (thus considered activated), but not in  $N_3$ , illustrated in (e) (thus considered inhibited).

in panels (b) and (c), together with an adjacent “overshoot” [74] at around 24 mm in  $N_1$ . These features derive from the negative current at the last electrode. The hyperpolarisation in  $N_1$  stops

the action potential from propagating towards the CNS, as observed in panel (d) in Fig. 2.19; the corresponding hyperpolarisation in  $N_3$  is minimal, and not strong enough to prevent an action potential from travelling to the end of the nerve, as shown in panel (e).

A fibre can be activated with either a single cathodic or anodic stimulation [74], and the modelling results suggest that the selective stimulation of a specific parallel fibre is mostly dependent on the stimulation provided by the last two electrodes. This suggests that similar excitations to those described above might be produced using less than eight electrodes. To investigate this, two trials were run, modifying the currents used for the 1000 tests so that only the last three or the last two electrodes were activated; i.e., the rest of the electrodes carried no current. With three electrodes, the seventh and eighth electrodes kept their original current values, and the sixth electrode carried a current to balance these two; similarly, with two electrodes, the eighth electrode kept its original current value, and the seventh electrode carried the inverse, to balance this. Results showed that it was indeed possible to selectively stimulate either fibre using fewer active electrodes. However, the number of cases of interest (selective activation of  $N_3$ ) dropped as the number of electrodes was reduced. When using three active electrodes targeting the selective activation of  $N_1$ , 14 cases produced no significant response in  $N_3$  (as in Fig. 2.15), 12 cases presented an anodic stimulation (as in Fig. 2.16) and 7 a cathodic stimulation (as in Fig. 2.17). For stimulating  $N_1$  with two electrodes, 37 cases produced no significant response in  $N_3$ , 6 cases had an anodic stimulation and 8 a cathodic stimulation. For selective activation of  $N_3$  with three electrodes, 15 cases showed an anodic stimulation (as in Fig. 2.18) and 4 cases a cathodic stimulation (as in Fig. 2.19). Targeting  $N_3$  with two electrodes, 5 cases had an anodic stimulation and 8 cases a cathodic stimulation.

## 2.6 Discussion

The results from the present study show that by suitable choice of electrode currents a specific nerve fibre can be selectively stimulated.

Regarding the scenario with one parallel fibre  $N_1$  and one perpendicular fibre  $N_2$ , simulation results were found to support experimental findings [99], indicating that the chosen level of complexity of the model is sufficient to capture such effects. For the cathodic stimulation, it was necessary to use currents three times greater than the currents for the anodic stimulation. This is due to the difference between the thresholds for the excitations (for the case of fingertip skin, sensation thresholds for anodic stimulation have been found to be lower than for cathodic stimulation [37]).

For the case of two parallel fibres,  $N_1$  and  $N_3$ , it has been demonstrated that stimulation currents can be chosen to excite only one of the two fibres and inhibit the other. Such selectivity was not achieved in previous studies by Kajimoto [40, 99], where stimulation of shallower fibres was always observed when deeper fibres were targeted. In fact, such unwanted stimulation of

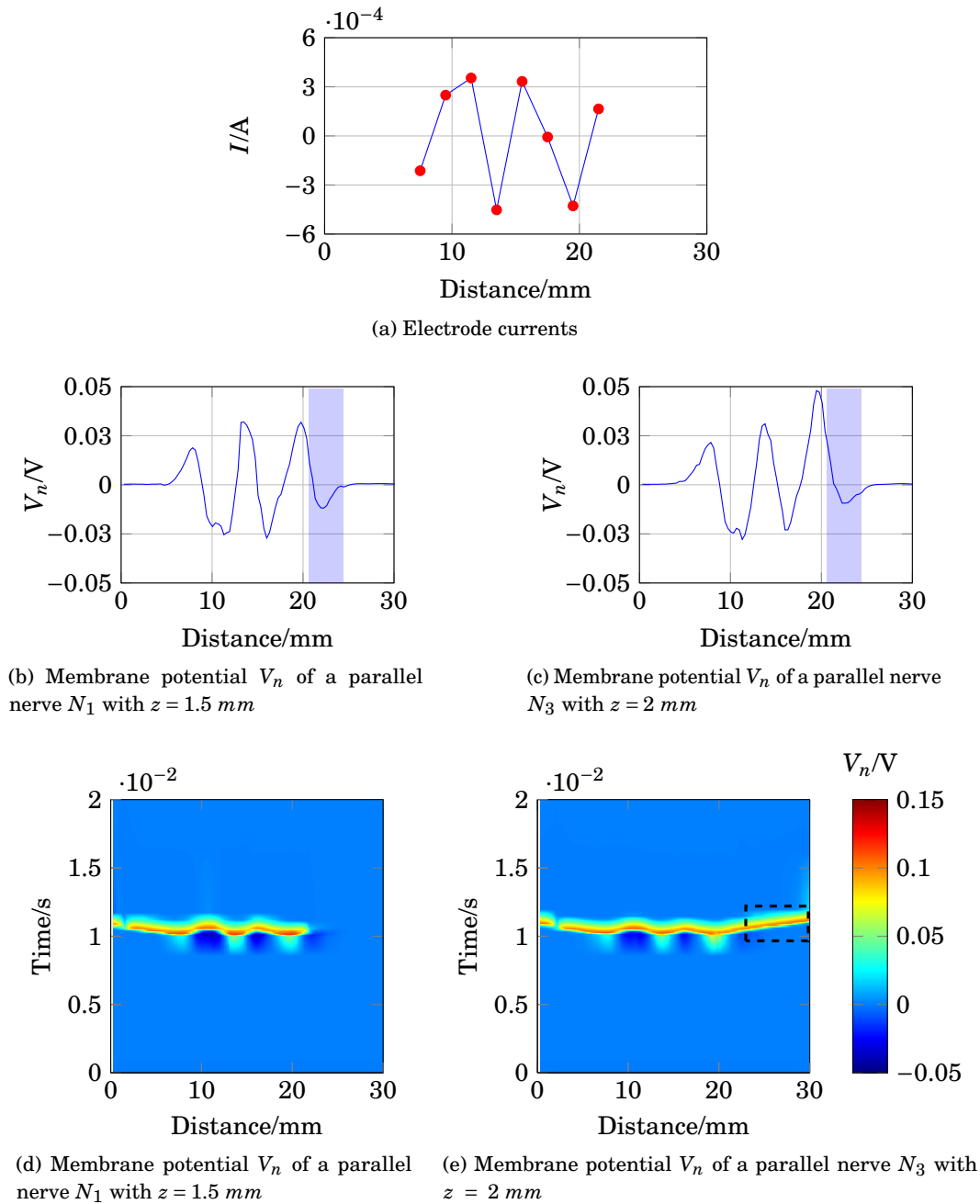


Figure 2.18: First example of selective stimulation of the deeper nerve fibre  $N_3$ . (a) shows the electrode currents. (b) and (c) illustrate the membrane potential  $V_n$  of  $N_1$  and  $N_3$ , respectively, 1 ms after stimulus onset. (d) and (e) correspond to the time courses of the excitations; it can be seen (region indicated by dotted lines) that an excitation (shown in red) propagates towards the nerve ending (CNS) in  $N_3$  as shown in (e) (thus considered activated), but not in  $N_1$  illustrated in (d) (thus considered inhibited).

shallower fibres was observed in more than 90% of the random stimulation patterns tested in the present study; however, selective stimulation of the deeper nerve fibre (inhibiting the shallower

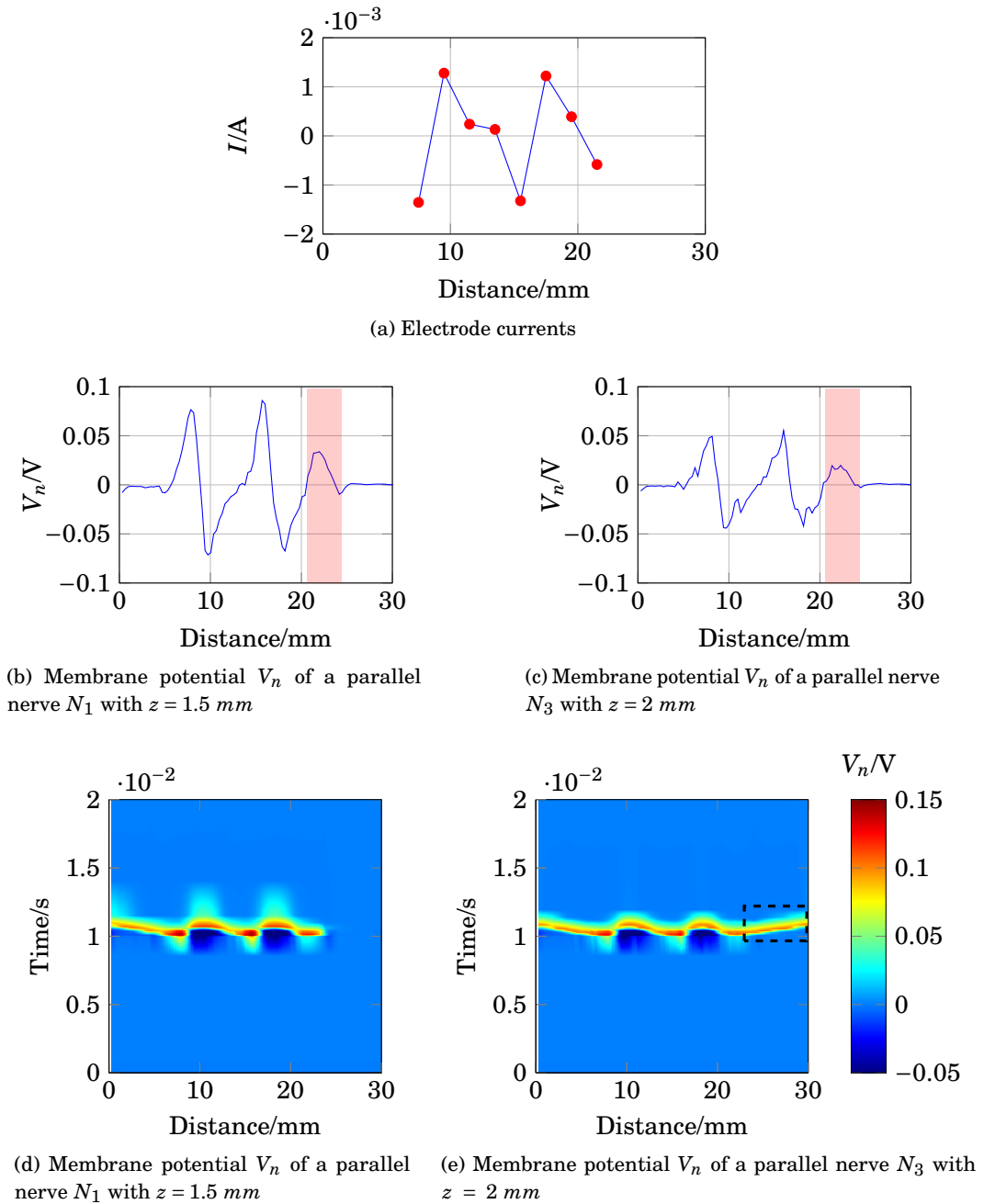


Figure 2.19: Second example of selective stimulation of the deeper nerve fibre  $N_3$ . (a) shows the electrode currents. (b) and (c) illustrate the membrane potential  $V_n$  of  $N_1$  and  $N_3$ , respectively, 1 ms after stimulus onset. (d) and (e) correspond to the time courses of the excitations; the region indicated by dotted lines in (d) shows that an excitation (in red) propagates towards the nerve ending (CNS) in  $N_1$  (thus considered activated), but not in  $N_3$ , depicted in (e) (thus considered inhibited).

nerve fibre) was possible in over 2% of cases, with appropriate stimulation patterns. To provide an explanation for this, it is necessary to look for common features in the subset of the random

stimulation patterns that is associated with selective stimulation.

Inspection of the modelled responses indicated that a fibre was activated by a stimulus which produced a positive membrane potential in approximately 10 consecutive nodes, or more. Similarly, a fibre was inhibited (stopping any previous action potential) by a stimulus which produced a negative membrane potential in at least 15 consecutive nodes (with either cathodic or anodic stimulation). As might be expected, the effectiveness of the stimulus was found to vary with the depth of the modelled fibres.

Since the excitation patterns which achieved selective stimulation did not at first sight hold clear commonalities, it was necessary to scrutinise the responses of the modelled fibres to look for shared characteristics. As supported by the simulations, there are different situations that produce selective excitation of the shallower nerve fibre  $N_1$ : a relatively weak stimulation excites  $N_1$  but not  $N_3$  (Fig. 2.15), or a stronger stimulation (anodic or cathodic) produces activation and inhibition in both nerve fibres, with a residual (final excitation) in  $N_1$  only (Fig. 2.16 and Fig. 2.17). In cases of selective stimulation of the deeper nerve, both fibres are activated (an action potential is generated), but the shallower one ( $N_1$ ) is inhibited by a hyperpolarisation in the membrane potential, produced by either the negative current responsible for the excitation (Fig. 2.19), or by positive current at the last electrode (Fig. 2.18). Investigating these cases further, it could be observed that the selectivity is in general attributable to the effect of currents from the last two electrodes, which determine the nerve's final state of excitation and/or inhibition. Excitations or inhibitions are the result of producing positive membrane potential in at least 10 consecutive nodes or a negative membrane potential in at least 15 consecutive nodes, respectively.

Results showed that it was indeed possible to selectively stimulate either fibre using fewer active electrodes. However, the number of cases of interest (selective activation of  $N_3$ ) dropped as the number of electrodes was reduced. Examination of the 8-electrode results (see examples above) suggests that selective activation of  $N_3$  is largely attributable to electrodes 7 and 8, or sometimes 6, 7 and 8. Therefore, reducing the stimuli to three electrodes disrupts some of these patterns, and reducing to two electrodes disrupts all of them, at least to some extent.

These results suggest that the simulation environment presented here could in future be used for optimisation of hardware design for selective stimulation. Although selective excitation is possible using only two or three electrodes, eight electrodes give greater flexibility in stimulus design, allowing a combination of localised activations or inhibitions at different positions in the fibre.

Summarising, the responses of the modelled fibres were consistent with preceding studies and experimental results [40, 99]. The selective stimulation results for the presented scenarios demonstrate the capabilities and extent of the simulation environment. In spite of the environment's lack of detail in some aspects of the representation, it was able to emulate known responses for modelled nerve fibres, suggesting that it can meaningfully be used to derive new hypotheses for future testing in psychophysical studies.

## **2.7 Conclusion**

As demonstrated throughout this chapter, the presented simulation environment provides an important tool for studying TENS in general and selective nerve stimulation in particular. It allows investigation of the design of electrode arrays for a TENS system in terms of electrode shape, spacing and number of electrodes, as well as studying the effect of different stimulation patterns. There is also a possibility of modelling nerves situated deeper than those considered in the present study; e.g., motor nerves. The presented model is a simplified representation of a human finger. Its level of complexity, however, was shown to be sufficient to produce simulation results that agree well with experimental results known from literature [40, 99].

## HARDWARE OF TENS SYSTEMS

In this chapter different tactile displays are compared, focusing on their hardware specifications and purposes. Next, the description of the design and hardware implementation for the previously modelled TENS system is presented. Different versions of the hardware design are included and evaluated, and the final layout of the circuit boards of the system is illustrated.

### 3.1 Tactile Displays

Tactile displays are defined as human-computer interfaces that convey to the user's skin reproduced tactile features of an object. They can be categorised according to the tactile sensation they provide or to the type of actuation they use. Regarding the type of actuation, the systems can be divided into mechanical energy devices and electrotactile stimulating devices. The mechanical devices comprise vibration-based [45, 71], focused ultrasound [33, 46], surface acoustic waves [66], air jets [59], and electro-rheological and magneto-rheological devices [58].

Kim et al. [45] developed a multi-dimensional tactile array to provide vibration, pressure and shear. The system used a set of four taxels (Figure 3.1); each taxel involved one voice coil that generated vibration and pressure, and one DC motor for rotational shear. The voice coils were controlled individually by a digital-to-analog converter (DAC) unit, two operational amplifiers and a digital potentiometer, while the DC motor was controlled by a digital EC speed controller.

Quek et al. designed a 3-degree-of-freedom skin deformation tactile device (Figure 3.2) comprising three geared DC motors assembling a Delta parallel mechanism [71]. This 3-degree-of-freedom mechanism was used for sensory substitution or augmentation of force feedback.

Hoshi et al. [33] presented a tactile display with 324 airborne ultrasound transducers in a 18x18 matrix (Figure 3.3), individually controlled in order to generate a focal point, producing a stress field in a 3D space. A second example of a tactile display using ultrasound actuators was





Figure 3.1: Internal structure of the taxel from the multi-dimensional tactile array. Taken from [45].

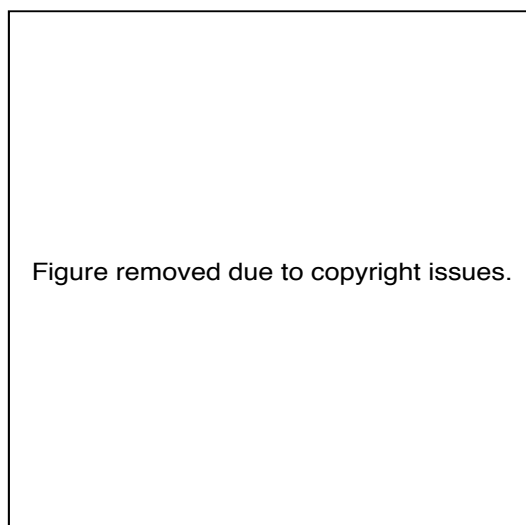


Figure 3.2: 3-Degree-of-Freedom tactile device. Taken from [71].

documented by Kim et al. [46], regarding a 4x4 piezoelectric ultrasonic actuator array (Figure 3.4) that could generate different types of texture information.

Nara et al. [66] presented a tactile display using acoustic waves generated by an interdigital transducer (IDT) that alternated voltage on a Lithium Niobate ( $\text{LiNbO}_3$ ) substrate (Figure 3.5), producing different roughness sensations. Lee et al. [59] investigated the tactile sensations resulting from a 1-point and a 4-point nozzle airflow display (Figure 3.6), showing that their performance was comparable to that of a vibrotactile display. Lee and Jang [58] developed a tactile display using magneto-rheological fluid (Figure 3.7) that could express 3D virtual surfaces using different combination of magnetic poles.

Electrotactile systems generally involve simpler hardware designs than mechanical stimulation-based tactile displays. This allows electrotactile displays to be smaller in size than the mechanical-based displays, as well as to have lower production and maintenance costs. The stimulation is controlled by specific electrical current, which can also be simpler than finely controlling mechanical actuators. Electrotactile displays use surface electrodes that target the sensory nerves

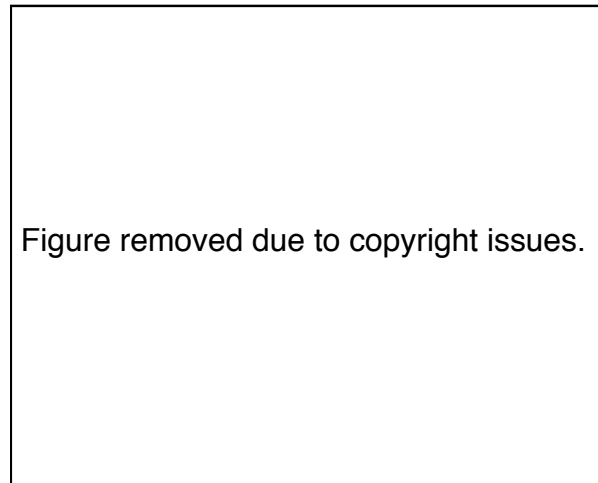


Figure 3.3: 18x18 array of airborne ultrasound transducers. Taken from [33].

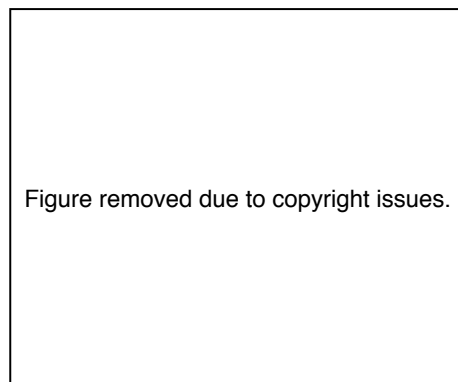


Figure 3.4: Assembled tactile display with ultrasonic actuators. Taken from [46].

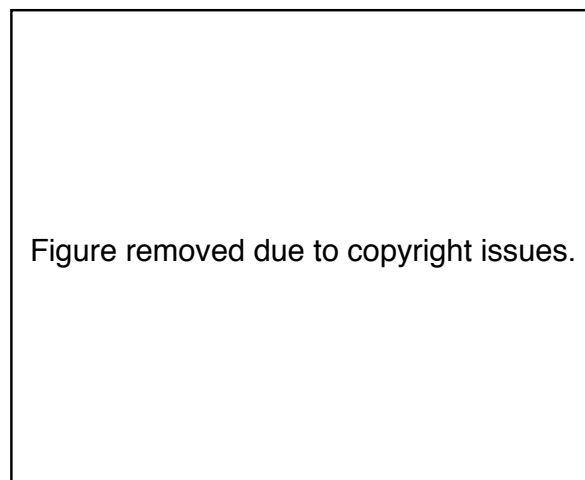


Figure 3.5: Schematic description of the surface acoustic wave tactile display. Taken from [66].

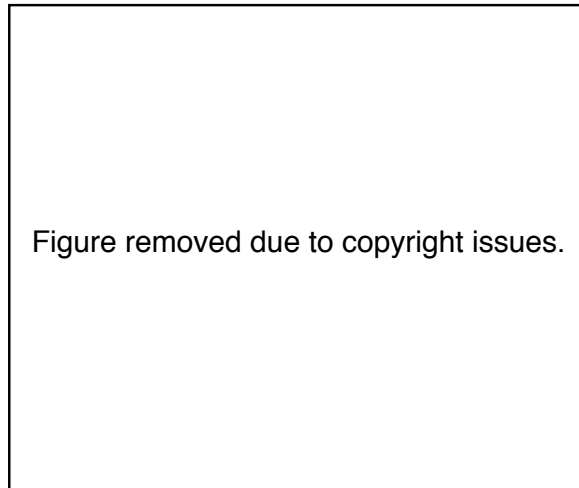


Figure 3.6: 1-point and 4-point nozzle mounts for the tactile display using airflows. Taken from [59].

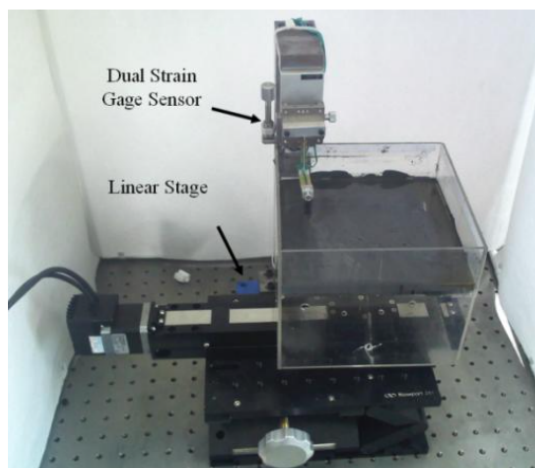


Figure 3.7: Hardware implementation of the magneto-rheological tactile display. Taken from [58], used with permission under Creative Commons license.

under the skin [76, 77]. The surface electrodes can either be a matrix or array of electrodes with different geometrical shapes [38, 39, 41, 43, 99, 101] or microneedle arrays [88].

Kitamura et al. developed an array of microneedles consisting of hydraulic amplification mechanisms and piezo-electric actuators (used as an electrode array) capable of stimulating all tactile receptors creating different tactile sensations [88]. Their system reduced the required voltage by penetrating the stratum corneum to 30 V. They used positive square pulses from a pulse generator and an Arduino MEGA to control PhotoMOS relays to switch the active electrodes at specific times.

Kajimoto et al. have documented multiple examples of systems using an array of geometrical electrodes [39, 41, 43, 99], where the systems share the same structure: a microprocessor, a high-speed analog-to-digital converter (ADC) (to control the individual switches for the electrodes) and a DAC, a voltage to current converter, switches and the electrode arrays (as depicted in Figure 3.8). The stimulating pulses are generated as voltage waveforms by the DAC and changed to a current pulse by a voltage-to-current (VI) converter, driven by a high-voltage source (300 - 350 V). The electrode arrays consisted of eight to 512 circular electrodes [39, 43, 99] or eight linear electrodes [41], providing a maximum stimulation current of 2 - 5 mA. All electrodes were in contact with the user's fingertip. These systems aimed to independently stimulate each type of mechanoreceptor [41], provide real-time impedance feedback [39], provide tactile vision substitution [43], and study the intensity of sensation and the sensation of anodic and cathodic stimulation [99].



Figure 3.8: TENS system structure documented by Kajimoto et al. [39].

Kaczmarek et al. developed another electrotactile example [38] for studying the perceived frequency and intensity of the stimuli, where a constant-current source delivered electrical pulses to the fingertip using a coaxial electrode (Figure 3.9). The system comprises a digital signal processor where the waveform is generated, an amplifier and VI converter, producing an output signal of  $-800$  to  $600$  V and  $\pm 20$  mA. Similarly, Yoshimoto et al. [101] presented an electrotactile display using a pulse generator, a VI converter, current mirrors and the electrodes (Figure 3.10),

providing electrotactile augmentation for texture modulation of real materials. The system is controlled by the computer and it produces an output up to 3 mA.

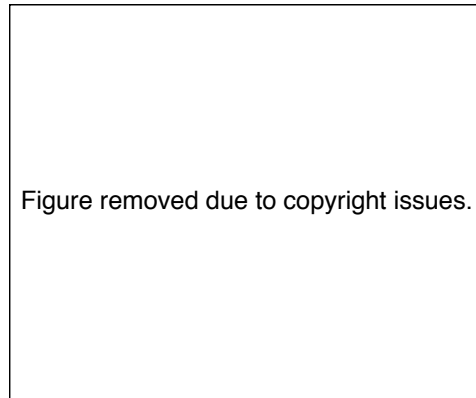


Figure 3.9: Electrotactile stimulation system developed by Kaczmarek et al. [38].

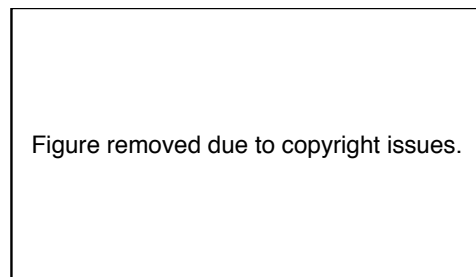


Figure 3.10: Electrotactile display structure from Yoshimoto et al. [101].

Taking into account that the electrical impedance of the skin varies due to environmental conditions and decreases with stimulation current [89], the stimulation current was chosen to be controlled in the design of the modelled TENS system (presented in chapter 2). In order to deliver stable currents regardless of variations in the impedance of the load, the designed circuit had to ensure a very high output impedance. Since the compliance voltage (range of output voltage) of the systems is typically around 150 – 300 V [78], a high-voltage source of 400 V ( $\pm 200$  V) was selected. The overall hardware structure was inspired by the examples of Kajimoto et al. [39, 41, 43, 99], having a DAC unit, VI converter and an electrode array.

## **3.2 Design and Implementation of the Hardware for the Modelled TENS System**

Based on the layout of the electrode array introduced in chapter 2, the corresponding design for the TENS hardware is developed. This system consists of three main components: a DAC unit, a VI converter and the electrode array (as depicted in Figures 3.11 and 3.12). The digital

input (driving) signal comes directly from Matlab, from the set of simulated current values that selectively stimulate a specific modelled nerve, as described in the results in chapter 2. This signal is sent to a Master Arduino Due, which shares the specific signal for each of the electrodes to four Slave Arduino Due's through I<sup>2</sup>C. The DAC units in the Slave Receivers convert the digital signal into an analog signal (voltage signal) that is then fed to the VI converter, where it is translated into a current signal. Finally, the output current is delivered to the user through each of the eight electrodes in the array. Each electrode is individually driven through one DAC and one VI converter, since it is highly important to finely control the amount of output current. All circuit boards were designed using EAGLE (<https://www.autodesk.com/products/eagle/overview>).

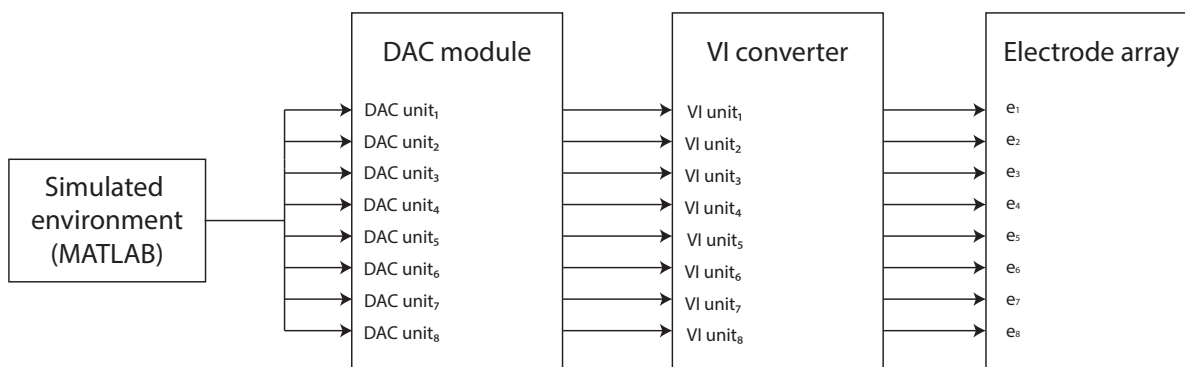


Figure 3.11: Block diagram of the electrical stimulation hardware.

### 3.2.1 Digital-to-Analog Converter Channels

Four Arduino Due boards were used, taking into account that each board has two 12-bit DAC units, to generate the eight input signals for the electrode array. Each DAC is connected to a voltage amplifier (displayed in the schematic in Figure 3.13) to condition the signal from the DAC output  $V_{DAC}$  to go from 0.55 to 2.75 V (original range) to a new range of -6 to 6 V in order to serve as input for the eight channels in the VI module ( $V_{out,DACn}$  where  $n = [1, 8]$ ). This signal conditioning allows a resolution of 0.0029 V per DAC value.

There are two copies of the voltage amplifier implemented in a circuit board that sits on top of each Arduino Due (Figure 3.14, see schematic in the Appendix). A Master Arduino Due receives all eight digital signals (corresponding to each channel or electrode) through serial communication with the computer, and then sends the corresponding information to each of the four Arduino Due's (set as Slaves) through I<sup>2</sup>C communication, since this protocol involves only a 2-wire bus (simplifying the connections and design of the whole DAC module) and allows the information to be sent quickly.

The voltage amplifier circuit acts as an unipolar to bipolar converter using a differential amplifier, with a transfer function described by equation (3.1), where  $V_1$  refers to the input voltage coming directly from the Arduino Due DAC,  $V_2$  is a reference voltage and  $n$  corresponds

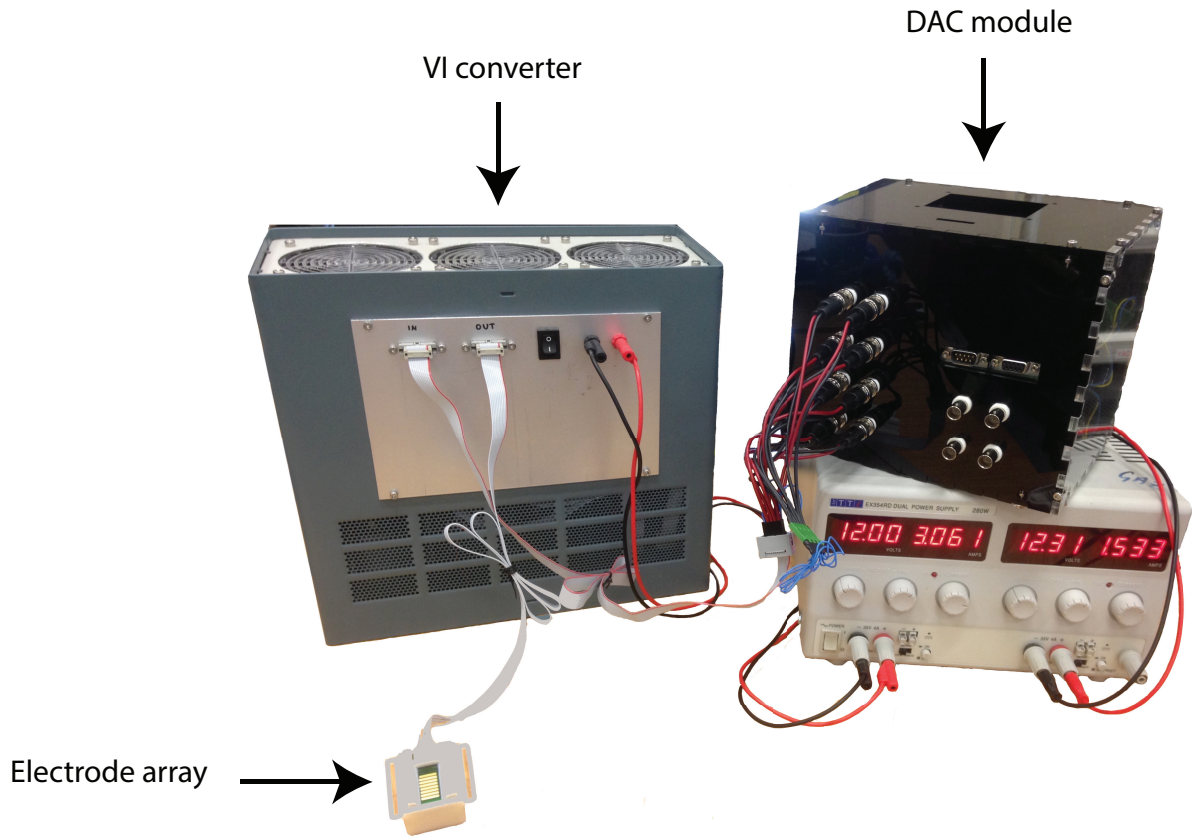


Figure 3.12: Implemented TENS hardware.

to the channel or electrode number. The gain of the amplifier is defined by equation (3.3), where the new range ( $V_{out}$  set to  $-6$  to  $6$  V) is divided over the original Arduino Due DAC range ( $V_1$  going from  $0.55$  to  $2.75$  V). The offset correction ( $V_{off}$ ), which allows an output voltage of zero volts when the same voltage is used as input, is given by equation (3.4).

The values of the resistors  $R_1$ ,  $R_2$  and  $R_4$  were chosen according to common commercial values.  $R_3$  was calculated using the amplification gain ( $A$ ) equation (3.3). The correct value for  $V_2$  is obtained using a potentiometer ( $R_5$ ) acting as a voltage divider, granting the fine movement of the signal to position it on the right offset. All the resistor values used in the DAC board are listed on Table 3.1.

$$(3.1) \quad V_{out,DACn} = V_1 \frac{R_2}{R_1 + R_2} \left( 1 + \frac{R_4}{R_3} \right) - V_2 \frac{R_4}{R_3}$$

$$(3.2) \quad V_{out,DACn} = AV_1 - V_{off}$$

$$(3.3) \quad A = \frac{V_{out,DACn,max} - V_{out,DACn,min}}{V_{1,max} - V_{1,min}}$$

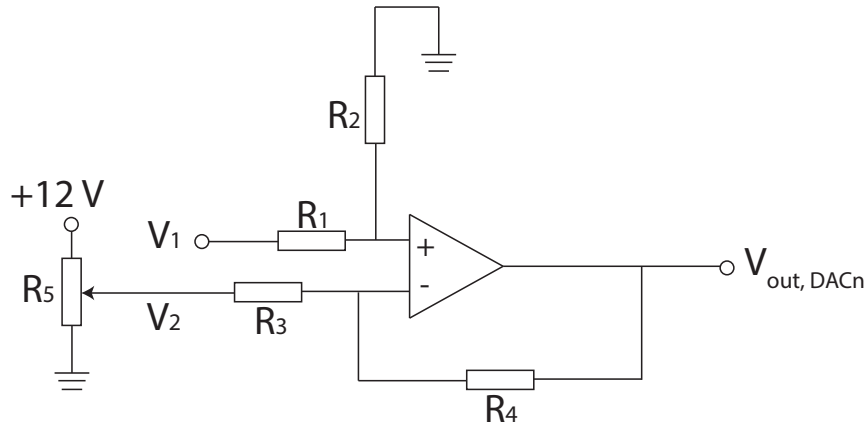


Figure 3.13: Voltage amplifier circuit connected to the Arduino Due boards to condition the output of the DAC units to a range of -6 to 6 V.

$$(3.4) \quad V_{off} = A \left( \frac{V_{out,DACn,max} - V_{out,DACn,min}}{2} + V_{DAC,min} \right)$$

Table 3.1: Resistor values used in the amplifier circuit.

Resistor	Value / k $\Omega$
$R_1$	1
$R_2$	34.8
$R_3$	1.62
$R_4$	7.5
$R_5$	2

### 3.2.2 Voltage-to-Current Converter

The next hardware component is the VI converter, one of which is needed for each electrode or channel. The VI converter is an electric circuit comprising a voltage follower or buffer amplifier acting as a voltage-controlled current source and a set of current mirrors, which ensure that the output current remains constant regardless of the load conditions. A current mirror is an electrical circuit that replicates the current flowing through an input terminal in an output terminal. Other features of a current mirror include a relatively low input resistance and a relatively high output resistance that allow both the input and output currents to stay constant.

Three versions of the VI converter were developed in order to achieve a robust design that could be used for hours keeping the output constant and avoiding damage to the electronic components (mainly due to over temperature). The electrical circuit for the first version is shown



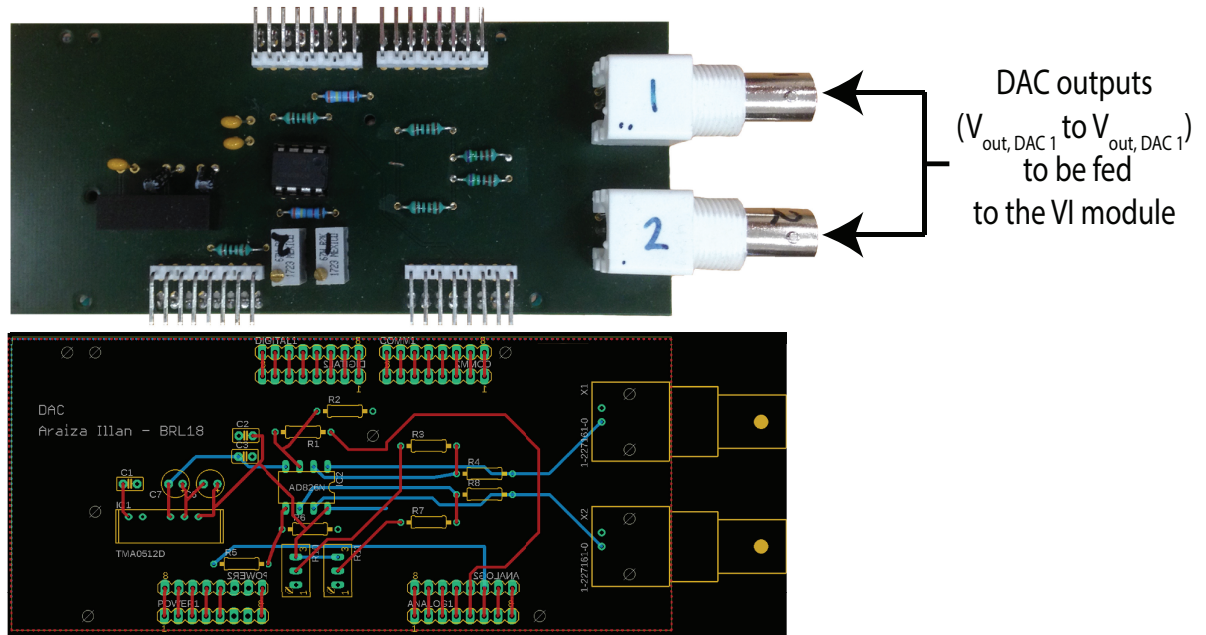


Figure 3.14: Circuit board of the two voltage amplifiers connected to the Arduino Due board to condition the output of the DAC units to a range of  $-6$  to  $6$  V. The implemented board is shown at the top and the circuit board drawing at the bottom.

in Figure 3.15, with the voltage-controlled current source (marked in green) and two current mirrors, one for positive current values (marked in red) and one for negative current values (marked in blue). The voltage-controlled current source consists of an operational amplifier and two transistors acting as switches, one NPN ( $T_1$ ) and one PNP ( $T_2$ ).

The operational amplifier has a high input impedance that leads to  $I_{01} \ll I_1$ . Thus,  $I_{01}$  can be neglected. Assuming that  $I_{01}$ ,  $I_{02}$  and  $I_{03}$  are equal to zero, the feedback to the negative input of the operational amplifier gives:

$$(3.5) \quad V_{R_1} = V_{out,DACn}$$

Ergo, the current flowing through  $R_1$  is described with:

$$(3.6) \quad I_1 = \frac{V_{out,DACn}}{R_1}$$

$T_1$  outputs positive current values towards the current mirror marked in red (Figure 3.15) when the voltage between its base and emitter ( $V_{BE}$ ) is positive at the base and negative at the emitter. Equivalently,  $T_2$  outputs negative current values towards the current mirror marked in blue (Figure 3.15) when the voltage between its base and emitter ( $V_{BE}$ ) is negative at the base and positive at the emitter. Therefore, a positive input voltage ( $V_{out,DACn} > 0$ ) leads to:

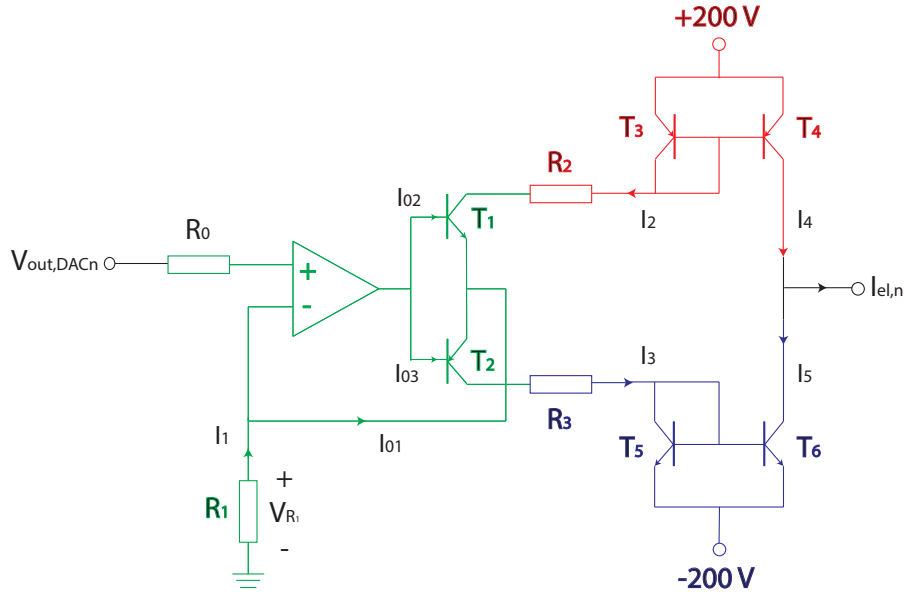


Figure 3.15: First version of the VI converter electrical circuit, comprising a voltage-controlled current source (in green) and two current mirrors (in red and blue).

$$(3.7) \quad I_2 = I_1 = \frac{V_{out,DACn}}{R_1},$$

$$(3.8) \quad I_3 = 0.$$

Whereas a negative input voltage ( $V_{out,DACn} < 0$ ) leads to:

$$(3.9) \quad I_2 = 0,$$

$$(3.10) \quad I_3 = I_1 = \frac{V_{out,DACn}}{R_1}.$$

The simple current mirror structure comprises two transistors of the same type (matching accurately either two PNP, like  $T_3$  and  $T_4$  marked in red in Figure 3.15, or two NPN, like  $T_5$  and  $T_6$  marked in blue in Figure 3.15) where, as the  $V_{BE}$  is the same, the current in both transistors is the same. One of the transistors has the base connected to the collector, acting as a diode, and both emitters are connected together to a voltage supply. Since the equations describing a PNP and NPN current mirrors are the same, only one type of mirror is further analysed. The current transfer ratio (CTR)  $\lambda$ , parameter describing the relation between the output current

and the input current ( $I_{out}/I_{in}$ , in Figure 3.16), shows the performance of the current mirror and its dependance on the transistor parameters.

The circuit for a basic BJT NPN current mirror is shown in Figure 3.16, where it can be observed that the CTR is given by:

$$(3.11) \quad \lambda_1 = 1 \pm \frac{2}{\beta} \pm \frac{V_{OS}}{V_T} - \frac{V_{\Delta Q}}{(V_I)_Q},$$

where  $\beta$  refers to the common-emitter current gain,  $V_{OS}$  to the required difference in  $V_{BE}$  to result in identical collector currents,  $V_T$  to the thermal voltage,  $V_{\Delta Q}$  to the difference in voltages between the collectors and bases  $V_{CB}$  of the transistors and  $(V_I)_Q$  to the Early intercept voltage at the operating Q-point [97].

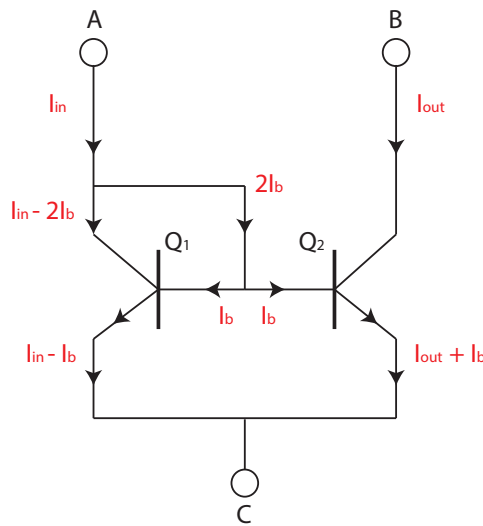


Figure 3.16: Simple NPN current mirror configuration. Modified from [97].

It can be seen in Figure 3.15 that the reference (mirrored) current of the PNP current mirror is  $I_2$  and the output (copy) current is  $I_4$ . Similarly, the reference current of the NPN current mirror is  $I_3$  and the output current is  $I_5$ , leading to:

$$(3.12) \quad I_{el,n} = I_4 + I_5 = I_2 + I_3,$$

where  $n$  is the number of the channel or electrode.

This first version of the VI converter was tested with a square pulse input signal of  $\pm 6$  V using a 10 k $\Omega$  10 Watt load, which gave the expected output of  $\pm 60$  V, i.e.  $\pm 6$  mA. However, this output could only be held for a couple of minutes before some of the transistors of the current mirrors overheated, causing its currents to increase and burn some of the components. Thus, an upgraded design was needed using transistors with a higher power dissipation and different current mirrors to prevent them from overheating.

For the second version of the VI converter the two basic current mirrors are replaced by Wilson current mirrors. This new configuration uses three transistors per mirror that produce a much higher output resistance and minimise the input-output current difference (Figure 3.17). The feedback given by the transistors in this configuration allows a better control over the output current, which seemed an appropriate solution to avoid the increment of the output current that the first VI converter presented.

Figure 3.17 illustrates the NPN Wilson current mirror configuration, where the CTR  $\lambda$  is defined as:

$$(3.13) \quad \lambda_2 = 1 \pm 2 \left( \frac{\Delta\beta}{\bar{\beta}^2} \pm \frac{V_{OS}}{V_T} - \frac{V_{\Delta Q}}{(V_I)_{0.7}} \right),$$

where  $\bar{\beta}$  represents the mean of all transistor current gains,  $\Delta\beta$  the span of  $\beta$  values for all transistors and  $(V_I)_{0.7}$  is the Early intercept voltage evaluated at a  $V_{CB}$  operating point of 0.7 V approximately (difference between the collector voltages of  $Q_1$  and  $Q_2$  in this configuration) [97].

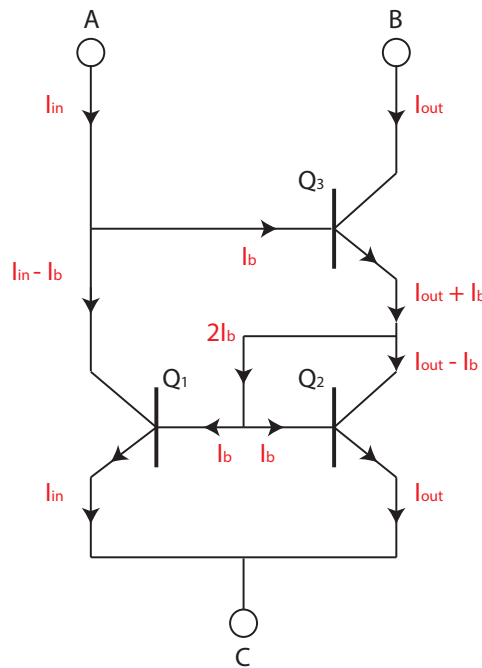


Figure 3.17: Three-transistor Wilson NPN current mirror configuration. Modified from [97].

This second version provides a more stable current output when testing the VI converter with the same driving signal and load as the previous version ( $\pm 6$  V and a 10 k $\Omega$  10 Watt load). Nevertheless, after running the system continuously for more than 20 minutes, some of the new transistors (with higher power dissipation than those used in the previous design) overheated (in both the voltage-controlled current source and current mirrors), resulting in the increment of the output current of the VI converter. Consequently, a third version was designed to address this problem.

The third version of the VI converter uses two improved Wilson current mirrors, adding a fourth transistor to each current mirror (Figure 3.18). This configuration equalises input and output collector voltages of the transistors, decreasing unbalancing influences. The exemplary NPN improved Wilson current mirror configuration is shown in Figure 3.18, where the CTR  $\lambda$  is given by:

$$(3.14) \quad \lambda_3 = 1 \pm 2 \left( \frac{\Delta\beta}{\beta^2} \pm \frac{V_{OS}}{V_T} \right).$$

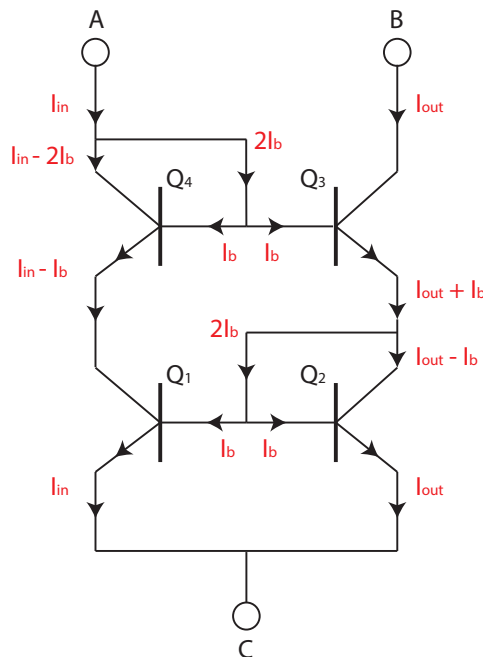


Figure 3.18: Four-transistor Wilson NPN current mirror configuration. Modified from [97].

Equation 3.14 shows that the remaining error between the output and input current is the result of a finite  $\beta$  and  $V_{BE}$  differences, thus reducing unbalances when compared to equations 3.11 and 3.13 [97]. This design also includes transistors in parallel for the voltage-controlled current source and ballast resistors (marked in green on Figure 3.19) to avoid thermal runaway, caused by an increase in the temperature of the transistors. The transistors in parallel increase current handling, and their operation is more reliable when using resistors in series with their emitters, balancing the current and temperature on the transistors. All the used resistor values are listed on Table 3.2. The electrical circuits were implemented in four boards, having two copies per board, as illustrated in Figure 3.20 (see schematic in the Appendix).

This final version proved to give the required constant output for more than 60 minutes, when testing with the same driving signal and load as the two previous versions. Even though the monitored output and overall circuit operated correctly and the chances of burning the

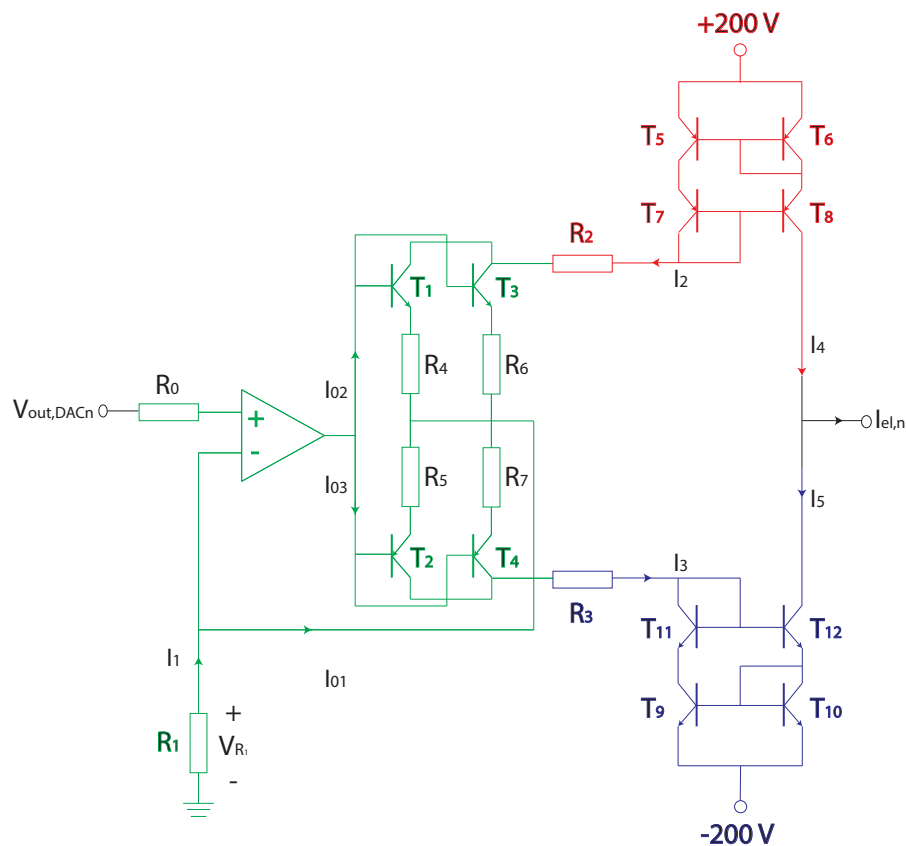


Figure 3.19: Final version of the VI converter electrical circuit, comprising a voltage-controlled current source with transistors in parallel and ballast resistors (in green) and two modified Wilson current mirrors (in red and blue).

Table 3.2: Resistor values used in the VI circuit.

Resistor	Value / $\Omega$
$R_0$	10000
$R_1$	1000
$R_2$	1000
$R_3$	1000
$R_4$	100
$R_5$	100
$R_6$	100
$R_7$	100

components (derived from overheated transistors) decreased, it was observed through a thermal camera that some of the transistors faced an overheating risk when the hardware was used for more than one hour. In order to address this risk and prevent any temperature changes that could result in a current change and burning of either transistors or the user's skin when touching the electrode, three fans were added on top of the VI circuits to cool all the components down and

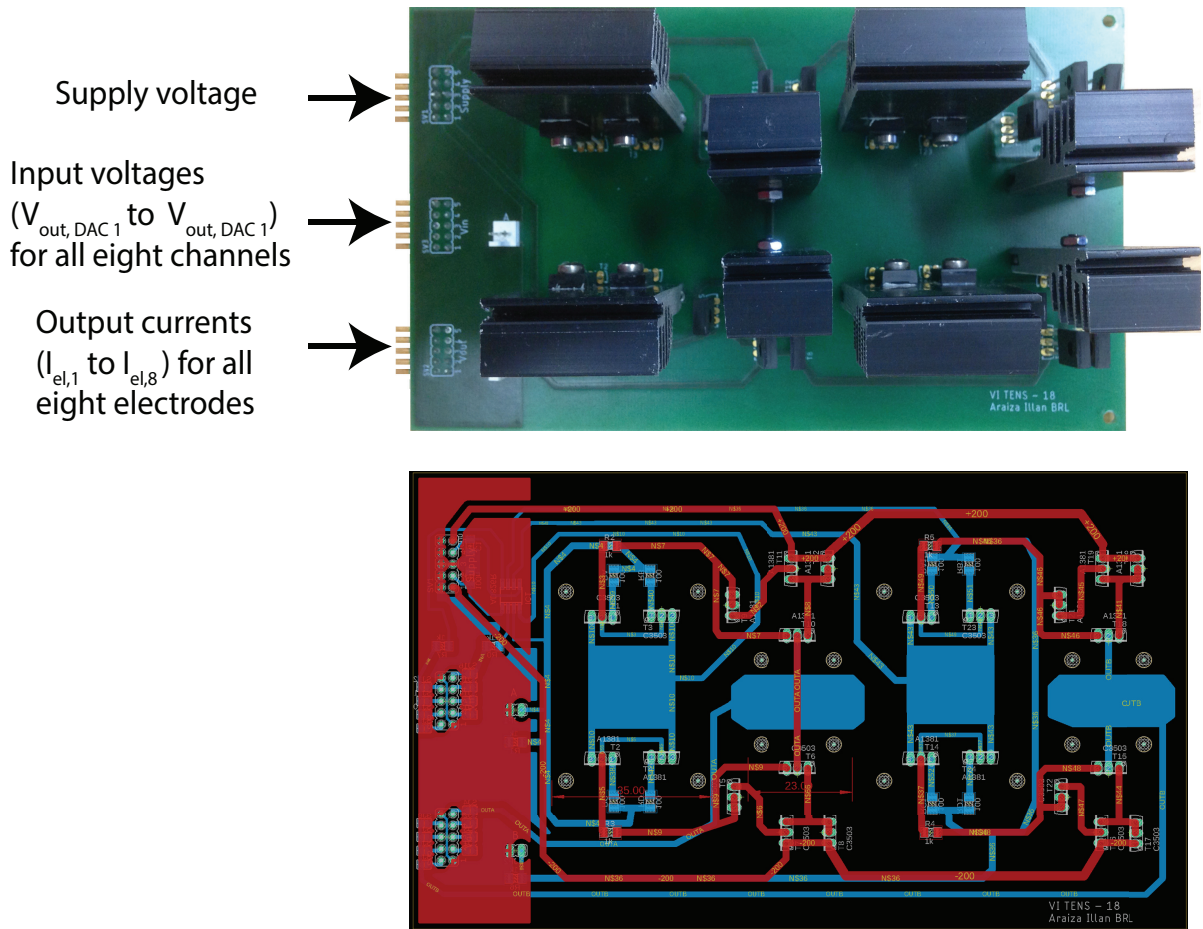


Figure 3.20: Circuit board comprising two VI units. The implemented board is shown at the top and the circuit board drawing at the bottom.

secure a safe and constant output current, and all transistors were mounted on heat sinks.

Figure 3.21 depicts the final version of the assembled hardware, where the modular architecture of the system is shown. The four VI boards are vertically positioned, having their outputs connected to the eight lines on the electrode array. The architecture of the boards was designed to enable easy measuring of voltage at specific points of the circuit, as well as when changing components if they resulted damaged. It was also designed to be compact, trying to optimise the space to fit two VI channels per board and counterbalance the bulk of the transistors, in order to make the system portable.

### 3.2.3 Board Design of the Power Supply

The power supply board for the VI converter (illustrated in Figures 3.21 and 3.22) accommodates the voltages needed to drive the operational amplifiers, the  $\pm 200$  V connected to the current mirrors and the buses for all inputs ( $V_{out,DACn}$ ) and outputs ( $I_{el,n}$ ) of the VI units. The design of

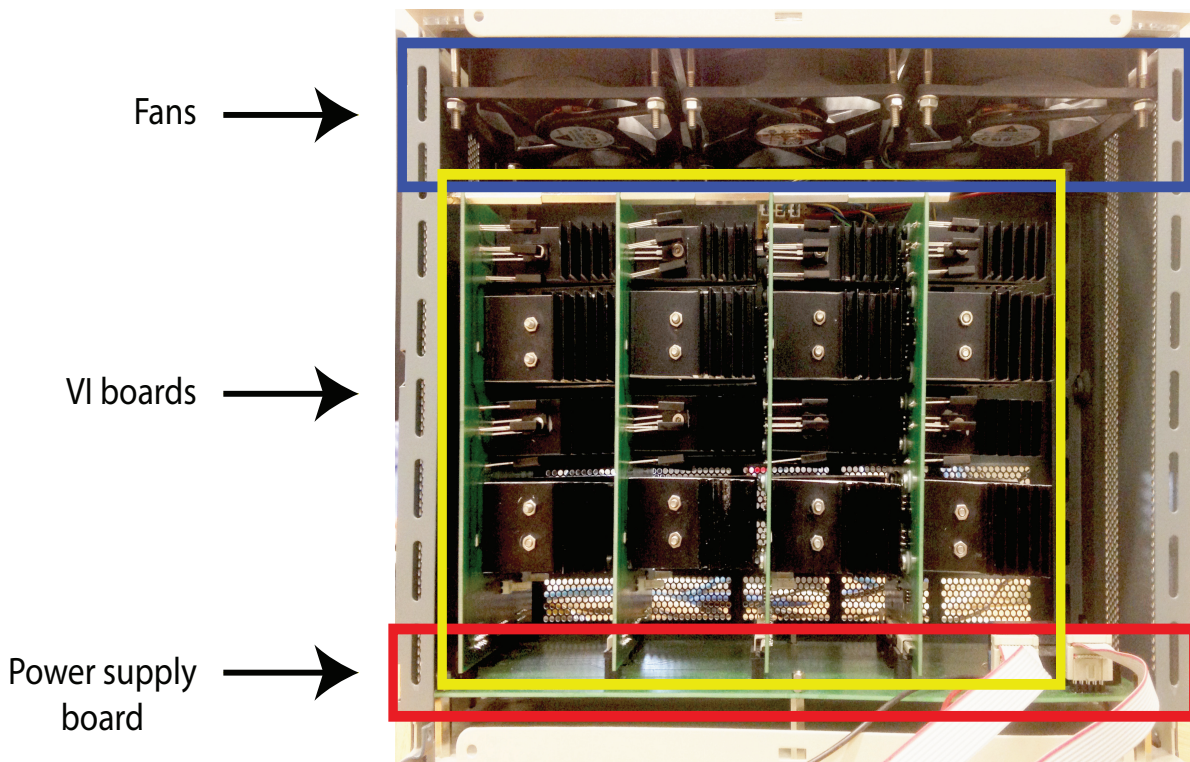


Figure 3.21: Assembled hardware for the VI converter. It includes the power supply board (marked in red), the four VI boards (marked in yellow) and the three fans (marked in blue).

this board facilitates the access to the four VI boards (using pin header connectors, as illustrated in Figure 3.23) and the air flow to cool down the components (see schematic in the Appendix).

### 3.2.4 Electrode Design

The physical electrode array has the same shape that was previously modelled for the simulated environment in chapter 2. It consists of eight linear electrodes of 10 mm by 1 mm, with 1 mm in between each line (Figure 3.24, see schematic in the Appendix). The electrodes are gold plated, allowing them to last longer and delaying their corrosion when in contact with human sweat during the experiments. Each of the linear electrodes is driven by one VI circuit, and the connector on the array allows the design to also be modular, facilitating the exchange of arrays when they start to show electrode wear.



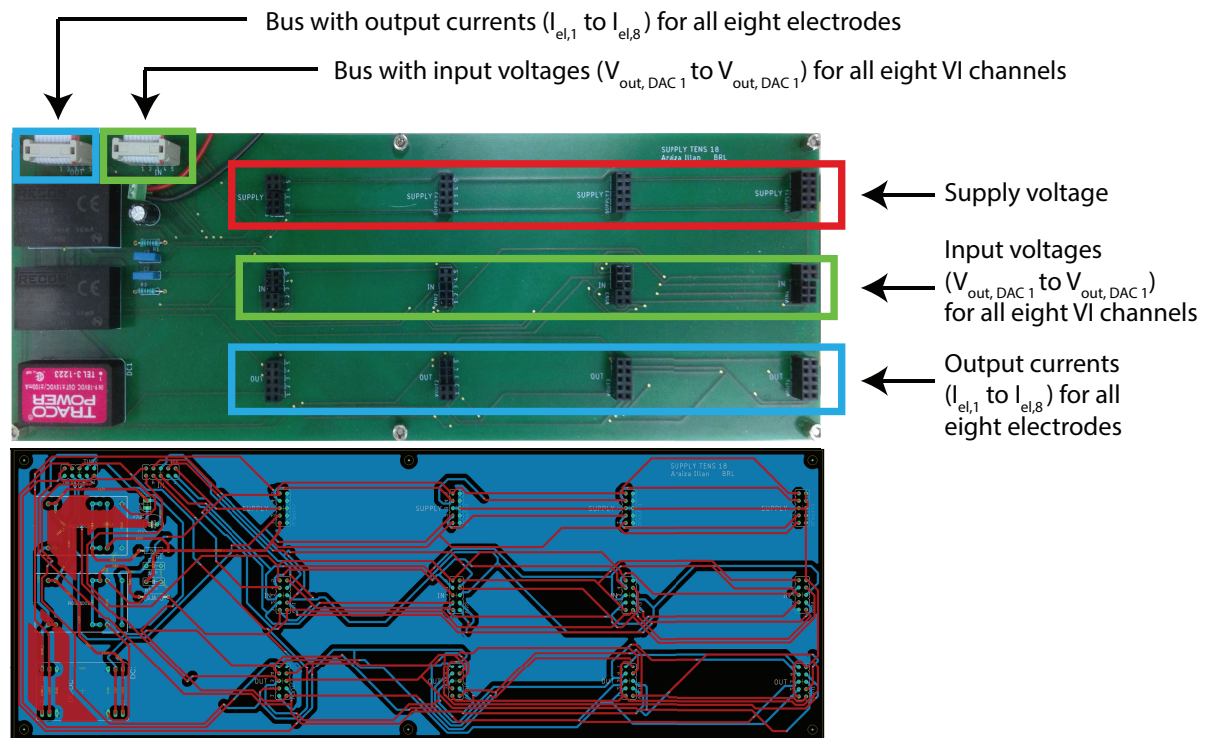


Figure 3.22: Power supply board for the VI converter. The implemented board is shown at the top and the circuit board drawing at the bottom.

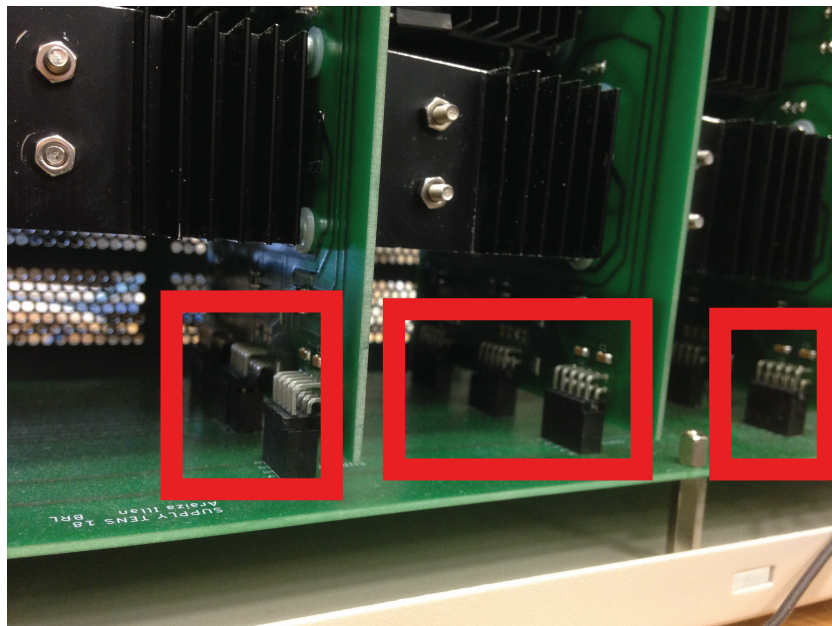


Figure 3.23: VI boards connected to the power supply board via pin header connectors (marked in red).

### 3.2. DESIGN AND IMPLEMENTATION OF THE HARDWARE FOR THE MODELLED TENS SYSTEM

---

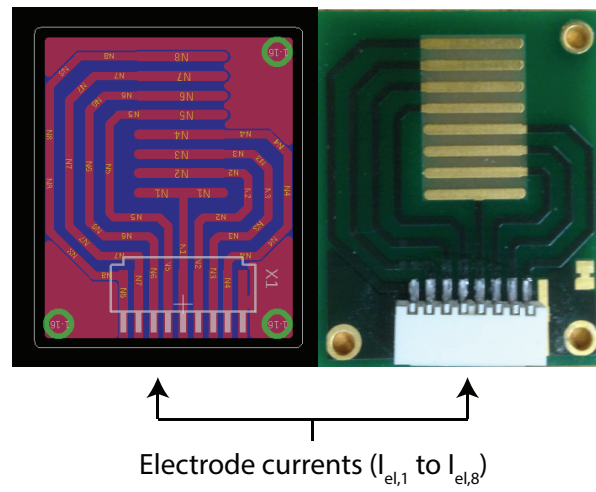


Figure 3.24: Electrode array. The circuit board drawing is shown on the left and the final electrode is on the right.



## PSYCHOPHYSICAL EXPERIMENTS USING THE TENS SYSTEM

In chapter 2 it was shown, through an ES model, that two sets of stimuli target nerve fibres connected to different mechanoreceptors, the next step to research was to investigate the sensations produced by these stimuli using the hardware implementation of the modelled TENS system developed in chapter 3. A series of psychophysical experiments was undertaken, employing a non-invasive technique to study how the participants perceive the given stimuli. This chapter includes a general introduction to psychophysics and signal detection theory, used to evaluate each participant's sensory capacities, followed by the design of the psychophysical experiments and the presentation and discussion of the obtained results.

### 4.1 Psychophysics

Psychophysics is a formal tool used to specify sensory capacities and test hypotheses about the underlying biological mechanisms related to sensory capacity. In psychophysics, the relationship between the value of the stimulus and the sensory response serves to define three laws: psychophysical laws, psychological laws and sensory response laws. The psychophysical laws refer to the way sensations relate to environmental stimuli, psychological laws describe how sensations relate to one another and sensory laws specify the way sensations relate to sensory responses [23]. Figure 4.1 illustrates the relationships between all three laws, where it can be observed that psychophysical laws can be deduced from experimental results if the sensory response laws of the participant are known.

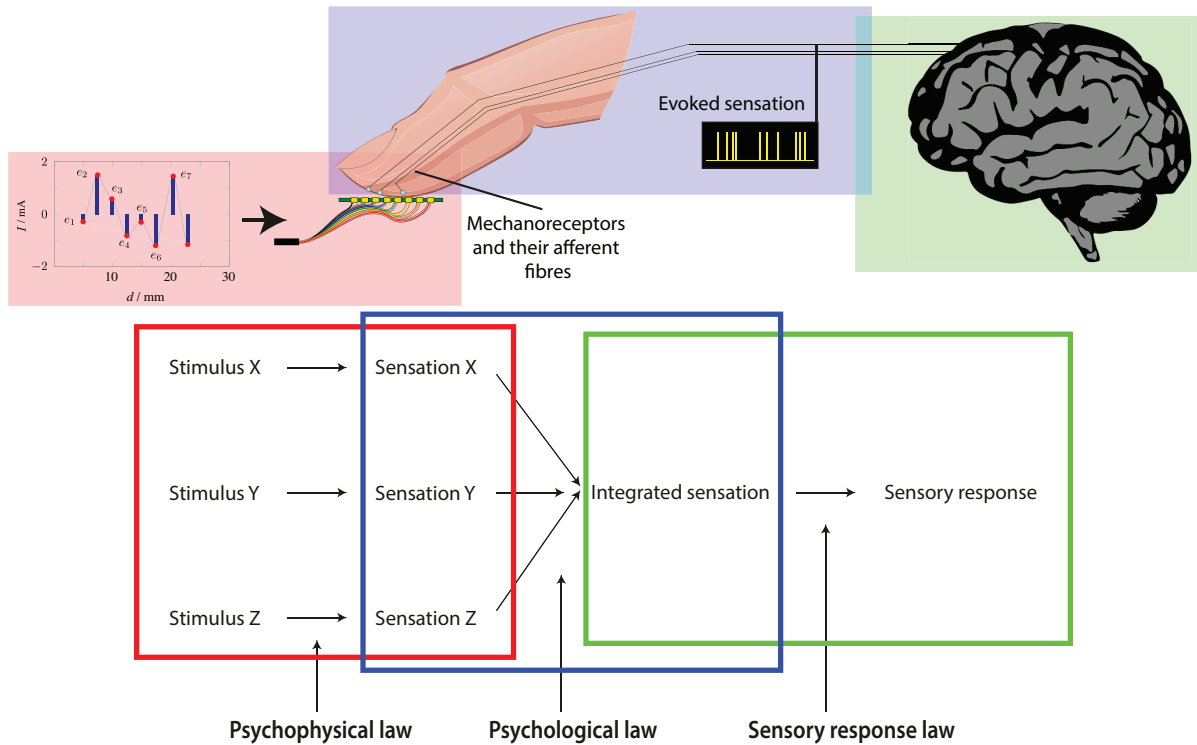


Figure 4.1: Relationships between psychophysical laws, psychological laws and sensory response laws. Modified from [23].

## 4.2 Signal Detection Theory

The theory of signal detection is a model that describes how people behave in detection situations. Taking into account that signals (stimuli) are detected against a background of activity (noise) that can be produced by the detection device or externally, the detection involves a participant making an observation ( $x$ ) and making a decision about that observation. The sensory observations can be represented by two probability distributions describing the random variation of noise and the signal-plus-noise [23]. Figure 4.2 depicts three theoretical frequency distributions of noise and signal plus noise for different cases of signal strength, where it can be seen that the difference between the means of the noise and signal-plus-noise decrease as the strength of the signal decreases. The overlap of the two distributions represent the difficulty of the decision. Since on every trial  $x$  is a random sample from one of the two distributions, the participant has to decide if  $x$  belongs to a signal added to the noise background or if it is only the noise by itself. The probability density or likelihood of  $x$  taking place when only noise is presented is given by the ordinate of the noise distribution. Likewise, the likelihood of  $x$  taking place when a signal is presented is given by the ordinate of the signal-plus-noise distribution [23]. There is a particular likelihood ratio  $l(x)$  for each value of  $x$ , defined by:

$$(4.1) \quad l(x) = \frac{\text{ordinate of signal-plus-noise distribution}}{\text{ordinate of noise distribution}}.$$

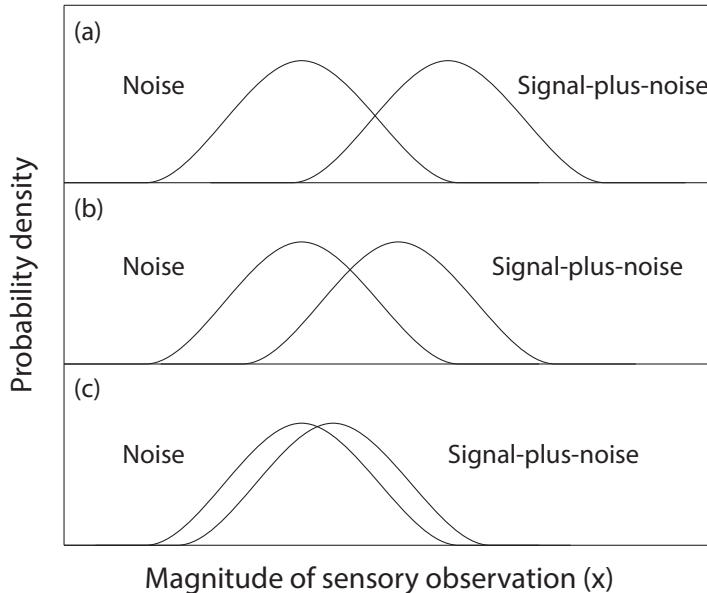


Figure 4.2: Noise and signal-plus-noise theoretical frequency distributions for three different values of signal strength. Panel (a) shows the strongest signal strength, while panel (c) shows the weakest signal strength. Modified from [23].

In signal detection theory, the assumption that a participant has a particular value of  $l(x)$  as a cutoff point is made. This cutoff point is defined as a criterion, and it serves as reference for the participant to make a decision regarding a particular observation  $x$ . If  $l(x)$  is equal or greater than the criterion, signal-plus-noise will be chosen; whereas if  $l(x)$  is less than the criterion, noise will be chosen. If the participant correctly classifies the stimulus above the criterion, a "hit" will be scored (correctly detecting the signal). Otherwise, incorrectly allocating it above the criterion will result in a "false alarm" (incorrectly affirming that the signal is present when it is not, commonly known as "false positive"). Equivalently, if the participant correctly classifies the stimulus below the criterion, a "correct-rejection" is achieved (correctly detecting that the signal is not present); whilst an incorrect allocation below the criterion leads to a "miss" (failing to detect the signal, commonly known as "false negative").

The theory also introduces a measure of discriminability ( $d'$ ), defined in terms of  $z$  (inverse of the normal distribution function).  $d'$  is a measure of sensitivity (ability to discriminate between stimuli [62]) that is independent of the method used to calculate it [48]. The  $z$  transformation translates the hit and false-alarm rate ( $H$  and  $F$ , respectively) to a  $z$  score (standard deviation units) [62]. If the participant is not able to discriminate at all,  $H = F$  and  $d' = 0$ ; similarly, perfect accuracy leads to an infinite  $d'$ .

### 4.3 Materials and Methods - Psychophysical Experiments

A psychophysical experiment serves the purpose of answering how certain experimental conditions alter the performance of a participant [67]. This experiment regards a set of trials where a stimulus is presented and a response is collected (i.e. a decision of the participant regarding an observation). The elements conforming a psychophysical experiments are: a stimulus, task, method, analysis and measure [48]. Psychophysical measurement refers to the behaviour that reveals internal processes [67]. In this case, the current provided through the TENS system described in chapter 3 is the stimulus; the task is to discriminate between the given stimuli (modelled in chapter 2) using the method of paired comparison (i.e., identifying different tactile sensations). The analysis refers to how the collected data is converted into measurements; i.e. obtaining the probability density functions, and the measures involved are the tactile sensitivity and criterion of the participant. Four stimuli and five participants were selected for the psychophysical experiments. All participants were adults with a healthy motor physiology of both arms and hands, and no pre-existing psychological conditions that may affect the memory (e.g. dementia or Alzheimer's) nor a pacemaker or an implantable cardioverter defibrillator. They all gave their consent to be part of the study after being told the specifications of the tests and the potential risks, using their index finger of their dominant hand for all tests. Both Research Ethics Committees from the University of Bristol and the University of the West of England gave ethical approval to carry out the psychophysical experiments (see Appendix).

One method of measuring tactile sensitivity is to determine the smallest amplitude of vibration that can be detected by the participant. Since vibrotactile thresholds depend on various factors (such as the location of the stimulation, the size of the stimulated skin area, and the duration and frequency of the stimulus [23]), the calibration of the system was needed to be able to provide a stimulus with a particular amplitude for a certain period of time that would guarantee a clear sensation for the participant.

#### 4.3.1 Current Calibration

The first calibration test was designed using four stimuli from the modelled sets in chapter 2, following the calibration method described in a study documenting dissimilarity ratings on the perception of frequency and intensity of electrical stimulation on a fingertip [38]. Two stimuli were randomly chosen from  $ES_s$  (set of 30 electrical stimuli targeting a shallower nerve) and two stimuli were randomly selected from  $ES_d$  (set of 25 electrical stimuli targeting a deeper nerve). All 8 electrode currents of each of the chosen four stimuli are given in table 4.1.

The calibration test used each of the four stimuli presented one at a time as a constant stimulus at 50 Hz. Starting with an amplitude not larger than  $\pm 0.05$  mA for each of the eight electrodes, the amplitudes are increased in very small steps (maximum  $\pm 0.05$  mA) by the participant (pressing a button that would send a signal to the Arduino Due boards to increase the

Table 4.1: **Electrode currents for the selected ES (all shown in mA).**

<b>Electrical stimulus</b>	$I_{el,1}$	$I_{el,2}$	$I_{el,3}$	$I_{el,4}$	$I_{el,5}$	$I_{el,6}$	$I_{el,7}$	$I_{el,8}$
<i>A</i>	-2.4	1.7	2.1	1.6	-0.3	-1.5	-0.6	-0.7
<i>B</i>	-1.6	1.3	0.4	1.9	-1.9	-0.8	-0.4	-2.7
<i>C</i>	-2.0	2.0	0.7	-0.6	-0.1	1.0	-2.0	0.9
<i>D</i>	-1.6	1.9	1.6	-0.9	-1.4	0.4	0.7	-0.7

DAC values in all eight channels) until they could perceive a sensation. After these values were logged, the participant kept increasing the amplitudes until the stimulus became uncomfortable. This method allows the setting of individual amplitude ranges where the participants could clearly feel each of the presented stimuli. Each test lasted 60 seconds and was run 10 times per participant for each stimulus.

This calibration method proved to be complicated for the participants, due to the triggering of nerve saturation, where some of the participants would report not being able to detect any sensation, then quickly find the stimulus uncomfortable when increasing the amplitude by only one step. It was also noted that the threshold and the amplitude range would significantly change if the calibration was run more than once during the same day; this finding also supported the hypothesis regarding nerve saturation, an effect that was further analysed to verify its duration. This effect was also taken into account as a potential limitation for further experiments using the ES system. Another limitation was that if the calibration was run on different days, the amplitude ranges of the stimuli would not be consistent (the amplitudes selected by the observers were significantly different every time a test was run). This was attributed to changes on the participants' skin mainly regarding hydration. The calibration test was run with 18 participants, where seven of them faced both limitations.

After these limitations were found using this calibration setup, revised method was adopted and tested with the 11 participants who did not present the previous limitations. The second calibration configuration was devised to overcome the problem of saturation. The new test presented all four mean amplitude values taken from the average of the participant's ranges per stimulus for one second at 50 Hz. The interstimulus interval was fixed to one second. If the participant was not able to clearly sense each stimulus, that specific amplitude was increased by a step not larger than  $\pm 0.05$  mA. This setup allows shorter periods of stimulation (8 seconds per test), decreasing the probability of saturating the participants' nerves. The selected amplitudes were logged to be used in the paired comparison experiments. The final five participants were chosen according to their availability to run further experiments.

Each participant used the same finger throughout all calibration tests. At the beginning of each test, the fingertip and the electrode array were cleaned with isopropyl alcohol. The participants were asked not to move their finger once it was placed on the electrode array, for it could generate an electric shock sensation [39].



### 4.3.2 Saturation

An exploratory saturation test was performed on one of the five participants only, for it was expected to require a long time to run. For practical purposes, fingers 2, 3, 4 and 5 from the non-dominant hand were used to run each of the four stimuli (*A*, *B*, *C* and *D*) at 10 Hz. Each stimulus had a specific amplitude that would produce a clear sensation on the corresponding fingertip, all perceived with similar intensity. The stimulation was constant for each trial, maintaining the same amplitude and stopping when the participant reported it uncomfortable, or when it reached two minutes. The aim of this test was to analyse the time range where the nerves could be electrically stimulated without reaching saturation in order to set the duration of the planned paired comparison tests accordingly.

Six tests were run on the same day per finger. Before each test, the fingertips and the electrode array were cleaned with isopropyl alcohol. The first test was run ensuring that all four fingers had not been exposed to any other electrical stimulation earlier that day. The timing for each test is listed on table 4.2. The first test is set to start at  $t_1 = 0$ . It can be observed that the second test was run 10 minutes after the first one, the third 30 minutes after the second, the 4th 60 minutes after the third, the fifth 120 minutes after the 4th and the sixth 240 minutes after the fifth. All stimuli were presented for a maximum of 120 seconds.

Table 4.2: **Timing of all six saturation tests.**

Test number $i$	Starting time $t_i$ / min
1	0
2	10
3	40
4	100
5	220
6	460

### 4.3.3 Same-Different Paired Comparison

Paired comparison is a performance-based procedure where the participant is required to make a decision regarding two stimuli per trial. Performance-based techniques measure the participant's ability at a certain task [48]. The task is to classify the stimuli, two or more, as identical or from the same class (thus responding "same" or "different"), even if the participant does not know how the stimuli differ. During the task, a pair of stimuli on each trial is presented, with half of the trials having a pair that is different and half of the trials having a pair that is the same.

This task was chosen in order to test the four selected examples from the two sets of current signals ( $ES_s$  corresponding to the electrical stimulation of a shallower fibre, and  $ES_d$  corresponding to the electrical stimulation of a deeper fibre) developed in chapter 2, studying the similarity or dissimilarity between the sensations produced by them. There are four possible

pairs:  $\langle ES_{s,i}ES_{s,i} \rangle$ ,  $\langle ES_{d,j}ES_{d,j} \rangle$ ,  $\langle ES_{s,i}ES_{d,j} \rangle$  and  $\langle ES_{d,j}ES_{s,i} \rangle$ , where  $i = [A, B]$  and  $j = [C, D]$ .

The calculation of  $d'$  is given by:

$$(4.2) \quad d'_{\text{same-different}} = 2z \left( \frac{1}{2} \left\{ 1 + \left[ 2p(c)_{\text{max}} - 1 \right]^{1/2} \right\} \right),$$

where  $p(c)_{\text{max}}$  is the proportion of correct responses for an unbiased participant [62], described by:

$$(4.3) \quad p(c)_{\text{max}} = \phi [z(H) - z(F)]/2,$$

where  $\phi$  is the normal distribution function.

The decision criteria can be expressed as a likelihood ratio ( $\beta$ ); the criterion location on the decision axis ( $c$ ) is given by:

$$(4.4) \quad c = \frac{\ln(\beta)}{d'}.$$

Similarly, the response bias ( $c_a$ ), describing the bias at each of the decision criteria points, is given by:

$$(4.5) \quad c_a = -\frac{\sigma_j}{\sigma_0 + \sigma_j} \sqrt{\frac{2}{\sigma_0^2 + \sigma_j^2}} [z(H) - z(F)],$$

where  $\sigma_j$  is the standard deviation of the  $m$  signal conditions represented by probability density functions ( $j$  goes from 0 to  $m - 1$ ) and  $\sigma_0$  is the units of the decision axis (usually equal to one) [28, 62].

As stated before, from the four stimuli, two belong to the  $ES_s$  set (stimulus  $A$  and  $B$ ) and the other two to the  $ES_d$  set (stimulus  $C$  and  $D$ ). This number of stimuli gives 24 pairs to be included in each test, 12 of which present different stimuli (number of possible permutations) and 12 the same stimulus (ensuring the probability of presenting different and same stimuli is the same; i.e., avoiding any bias to "same" or "different" classification). These pairs are listed on table 4.3. The experiments are divided into three blocks, each presenting the stimuli with a different frequency. Each round comprises 10 trials, where the order of presentation of the pairs of stimuli is randomly allocated. The chosen frequencies were 10, 50 and 200 Hz, considering that the sensitivity of Merkel disks for mechanical stimulation is highest around 10 Hz and that of Pacinian corpuscles around 200 – 300 Hz, and that both mechanoreceptors are activated around 50 Hz [12]. These frequencies were selected in order to investigate their effect when used in

Table 4.3: Set of 24 pairs used for the same-different paired comparison.

Pair	First stimulus	Second stimulus
1	<i>A</i>	<i>A</i>
2	<i>A</i>	<i>A</i>
3	<i>A</i>	<i>A</i>
4	<i>A</i>	<i>B</i>
5	<i>A</i>	<i>C</i>
6	<i>A</i>	<i>D</i>
7	<i>B</i>	<i>A</i>
8	<i>B</i>	<i>B</i>
9	<i>B</i>	<i>B</i>
10	<i>B</i>	<i>B</i>
11	<i>B</i>	<i>C</i>
12	<i>B</i>	<i>D</i>
13	<i>C</i>	<i>A</i>
14	<i>C</i>	<i>B</i>
15	<i>C</i>	<i>C</i>
16	<i>C</i>	<i>C</i>
17	<i>C</i>	<i>C</i>
18	<i>C</i>	<i>D</i>
19	<i>D</i>	<i>A</i>
20	<i>D</i>	<i>B</i>
21	<i>D</i>	<i>C</i>
22	<i>D</i>	<i>D</i>
23	<i>D</i>	<i>D</i>
24	<i>D</i>	<i>D</i>

electrical stimulation, since the only documentation regards mechanical stimulation. All stimuli had a 50% duty cycle.

Each stimulus was presented for one second, the interstimulus interval was fixed to one second and the interval between pairs was set to three seconds, therefore giving a total of 144 seconds per trial. This period of time ensures that the participants' nerve fibres would not reach saturation; i.e., the participants could comfortably feel all of the pairs per test.

## 4.4 Results

The paired comparison data is presented firstly evaluating the discrimination between all stimuli for each of the three used frequencies, then evaluating the discrimination between classes of stimuli ( $ES_s$  and  $ES_d$ ) for each frequency and finally, evaluating the discrimination of stimuli within the aforementioned classes (i.e., between both stimuli from  $ES_s$  and between both stimuli of  $ES_d$ ) for each frequency. All corresponding plots and the estimated discrimination measures were computed using RscorePlus (<http://psych.colorado.edu/~lharvey/html/software.html>).

#### 4.4.1 Saturation Test

The time ranges before reaching nerve saturation for all fingertips (fingers 2 - 5) for each of the four stimuli are illustrated in panels (a) to (d) in Figure 4.3. Panels (a) and (c) in Figure 4.3 show that none of the fingers could match the first measured time range before reaching saturation in the rest of the trials. Two fingers did reach the first measured time range before saturation in panel (b) in Figure 4.3, and panel (d) depicts an increment in the first measured time range before saturation at the last trial (finger 2).

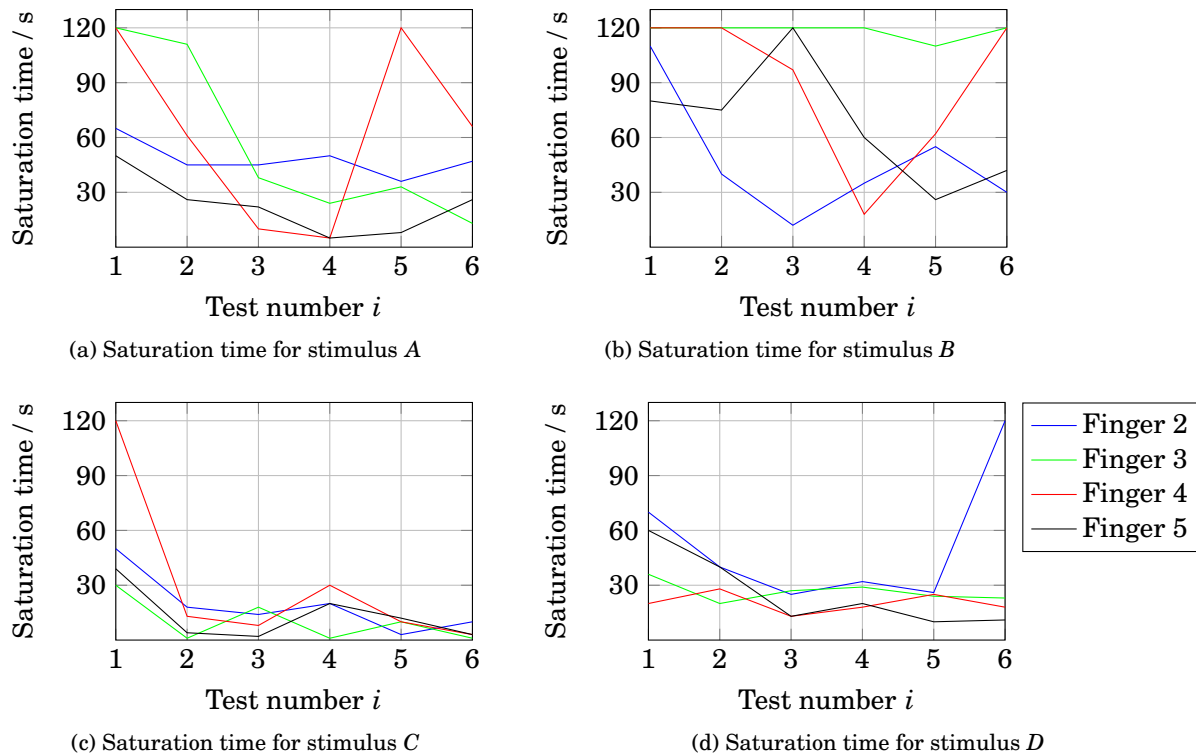


Figure 4.3: Time ranges before reaching nerve saturation for all four fingers when four stimuli were presented at 10 Hz during the six saturation tests (table 4.2). Panel (a) shows the response of the fingers to stimulus A, panel (b) to stimulus B, panel (c) to stimulus C and panel (d) to stimulus D.

#### 4.4.2 Discrimination Between all Presented Stimuli

For this section, table 4.4 shows the stimulus pairs taken as "same", and table 4.5 the stimulus pairs defined as "different". The estimated  $d'$ ,  $\beta$  and  $c$  for each participant ( $P_n$ ) for all three frequencies (10, 50 and 200 Hz) are shown in table 4.6.

The performances of the five participants on the discrimination between all stimuli are depicted in Figure 4.4, where each row corresponds to the probability density distributions of each participant using all four stimuli with 10, 50 and 200 Hz, respectively. The red markers

Table 4.4: "Same" pairs for discrimination between all stimuli.

First stimulus	Second stimulus
A	A
B	B
C	C
D	D

Table 4.5: "Different" pairs for discrimination between all stimuli.

First stimulus	Second stimulus
A	B
A	C
A	D
B	A
B	C
B	D
C	A
C	B
C	D
D	A
D	B
D	C

Table 4.6: Signal detection model parameters from discriminating between all stimuli.

Participant	$d'_{10Hz}$	$\beta_{10Hz}$	$c_{10Hz}$	$d'_{50Hz}$	$\beta_{50Hz}$	$c_{50Hz}$	$d'_{200Hz}$	$\beta_{200Hz}$	$c_{200Hz}$
$P_1$	3.70	2.82	0.28	2.03	1.90	0.32	1.09	1.25	0.11
$P_2$	2.57	1.13	0.05	1.96	1.65	0.25	-0.06	1.00	0.01
$P_3$	2.61	1.67	0.20	1.93	2.03	0.37	0.02	1.00	0.07
$P_4$	2.37	1.42	0.15	2.09	2.99	0.52	-0.42	1.00	0.04
$P_5$	2.53	0.75	-0.12	1.76	1.50	0.23	0.82	0.89	-0.14
Average	2.76	1.56	0.11	1.95	2.01	0.34	0.29	1.03	-0.02

represent the computed decision criterion ( $c_a$ ) and its standard error in each panel. According to the results listed on table 4.6 and panels (a), (b) and (c) in Figure 4.4, it can be observed that participant  $P_1$  presented the best performance in 10 and 200 Hz and the second best when using 50 Hz. Participants  $P_2$ ,  $P_3$  and  $P_4$  were not able to discriminate between all four stimuli when using 200 Hz.  $P_4$  had the best performance at 50 Hz. Overall, the participants show what is defined as a conservative decision (more evidence of the signal is needed in order to decide whether it was presented on the pair of stimuli or not) at 10 and 50 Hz. It is also noted that the value of  $d'$  of each participant drops as the frequency is increased.

The breakdown of the responses of the participants who obtained the best performances for each of the three frequencies ( $P_1$  for 10 and 200 Hz and  $P_4$  for 50 Hz) when discriminating

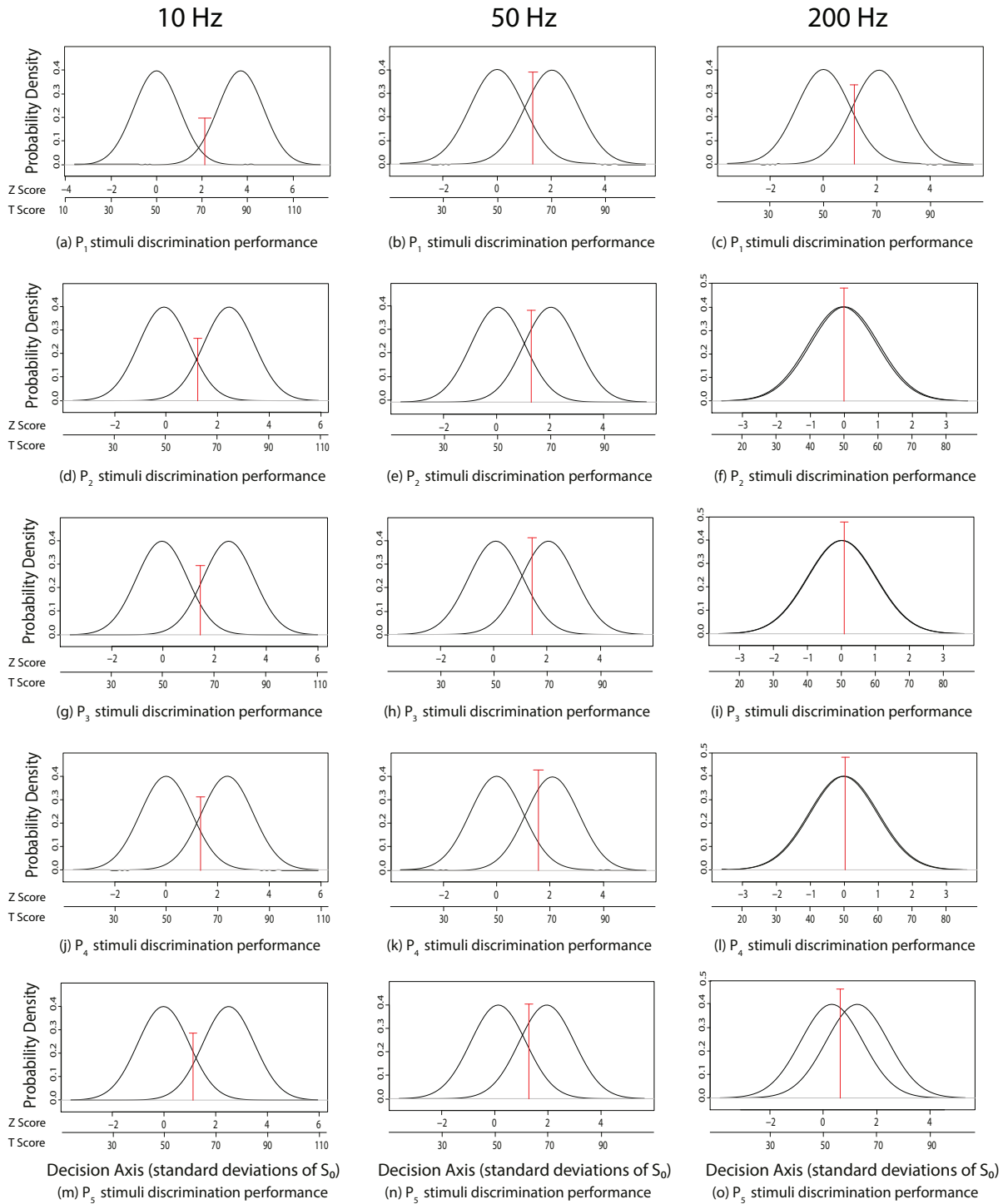


Figure 4.4: Probability density distributions of the discrimination performances between all four stimuli of the five participants ( $P_1$  to  $P_5$ ). Panels (a), (b) and (c) correspond to the responses of  $P_1$ , panels (d), (e) and (f) to  $P_2$ , panels (g), (h) and (i) to  $P_3$ , panels (j), (k) and (l) to  $P_4$ , and panels (m), (n) and (o) to  $P_5$ . Each column refer to the stimuli at 10, 50 and 200 Hz. All computed decision criteria ( $c_a$ ) and their standard errors are marked in red in each panel. The corresponding T score values to the Z score values are shown in each panel.

between all stimuli are shown in Figure 4.5. Here it can be observed that a large amount of hits and correct rejections lead to a high performance, as well as a small amount of misses and false alarms.

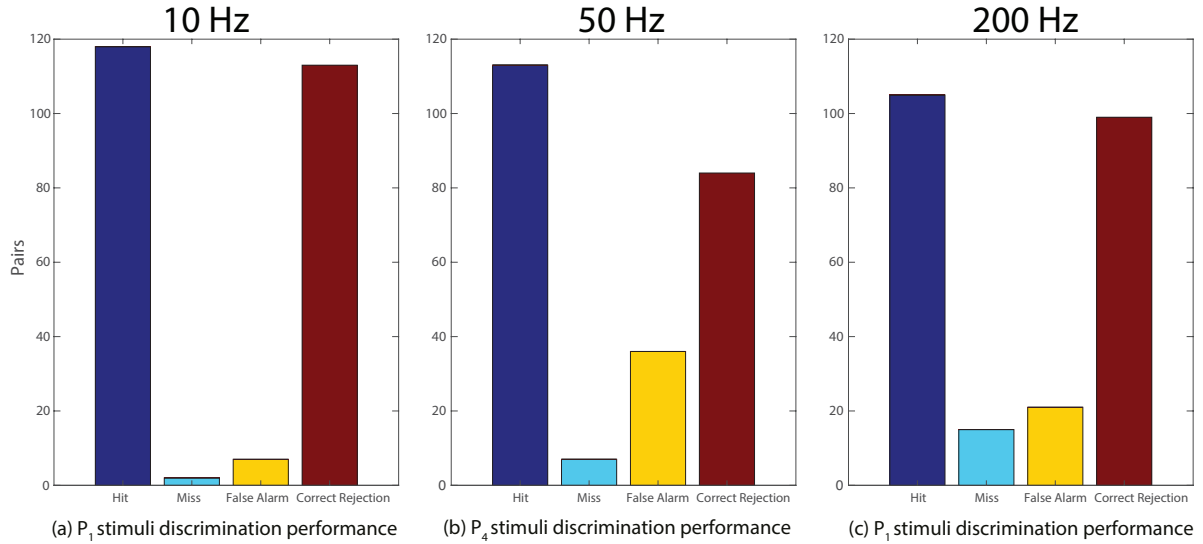


Figure 4.5: Number of hits, misses, false alarms and correct rejections of the best performances of the five participants when discriminating between all stimuli. Panels (a) and (c) correspond to the performance of  $P_1$  for 10 and 200 Hz, respectively. Panel (b) illustrates the performance of  $P_4$  for 50 Hz.

The added performance of all five participants is observed in Figure 4.6, where each panel corresponds to the added responses for 10, 50 and 200 Hz when discriminating between all stimuli. It is evident that the best added performance was achieved when using 10 Hz, and the worst performance when using 200 Hz.

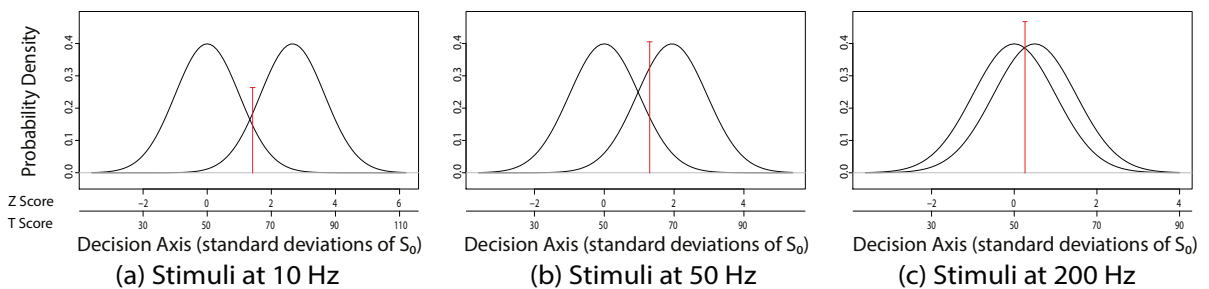


Figure 4.6: Probability density distributions of the added discrimination performances between all stimuli of the five participants ( $P_1$  to  $P_5$ ). Panels (a), (b) and (c) correspond to the added responses at 10, 50 and 200 Hz, respectively. All computed decision criterions ( $c_a$ ) and their standard errors are marked in red in each panel. The corresponding T score values to the Z score values are shown in each panel.

### 4.4.3 Discrimination Between Stimuli Classes

The "different" pairs between classes  $ES_s$  and  $ES_d$  are listed on table 4.7, where it is observed that all the pairs correspond to stimuli from different classes (thus excluding pairs with stimuli from the same class). The estimated  $d'$ ,  $\beta$  and  $c$  for all five participants using all three frequencies (10, 50 and 200 Hz) for the stimuli, are shown in table 4.8.

Table 4.7: "Different" pairs for discrimination between stimuli classes.

First stimulus	Second stimulus
<i>A</i>	<i>C</i>
<i>A</i>	<i>D</i>
<i>B</i>	<i>C</i>
<i>B</i>	<i>D</i>
<i>C</i>	<i>A</i>
<i>C</i>	<i>B</i>
<i>D</i>	<i>A</i>
<i>D</i>	<i>B</i>

Table 4.8: Signal detection model parameters from discriminating between stimuli classes.

Participant	$d'_{10Hz}$	$\beta_{10Hz}$	$c_{10Hz}$	$d'_{50Hz}$	$\beta_{50Hz}$	$c_{50Hz}$	$d'_{200Hz}$	$\beta_{200Hz}$	$c_{200Hz}$
$P_1$	3.77	2.49	0.24	2.61	1.07	0.03	2.08	1.25	0.11
$P_2$	3.11	0.50	-0.23	3.20	0.31	-0.36	-0.06	1.00	0.01
$P_3$	4.00	0.14	-0.50	1.93	2.03	0.37	-0.20	0.96	0.18
$P_4$	3.83	0.11	-0.59	3.01	1.22	0.07	-0.073	1.00	0.06
$P_5$	2.80	0.50	-0.25	2.26	0.96	-0.02	0.84	0.89	-0.14
Average	3.50	0.75	-0.27	2.60	1.12	0.02	0.52	1.02	0.04

The performances of all five participants ( $P_1$  to  $P_5$ ) are shown in Figure 4.7, where the each row corresponds to the responses of each participant regarding the discrimination between stimuli classes at 10, 50 and 200 Hz, respectively. Each panel includes the individual decision criterion ( $c_a$ ) alongside its standard error marked in red. Panel (h) in Figure 4.7 illustrates that participant  $P_3$  had the best performance when using stimuli at 10 Hz. Similarly, panels (b) and (c) show that participant  $P_1$  had the best performance at 50 and 200 Hz, respectively. Participants  $P_2$ ,  $P_3$  and  $P_4$  were not able to distinguish between stimuli classes at 200 Hz. Participant  $P_2$  showed their individual best performance at 50 Hz, contrary to the rest of the participants that had their individual bests at 10 Hz. Participant  $P_1$  proved to be conservative while making a decision, whilst participant  $P_5$  was the only one exhibiting what is known as a liberal behaviour (i.e., when little evidence of the signal is needed in order to make a decision regarding whether the signal was presented or not) when using stimuli at 10 and 200 Hz. Overall, it can be observed in table 4.8 that the best performance regarding the task of differentiating between stimuli



classes, was achieved when using 10 Hz.

The breakdown of the responses of the participants who obtained the best performances for each of the three frequencies ( $P_3$  for 10 Hz,  $P_2$  for 50 Hz and  $P_1$  for 200 Hz) when discriminating between stimuli classes are shown in Figure 4.8. It is illustrated that a large amount of hits and correct rejections lead to a high performance, as well as a small amount of misses and false alarms.

The added performance of the five participants is presented in Figure 4.9, where the panels correspond to the added responses for 10, 50 and 200 Hz when discriminating between stimuli classes. It is evident that the best added performance was achieved when using 10 Hz, and the worst performance when using 200 Hz.

#### 4.4.4 Discrimination Within Stimuli Classes

The four "different" pairs for the discrimination within classes  $ES_s$  and  $ES_d$  are shown in table 4.9, where it is noted that the pairs correspond to stimuli from the same class (thus excluding pairs with stimuli from different classes).  $d'$ ,  $\beta$  and  $c$  of all participants for all three presented frequencies are listed on table 4.10.

Table 4.9: "Different" pairs for discrimination within stimuli classes.

First stimulus	Second stimulus
A	B
B	A
C	D
D	C

Table 4.10: Signal detection model parameters from discriminating within stimuli classes.

Participant	$d'_{10Hz}$	$\beta_{10Hz}$	$c_{10Hz}$	$d'_{50Hz}$	$\beta_{50Hz}$	$c_{50Hz}$	$d'_{200Hz}$	$\beta_{200Hz}$	$c_{200Hz}$
$P_1$	3.57	3.42	0.35	1.27	2.42	0.70	2.09	1.25	0.11
$P_2$	2.01	1.93	0.33	0.85	1.99	0.81	0.04	1.00	-0.04
$P_3$	1.75	2.99	0.63	1.08	2.35	0.79	0.47	0.93	-0.15
$P_4$	1.46	2.41	0.60	0.90	2.73	1.12	0.02	1.00	0.01
$P_5$	2.19	1.13	0.06	1.17	1.85	0.52	0.80	0.91	-0.13
Average	2.20	2.38	0.39	1.05	2.27	0.79	0.68	1.02	-0.04

The probability density distributions describing the performances of the five participants ( $P_1$  to  $P_5$ ) are shown in Figure 4.10. All the three panels per row correspond to the performance of each participant when using stimuli at 10, 50 and 200 Hz, respectively. The individual decision criterions ( $c_d$ ) and their standard error are marked in red in each panel. Panels (a), (b) and (c) in Figure 4.10 show that participant  $P_1$  had the best performance regarding the discrimination within stimuli classes at 10, 50 and 200 Hz. The same participant ( $P_1$ ) was the only one that

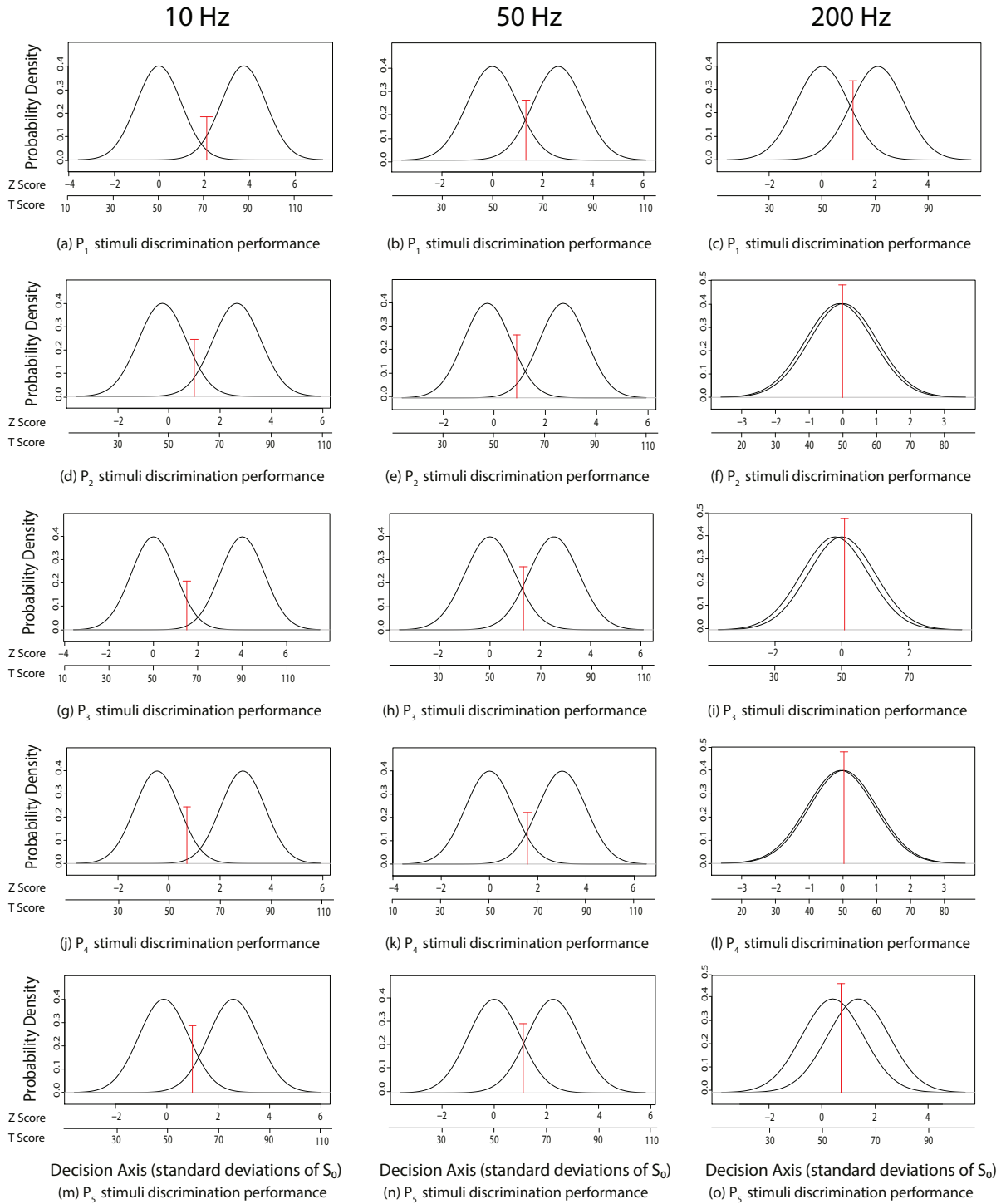


Figure 4.7: Probability density distributions of the discrimination performances between stimuli classes of the five participants ( $P_1$  to  $P_5$ ). Panels (a), (b) and (c) correspond to the responses of  $P_1$ , panels (d), (e) and (f) to  $P_2$ , panels (g), (h) and (i) to  $P_3$ , panels (j), (k) and (l) to  $P_4$ , and panels (m), (n) and (o) to  $P_5$ . Each column refer to the stimuli at 10, 50 and 200 Hz. All computed decision criteria ( $c_a$ ) and their standard errors are marked in red in each panel. The corresponding T score values to the Z score values are shown in each panel.

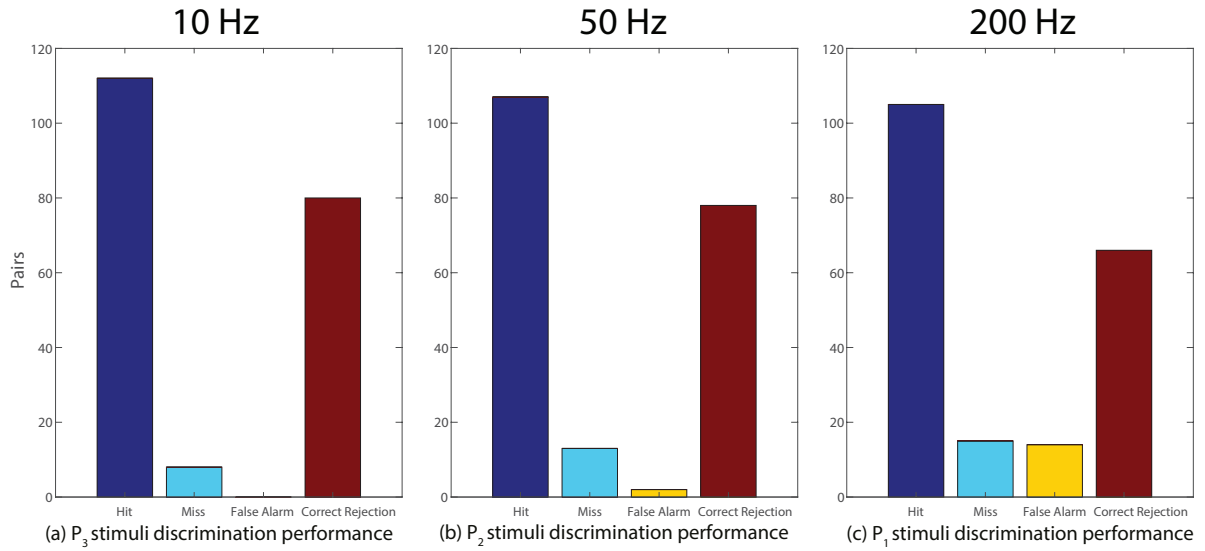


Figure 4.8: Number of hits, misses, false alarms and correct rejections of the best performances of the five participants when discriminating between stimuli classes. Panel (a) shows the performance of  $P_3$  for 10 Hz, panel (b) of  $P_2$  for 50 Hz and panel (c) of  $P_1$  for 200 Hz.

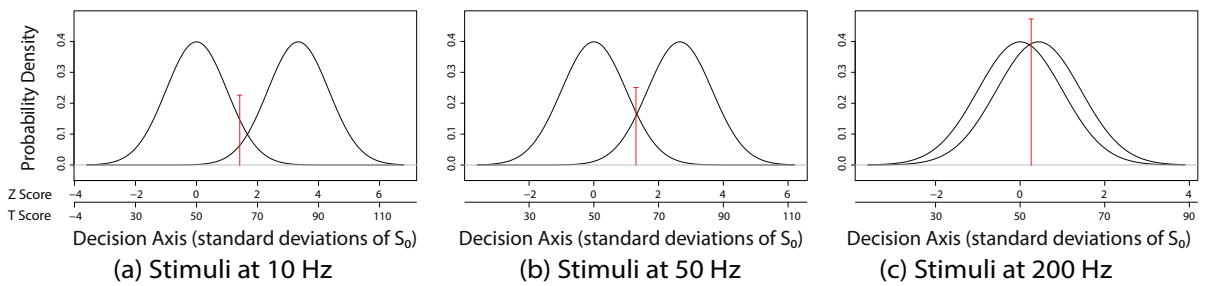


Figure 4.9: Probability density distributions of the added discrimination performances between stimuli classes of the five participants ( $P_1$  to  $P_5$ ). Panels (a), (b) and (c) correspond to the added responses at 10, 50 and 200 Hz, respectively. All computed decision criteria ( $c_a$ ) and their standard errors are marked in red in each panel. The corresponding T score values to the Z score values are shown in each panel.

presented a better performance using 200 Hz than 50 Hz. Participants  $P_2$  and  $P_4$  were not able to differentiate within stimuli classes at 200 Hz. Every participant had their individual best performance at 10 Hz. According to the parameter values showed in table 4.10, participant  $P_5$  was conservative with 10 and 50 Hz and liberal with 200 Hz, whilst participant  $P_1$  was consistently conservative.

The breakdown of the responses of  $P_1$ , who obtained the best performances for all three frequencies when discriminating within stimuli classes, are shown in Figure 4.11. It is illustrated that a large amount of hits and correct rejections lead to a high performance.

The added performance of all five participants is observed in Figure 4.12, where the panels correspond to the added responses for 10, 50 and 200 Hz when discriminating within stimuli classes. It is shown that the best added performance was achieved when using 10 Hz, and the worst performance when using 200 Hz.

## 4.5 Discussion

The saturation tests were quite uncomfortable for the participant. This is the reason why no further saturation experiments regarding other frequencies could be performed using the same fingers, since the participant described them as sore to the touch and sometimes numb for more than two days after running all six tests. Only three cases out of the 16 recorded sets of time ranges showed nerve recovery, matching or surpassing the first measured time range before saturation at the end of the trials (fingers 3 and 4 with stimulus  $B$  in panel (b) in Figure 4.3 and finger 1 with stimulus  $D$  in panel (d) in Figure 4.3). The noted saturation seemed to last longer than four hours, which was the time interval between the last two saturation tests.

The participant also noted that the sensations produced by the stimuli would change throughout the tests. During the first test the stimuli were described as suction and vibration, to then escalate along the following trials and be perceived as a hot needle or burning sensation and numbness. Changes in the perception of the stimuli would happen fairly quickly, thus resulting in a significant reduction of the time ranges before categorising the sensation as unpleasant or painful. Another interesting observation is that the unpleasant sensation was sometimes described to come in waves; i.e., after it was characterised as uncomfortable for a couple of seconds, it would seem tolerable for another couple of seconds right after that until it would become uncomfortable once more. This observation could be associated with sensory adaptation (reduction in sensitivity).

Regarding the paired comparison experiments, all participants noted that after running at least three tests in a row, the stimuli presented at 10 Hz were uncomfortable. This observation supported the hypothesis of reaching nerve saturation. They also reported some cases where they would feel their fingertip becoming numb; this effect was produced when only presenting stimuli from class  $ES_s$  ( $A$  and/or  $B$ ) at 200 Hz, hindering their capacity to perceive if this numbness

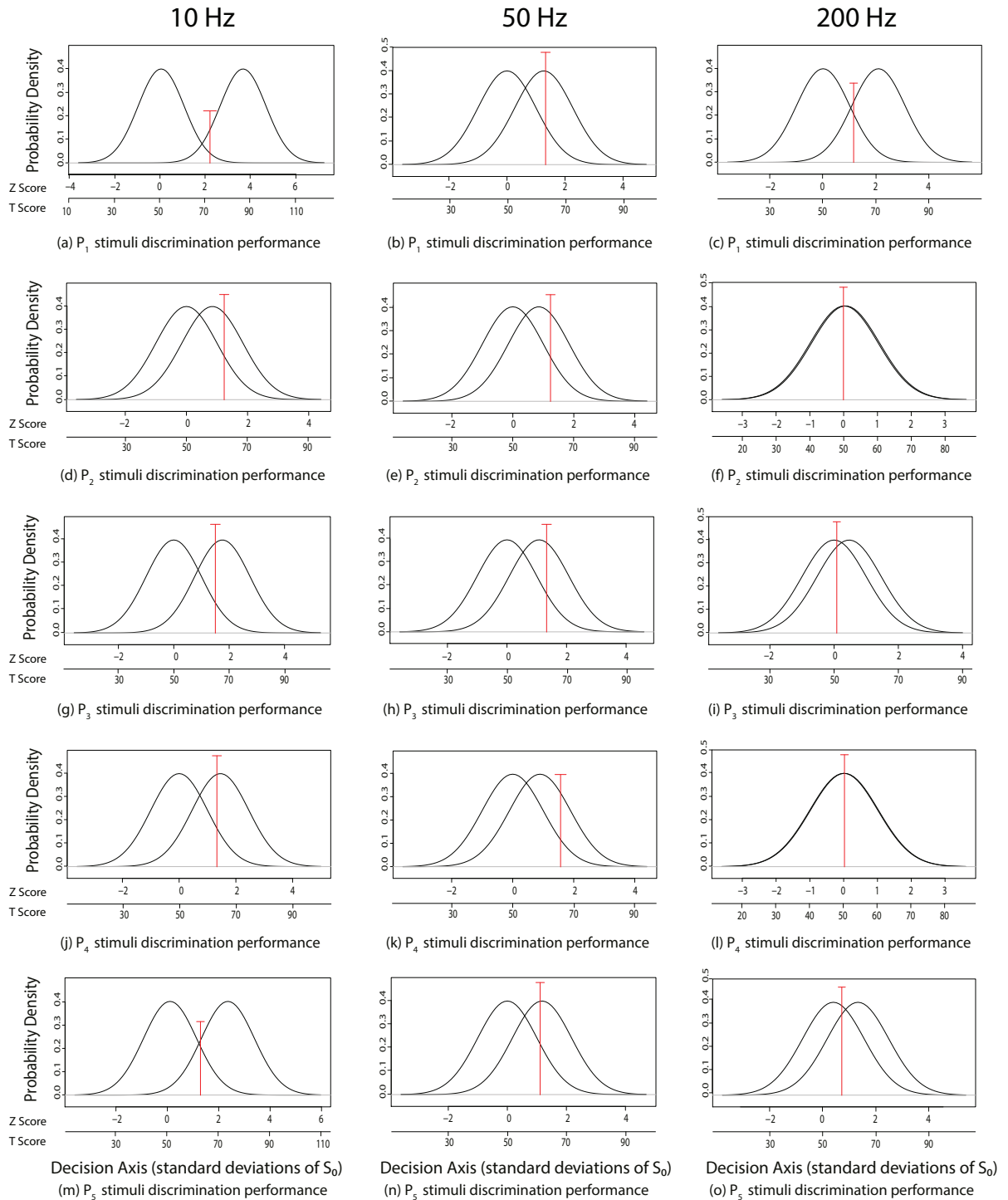


Figure 4.10: Probability density distributions of the discrimination performances within stimuli classes of the five participants ( $P_1$  to  $P_5$ ). Panels (a), (b) and (c) correspond to the responses of  $P_1$ , panels (d), (e) and (f) to  $P_2$ , panels (g), (h) and (i) to  $P_3$ , panels (j), (k) and (l) to  $P_4$ , and panels (m), (n) and (o) to  $P_5$ . Each column refer to the stimuli at 10, 50 and 200 Hz. All computed decision criterions ( $c_a$ ) and their standard errors are marked in red in each panel. The corresponding T score values to the Z score values are shown in each panel.

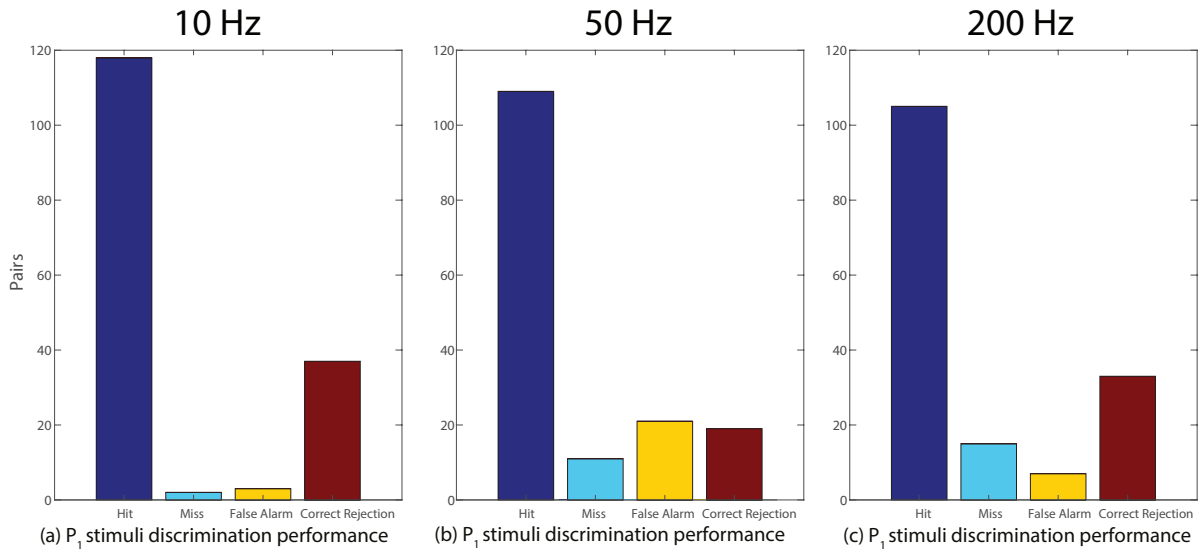


Figure 4.11: Number of hits, misses, false alarms and correct rejections of the best performances of the five participants when discriminating within stimuli classes. Panels (a), (b) and (c) correspond to the performance of  $P_1$  for 10, 50 and 200 Hz, respectively.

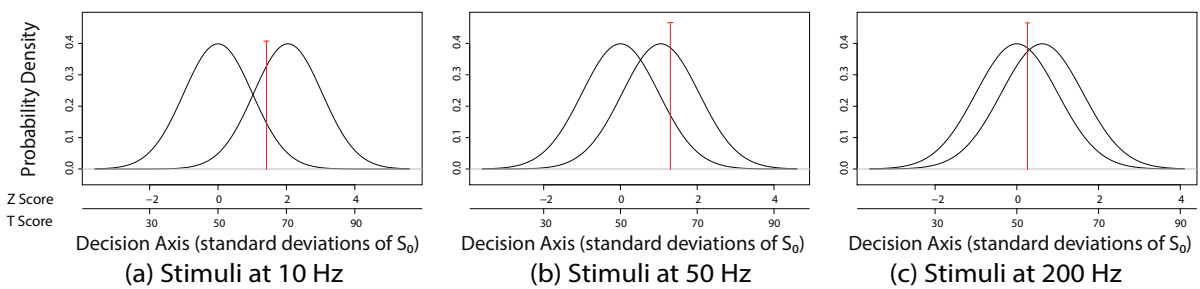


Figure 4.12: Probability density distributions of the added discrimination performances within stimuli classes of the five participants ( $P_1$  to  $P_5$ ). Panels (a), (b) and (c) correspond to the added responses at 10, 50 and 200 Hz, respectively. All computed decision criteria ( $c_a$ ) and their standard errors are marked in red in each panel. The corresponding T score values to the Z score values are shown in each panel.

was strictly the result of the presented stimuli or if it was a constant sensation related to either nerve saturation or sensory adaptation. Most of these reported cases corresponded to pairs where both presented stimuli were the same (i.e, either  $\langle AA \rangle$  or  $\langle BB \rangle$ ), suggesting that class  $ES_s$  produces an overstimulation at 200 Hz, related probably to the excitation of more than just the shallower fibres.

The average values of the statistics shown in tables 4.6, 4.8 and 4.10 depict that the best performance (largest  $d'$ ) was achieved discriminating between classes at 10 Hz. When the stimuli were presented at 50 Hz, the best performance was also achieved during the discrimination between stimuli classes. However, when using 200 Hz, the best performance was achieved during the discrimination within classes. It can also be observed that the average  $d'$  for all three frequencies when discriminating between classes, is greater than that regarding differentiation between all stimuli. It is also observed that, in average, the participants were better at discriminating between classes than within for frequencies 10 and 50 Hz, suggesting that the classes are activating different fibres (ergo producing different sensations) and within classes the same fibres are being activated.

Furthermore, the decision making proved to be less conservative when differentiating between stimuli classes than when discriminating between all stimuli (smaller  $\beta$ ) for all three frequencies. Discriminating within stimuli classes showed the most conservative behaviour of the participants at 10 and 50 Hz, as well as the smallest average  $d'$  for each frequency (comparing them to the average  $d'$  regarding discrimination between all stimuli and between stimuli classes). It should also be noted that, on average, all three discrimination tasks showed very little tendency to be conservative when making decisions involving stimuli at 200 Hz.

There is no general pattern of results throughout all three frequencies in the three discrimination tasks, except for the fact that the added performance of all five participants was better when using 10 Hz than when using 50 and 200 Hz (as depicted in Figures 4.6, 4.9 and 4.12). It can also be observed that, when using 10 Hz for all three discrimination tasks, the number of hits and correct rejections that the participants with best performances presented were larger than those obtained when using 50 and 200 Hz (as illustrated in Figures 4.5, 4.8 and 4.11). The best overall performance in all three discrimination tasks was achieved by participant  $P_1$ , showing a consistent conservative behaviour throughout all trials. Nevertheless, it can be observed in specific cases that other participants had better performances than  $P_1$  while showing a liberal behaviour, such as participant  $P_3$  during the discrimination between stimuli classes at 10 Hz and participant  $P_4$  during the same discrimination task at 10 and 50 Hz (table 4.8). Thus denoting that not always a conservative decision will lead to a better performance in the discrimination task; i.e.,  $d'$  and  $\beta$  are independent from one another.

## 4.6 Conclusion

The results obtained in this chapter show that different sensations can be produced by the developed TENS system. This can be observed in tables 4.6, 4.8 and 4.10, where the discriminability ( $d'$ ) of each participant is computed based on the perceived tactile sensations resulting of the presentation of the four different electrical stimuli. It is observed that not every participant has the same ability to differentiate between all stimuli, stimuli classes and within stimuli classes when using different frequencies. The discrimination between the presented stimuli appeared to be a difficult task as the frequency of the signal was increased. However, the performance of participant  $P_1$  serves as an example where it is shown that it is possible to discriminate the presented stimuli, thus indicating that the individual evoked sensations can be discriminated. The next step involves the comparison of the perceived sensations produced by the developed TENS system to those produced by a mechanical stimulation system, first in a simulation environment (presented in chapter 5) and finally using both the electrical and mechanical hardware implementations (detailed in chapter 6).





## COMPARISON BETWEEN ELECTRICAL AND MECHANICAL STIMULATION SIMULATION ENVIRONMENTS

In order to investigate the dissimilarity between the perceived sensations produced by the developed TENS system to those produced by a mechanical stimulation system, the first step was to compare both systems in a simulation environment. The first part of this chapter describes the mechanical stimulation model used to compare the modelled TENS output in chapter 2 when selectively stimulating modelled fibres. The second part of this section involves a general description of spike train metrics and different techniques to compare spike trains. Lastly, the implementation of an optimiser to search for the best values of the parameters of the ES simulation environment to produce a similar output to that of the mechanical stimulation environment is presented.

### 5.1 Mechanical Stimulation Simulation Environment

There are different documented models that represent the spatial properties of tactile stimuli [13, 68, 82]. Dandekar et al. presented a multilayered 3D human and monkey FEM that could predict the response of slowly adapting type 1 (SA1) afferents when static indentations of complex object shapes [13]. Phillips and Johnson modelled nonlinear responses of peripheral afferents through continuum mechanics that allowed the characterisation of the resulting tissue deformation and its impact on the mechanoreceptor [68]. Similarly, Sripathi et al. created a continuum mechanical model of the responses of SA1 and rapidly adaptive (RA) afferents to indented spatial patterns.

On the other hand, the model that includes the temporal properties of the mechanical stimuli was developed by Dong et al., predicting mechanoreceptive responses to new stimuli [16]. This model implements an integrate-and-fire (IF) model capable of replicating the properties of SA1,

RA and Pacinian (PC) fibres, predicting with millisecond accuracy the timing of individual spikes (as observed in Figure 5.1). 12 free parameters are used to define modelled neurons, as well as a saturating nonlinearity, which allows it to be applied to a wide range of stimuli. This model was selected to generate simulated nerve responses (presented as spike trains) to specific simulated stimuli to be compared to those from the modelled TENS system in chapter 2; i.e., modelled PC fibres and SA1 fibres (connected to Merkel disks), both running parallel to the skin at different depths.

In [16], the patterns of spikes resulting from multiple vibrations delivered to the skin through a punctuate probe without spatial elaboration from the ulnar and median nerves of four anesthetized Macaque monkeys (*Macaca mulatta*), were recorded using standard methods [87]. The mechanoreceptive afferents were classified through standard procedures [19, 20, 87] into SA1, RA and PC fibres. These single unit recordings were then used to train the IF model. The stimuli used for model fitting consisted of a set of sinusoidal, diharmonic, triharmonic and band-pass noise stimuli.



Figure 5.1: Mechanical stimulation model. Firstly, the displacement stimulus (position) is converted into velocity and acceleration signals. Each of the three signals is then separated into positive and negative components, rectified and multiplied by individual weights  $\omega_i$ . The resulting signals are then summed and passed through a saturation filter. The output of the saturation filter constitutes the current input for the integrate-and-fire model, where a spike is produced when the input current results in a depolarisation of the membrane potential beyond a defined threshold to then go back to the membrane resting potential. Reproduced from [16].

The model architecture is depicted in Figure 5.1. The position signal used to drive this model is the displacement ( $x$ ) of a probe on the skin. The velocity and acceleration correspond to the first and second derivative of  $x$ , respectively. All three signals are separated into their positive and negative components and then rectified and multiplied by an individual weight  $\omega_i$ . The signals are then summed and passed through a saturation filter (given by (5.1), where  $s$  is the weighted sum and  $I_0$  is the transduction current or saturation parameter). The output of the saturation filter serves as input to the IF model ( $I(t)$ ), which has two dynamic variables: membrane potential

and adaptive threshold.

$$(5.1) \quad S(s) = I(t) = \frac{I_0 s}{I_0 + |s|}.$$

The rate of change of the membrane potential  $V'(t)$  and the adaptive threshold  $\Theta'(t)$  are described by:

$$(5.2) \quad V'(t) = -\frac{1}{\tau} [V(t) - V_{rest}] + \frac{I(t) + I_{ind}(t)}{C},$$

$$(5.3) \quad \Theta'(t) = a [V(t) - V_{rest}] - b [\Theta(t) - \Theta_\infty],$$

where  $\tau$  is the membrane time constant,  $V_{rest}$  is the resting membrane potential,  $I_{ind}(t)$  is the spike-induced current,  $C$  is the capacitance of the model neuron,  $a$  is the threshold adaptation time constant,  $b$  is the inverse threshold rebound time constant and  $\Theta_\infty$  is the equilibrium threshold. The spike-induced current ( $I_{ind}(t)$ ) is produced by two kinds of ion channels ( $i_0$  and  $i_1$ ), each with a specific decay time constant ( $\tau_0$  and  $\tau_1$ , respectively) that allows the model to present different spiking behaviours, like burstiness. An action potential is originated when  $V(t) = \Theta(t)$ . Next,  $V(t)$  is reset to  $V_{rest}$  and the adaptive threshold is reset to  $\max[\Theta(t), \Theta_\infty]$ . The spike-induced currents are summed to the two channels, giving:

$$(5.4) \quad \begin{aligned} i_0 &\leftarrow i_0 + A_0, \\ i_1 &\leftarrow i_1 + A_1, \end{aligned}$$

where  $A_0$  and  $A_1$  represent the amplitudes of the spike-induced currents.

In summary, the model needs the definition of the 12 parameters per modelled neuron and the specific modelled mechanical stimulus to produce a spike train representing the response of the membrane potential  $V(t)$  to the presented stimulus. From the 12 parameters, four regard the spike generation:  $\tau$ ,  $a$  and the amplitudes of both spike-induced currents  $i_0$  and  $i_1$  ( $A_0$  and  $A_1$ , respectively). Seven other parameters describe the transduction model: the positive and negative components of the displacement, the positive and negative components of the velocity, the positive and negative components of the acceleration, and  $I_0$ . Finally, the last parameter is the transduction delay (see [47] for more detail).

## 5.2 Spike Train Metrics

Spike trains refer to a sequence of action potentials originating from one or more neurons; they are a time series of all-or-none events that occur during a determined time of observation. Spike

train metrics are a method used to quantify similarity and dissimilarity of spike trains by defining a measure of the distance between spike trains [34].

One of the popular ways to measure the similarity between two spike trains involves the calculation of the cross-correlation of the binned spike trains [3]. Nevertheless, it has been documented there is encoded information in the precise timing of the action potentials [63, 93]. Using measures based on binning the spike trains can lead to problems regarding estimation and quantisation of the spike times when the bin size is reduced [24].

Alternative binless spike metrics have been proposed, avoiding the difficulties previously discussed. Examples of these metrics include edit distance metrics such as the Victor-Purpura (VP) distance [91, 92], and kernel-based metrics such as the van Rossum's distance [90]. Edit distance metrics compute a measure of dissimilarity from the original pair of spike trains [34], whilst kernel-based metrics map spike trains into vector space to then compute the distance between the original spike trains using the Euclidean distance. The  $L_p$  norm of the difference between the estimated rate functions (where  $p \geq 1$ ) of two spike trains is the value of the metric between them. The  $L_p$  norm of a measurable function  $f$  on a measure space  $X$  is given by:

$$(5.5) \quad \|f\|_{L_p} = \left( \int x |f|^p \right)^{1/p};$$

when  $p = 2$ , the metric resembles Euclidean distances [17].

VP distance was the first binless proposed technique [94], addressing time warping. In this metric the distance between spike trains is defined as the cost in transforming one spike train into the other, preserving the integrity of single spikes instead of considering their contributions to a rate function [17]. There are three main operations regarding individual spikes: moving one spike to synchronise with the other, deleting a spike and inserting a spike [91, 92]. The resulting distance is the sum of the cost of each operation. The cost of aligning two spikes from different trains is represented by  $q\Delta t$ , where  $q > 0$ . Similarly, deleting or inserting a spike on either of the two trains has a cost of 1. The VP distance is therefore given by:

$$(5.6) \quad \sum_{i=1}^k q\Delta t_i + D_1 + D_2,$$

where  $\Delta t_i$  represents the differences between spike times in aligned pairs of spikes for  $i \in \{1, \dots, k\}$ .  $D_1$  and  $D_2$  correspond to the number of deleted spikes from the first and second spike trains, respectively. VP metric takes the minimum distance over all computed ways of aligning the trains [91, 92]. The disadvantage of this metric is that it matches an  $L_1$  norm on a vector space; this can complicate the results when embedding a group of spike trains produced by a common stimulus, resulting in a hyperbolic structure for the set of spike trains that is not observed in the stimulus space.

One alternative to the limitation of the VP distance is the generalised Victor-Purpura (GVP) metric, proposed by Dubbs et al. [17]. This metric is consistent with the idea that time-coding

of spike trains possess information beyond that conveyed by their firing rate, and presents all desirable properties of an  $L_p$  norm. If  $p = 1$ , the metric is equal to the original VP distance; on the other hand, if  $p = 2$ , embedded sets of spike trains "fit" in Euclidean space with significantly less difficulty than when using any other value for  $p \geq 1$  [17].

The GVP metric is given by:

$$(5.7) \quad \min \left[ \sum_{i=1}^k q^p \Delta t_i^p + D_1 + D_2 \right]^{1/p},$$

having  $p \geq 1$ . When  $p = 1$ , GVP metric is equal to the standard VP metric [17]. The GVP distance can be more mathematically specific using:

$$(5.8) \quad d_{p,q}[M](\mathbf{x}, \mathbf{y}) = \left[ \sum_{(x_i, y_j) \in M} q^p |x_i - y_j|^p + (m - |M|) + (n - |N|) \right]^{1/p},$$

where  $\mathbf{x} = \{x_i\}_{i=1}^m$  and  $\mathbf{y} = \{y_j\}_{j=1}^n$  are spike trains,  $M$  is a "matching" between the spike trains (i.e., a set of ordered pairs  $\{(x_{i1}, y_{j1}), \dots, (x_{ik}, y_{jk})\}$  where no element of  $\mathbf{x}$  or  $\mathbf{y}$  is repeated) and the number of ordered pairs in  $M$  is given by the cardinality of  $M$ ,  $|M|$ . Having  $\mathcal{M}$  as the set of all matchings, the GVP metric is defined as [17]:

$$(5.9) \quad d_{p,q}(\mathbf{x}, \mathbf{y}) = \min_{m \in \mathcal{M}} d_{p,q}[M](\mathbf{x}, \mathbf{y}).$$

## 5.3 Materials and Methods

### 5.3.1 MS Simulation Environment Implementation

Dong et al.'s mechanotransduction model described earlier in this chapter, was implemented in Matlab to model two nerve fibres: one SA1 and one PC, selecting the 12 parameters per fibre according to their respective documented values. Similarly, the properties of the mechanical stimulus are established; e.g. frequency, sampling frequency, gain, duration and wave form. The resulting stimulus signal is then differentiated to compute the corresponding velocity and acceleration. Next, the positive and negative components of all three signals (original stimulus; i.e., displacement, velocity and acceleration) are separated and rectified to then be multiplied by a specific weight  $\omega_i$ , taken from documented values in [16]. The sum of all these six parameters gives  $I_0$ , used as input current for the IF computation, where the membrane potential is calculated and compared to the threshold value to check if an action potential is generated. If an action potential is present, the membrane potential is set back to its resting potential. The modelled output includes the membrane potential, the spike train and an array of the timings where spikes were produced.

In order to evaluate the implementation of the mechanical stimulation model, two sine waves with documented frequencies and amplitudes required to produce one or two spikes per cycle (SPC) were used to simulate the response of a modelled SA1 fibre. Likewise, two other sine waves with documented frequencies and amplitudes that result in one or two SPC were used to model the response of a PC fibre. All stimuli were presented for one second.

After verifying the output of both the modelled SA1 and PC fibre, two sets of 20 frequencies and amplitudes for mechanical stimulation were generated. One set was designed to stimulate the SA1 fibre ( $MS_{SA1}$ ) and the other for the PC fibre ( $MS_{PC}$ ). Both sets were created under the condition that 10 of the stimuli had to produce on average one SPC and the other 10 had to result on average in two SPC in the fibre in question. The frequencies were randomly selected within a range of 10 to 100 Hz and the amplitudes within a range of 5 to 700  $\mu\text{m}$ . The spike trains resulting from each of the 20 simulated mechanical stimuli from both tests ( $S_{MS}$ ) were used to design an optimiser that adjusts the parameters describing the ES in order to minimise the difference between  $S_{MS}$  and the spike trains generated by the simulated TENS system ( $S_{ES}$ ). The frequencies, amplitudes and number of induced spikes of each of the 20 mechanical stimuli per set, are listed on table 5.1 (for the  $MS_{SA1}$  set) and 5.2 (for the  $MS_{PC}$  set). All stimuli were presented for one second.

Table 5.1: **Parameters of the mechanical stimuli set for the modelled SA1 fibre ( $MS_{SA1}$ ).**

Stimulus	Frequency / Hz	Amplitude / $\mu\text{m}$	Number of induced spikes
1	45	351	46
2	65	507	67
3	25	195	25
4	27	211	27
5	18	140	18
6	39	304	40
7	80	624	81
8	31	242	32
9	77	601	79
10	73	569	74
11	45	675	82
12	48	720	91
13	29	435	58
14	23	345	52
15	36	540	73
16	30	450	60
17	25	375	56
18	47	705	93
19	37	555	75
20	28	420	56

Table 5.2: Parameters of the mechanical stimuli set for the modelled PC fibre ( $MS_{PC}$ ).

Stimulus	Frequency / Hz	Amplitude / $\mu\text{m}$	Number of induced spikes
1	47	18	44
2	54	16	52
3	41	19	37
4	77	10	93
5	46	18	43
6	64	13	79
7	93	6	87
8	73	11	91
9	62	14	77
10	52	16	50
11	64	38	138
12	42	36	75
13	85	30	183
14	49	60	113
15	48	38	90
16	76	32	163
17	55	40	105
18	59	29	110
19	64	33	134
20	64	36	138

### 5.3.2 Spike Train Comparison Using GVP Metric

Since the comparison of the spike trains resulting from both the mechanical and the electrical stimulation model is an optimisation problem, a genetic algorithm was chosen as the technique to search for the optimum parameters of the ES model that would create a similar spike train to that obtained from the MS model. A genetic algorithm is an adaptive heuristics search biologically inspired by the theory of natural selection. It is an optimisation technique that allows the simulation of an evolution process within a set of candidates or individuals (potential optimum solutions) [52]. The parameters of each candidate are represented by a set of genes, generally computed as binary values. Another important characteristic of the genetic algorithms is the introduction of mutation. This process is based on random changes that help avoid local minima (that could lead to premature convergence) [95].

For this algorithm, firstly the initial population is created and their individual performance evaluated (i.e., computing their fitness). The fittest individuals are given a higher chance to reproduce than the rest of the population, creating the offspring through the crossover of their genes. This implies that the genes (parameters) from the fittest candidates are propagated to the next generations, allowing the creation of new individuals that could potentially have a better performance than either of their parents. Next, mutation is applied and the fitness of the offspring is computed, selecting the new fittest individuals for the next iteration. It should



be noted that the offspring replaces the individuals with poorer performance, keeping constant the number of candidates per generation. The algorithm can finish either when the fitness of the population converges to a certain value or when a defined number of iterations is reached (termination condition) [52]. This basic genetic algorithm logic is shown in Figure 5.2.

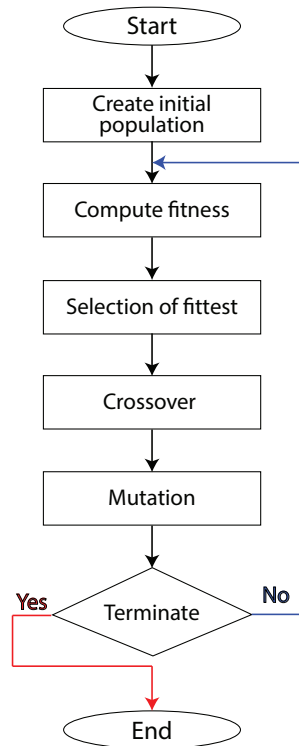


Figure 5.2: Flow chart representing the basic genetic algorithm structure.

The genetic algorithm was implemented in Matlab. From the modelled selective stimulation cases previously documented in chapter 2, the optimiser was used to compare each of the spike trains from 25 modelled cases where the eight electrode currents would selectively stimulate a shallower nerve (set  $ES_s$ ) to each of the 20 spike trains resulting from  $MS_{SA1}$ , and to compare each of the spike trains from 25 modelled cases where a deeper nerve would be activated (set  $ES_d$ ) to each of the 20 spike trains resulting from  $MS_{PC}$ . Therefore, the genetic algorithm was run 500 times when matching  $ES_s$  to  $MS_{SA1}$  and 500 times when matching  $ES_d$  to  $MS_{PC}$ . The eight electrode currents per modelled ES case are listed on table 5.3 for  $ES_s$  and on table 5.4 for  $ES_d$ .

The ES parameters to optimise were the frequency and the square pulse amplitude of the monophasic excitation signal of the modelled ES system (previously described in chapter 2), where the optimum values were searched within a range of [1,255] Hz and [0.1, 7] V. The optimiser was run using BlueCrystal Phase 3 (a supercomputer in the University of Bristol) [1], which limited the time it could run per trial to 350 hours. Taking this limitation into account, after running a couple of test trials with a population size of 100 individuals and 300 iterations, it was observed

Table 5.3: **Electrode currents for the set  $ES_s$  (all shown in mA).**

Stimulus	$I_{el,1}$	$I_{el,2}$	$I_{el,3}$	$I_{el,4}$	$I_{el,5}$	$I_{el,6}$	$I_{el,7}$	$I_{el,8}$
1	-2.38	1.75	2.12	1.65	-0.29	-1.52	-0.59	-0.74
2	-1.62	1.29	0.41	1.87	1.92	-0.78	-0.35	-2.74
3	-1.44	0.71	0.55	-0.10	2.77	0.36	-1.51	-1.33
4	-1.37	0.75	-0.10	1.19	-0.53	1.02	-1.36	0.39
5	-1.36	1.18	-1.28	1.55	-0.24	0.74	-0.30	-0.29
6	-1.27	1.33	0.86	-0.03	-0.19	-0.15	-0.58	0.04
7	-1.12	0.77	0.25	1.16	-0.64	-0.11	-0.06	-0.24
8	-1.10	0.90	0.30	0.18	1.06	-0.75	0.47	-1.06
9	-0.92	-1.07	1.39	1.18	2.44	-0.87	-0.98	-1.17
10	-0.76	-0.54	0.37	0.75	0.55	-0.62	0.69	-0.45
11	-0.68	-0.40	0.11	1.29	0.53	0.61	0.34	-1.80
12	-0.53	-0.18	0.64	0.17	0.52	-0.05	-0.70	0.14
13	-0.23	-0.77	1.07	-0.64	0.53	1.06	0.27	-1.30
14	-0.15	0.01	0.09	0.01	0.05	0.01	0.01	-0.01
15	-0.14	-1.69	1.63	1.16	0.69	-0.81	1.05	-1.90
16	-0.14	-0.11	0.90	-0.60	0.77	-1.01	-0.34	0.53
17	-0.13	0.06	0.04	-0.06	0.08	0.06	-0.14	0.09
18	-0.08	-0.01	0.10	-0.10	-0.01	0.10	-0.01	-0.02
19	-0.05	0.05	-0.01	-0.02	0.04	-0.03	0.06	-0.06
20	-0.04	0.13	-0.08	-0.09	0.09	0.03	0.01	-0.05
21	-0.03	0.04	0.06	0.33	-0.70	0.27	-0.10	0.12
22	-0.03	-0.01	0.01	-0.01	-0.05	0.09	-0.07	0.07
23	-0.01	-0.16	0.07	0.12	0.04	0.03	-0.12	0.03
24	0.02	-0.01	0.01	-0.05	-0.06	-0.02	0.09	0.01
25	0.06	-0.07	-0.05	0.05	-0.08	0.04	0.07	-0.02

that the optimiser could only run for half of the iterations within the 350 hour-limit. Therefore, the population size was set to 60 individuals and 200 iterations, considering as well that a smaller population size is believed to result in quicker convergence speed. Each individual had 15 genes as binary values or bits. For the amplitude, three genes represented the integer value and four genes represented the decimals. The other eight genes corresponded to the frequency (integer values). 16 offspring with a mutation rate of 4 (i.e., affecting a quarter of the offspring) were created per iteration. The mutation rate was chosen following the recommendation in [52], where it is suggested to set the mutation rate to  $1/N$ , where  $N$  is the length of the bit string (in this case,  $N = 15$ ). A 2-point crossover was implemented, where the location for both crossover points was selected randomly. The fitness of each individual was estimated by running the ES simulation environment (described in chapter 2) to compute the corresponding spike train and compare it to that from the matching modelled MS using the GVP distance, given by equation 5.8, with  $p = 2$  (allowing the metric to resemble Euclidean distances) and  $q = 0.01$ . The selected value for  $q$  was hand-tuned after running some tests and verifying this value would provide a significantly

Table 5.4: **Electrode currents for the set  $ES_d$  (all shown in mA).**

<b>Stimulus</b>	$I_{el,1}$	$I_{el,2}$	$I_{el,3}$	$I_{el,4}$	$I_{el,5}$	$I_{el,6}$	$I_{el,7}$	$I_{el,8}$
1	-2.01	1.99	0.71	-0.59	-0.05	1.04	-1.97	0.88
2	-1.55	1.94	1.59	-0.85	-1.44	0.36	0.66	-0.70
3	-1.31	1.01	-0.68	-0.56	1.10	2.16	-1.10	-0.63
4	-0.80	1.37	0.54	-0.21	1.15	-1.19	-1.60	0.74
5	-0.72	-0.28	-0.95	1.46	1.72	-0.69	-0.58	0.05
6	-0.61	0.01	-0.94	1.37	1.86	-0.17	-0.94	-0.58
7	-0.36	0.67	0.20	0.56	-0.22	-0.42	-0.49	0.06
8	-0.29	0.37	0.18	0.33	-0.07	-0.45	0.29	-0.35
9	-0.29	0.38	-0.03	-0.11	0.32	0.33	-0.27	-0.33
10	-0.25	0.22	-0.03	0.01	0.16	0.01	0.23	-0.34
11	-0.08	-0.01	0.13	-0.11	-0.05	0.11	-0.17	0.18
12	-0.07	0.58	-0.44	0.09	-0.09	-0.07	-0.41	0.41
13	-0.03	-0.10	-0.01	-0.03	0.05	0.15	-0.13	0.11
14	-0.01	0.14	-0.06	-0.07	0.13	0.04	-0.33	0.16
15	0.02	-0.59	-0.33	1.16	0.68	-0.04	-0.66	-0.25
16	0.04	-0.05	-0.08	0.05	-0.09	0.10	0.02	-0.01
17	0.05	-0.09	-0.06	0.06	-0.09	0.10	0.03	-0.01
18	0.11	-0.08	-0.01	0.09	-0.01	-0.01	-0.08	-0.02
19	0.16	-0.09	0.01	-0.05	0.05	-0.05	-0.08	0.04
20	0.22	1.08	-1.01	0.22	-0.49	0.80	-0.71	-0.11
21	1.06	1.21	-0.76	0.64	-0.61	-0.82	-1.15	0.44
22	1.50	-0.17	0.23	0.46	1.47	-1.74	-0.68	-1.07
23	1.52	-0.80	1.27	-1.03	1.35	-1.31	0.89	-1.91
24	2.08	0.46	-0.11	-1.39	-0.95	-0.02	0.38	-0.45
25	2.40	-0.29	0.55	1.17	0.95	-1.47	-2.16	-1.15

small value when the spiking trains were similar and a significantly large value when they were different.

The fitness is inversely proportional to the computed GVP distance (i.e., a greater distance or dissimilarity will result in a poor fitness value and vice versa). The output from each of the 500 individually run optimisers was saved in a .txt file, where all generations were logged including all genes from each individual, as well as their fitness. 58% of the cases reached the 200 iteration between six to ten days; nevertheless, the resting 42% stopped before reaching the 200 iteration-condition due to the time limit from the supercomputer.

## 5.4 Results

### 5.4.1 Verification of the MS Simulation Environment Implementation

The implementation of the MS model developed by Dong et al. [16] was verified by testing four different mechanical stimuli. Two of them were documented to produce one SPC in a modelled SA1 and a PC fibre respectively, and the other two were documented to induce two SPC in the corresponding fibre.

#### 5.4.1.1 Testing Modelled SA1 Response

The frequencies and amplitudes of the mechanical stimuli for the modelled SA1 are listed on table 5.5, along with the documented resulting SPC [16] and the modelled SPC. The corresponding membrane potential ( $V(t)$ ) to each of the two tested mechanical stimuli is illustrated in Figure 5.3. Panel (a) shows the mechanical stimulus 1, which induced one SPC in average (as observed in panel (b)). Panel (c) depicts the mechanical stimulus 2, which resulted in two SPC on average (as presented in panel (d)).  $V_{rest}$  is shown in green in panels (b) and (d), where it is noted that the membrane potential goes back to this resting potential value after a spike is induced.

Table 5.5: Mechanical stimuli used to test the modelled SA1 fibre response.

Stimulus	Frequency / Hz	Amplitude / $\mu\text{m}$	Documented SPC	Modelled SPC
1	40	200	1	1
2	20	320	2	2

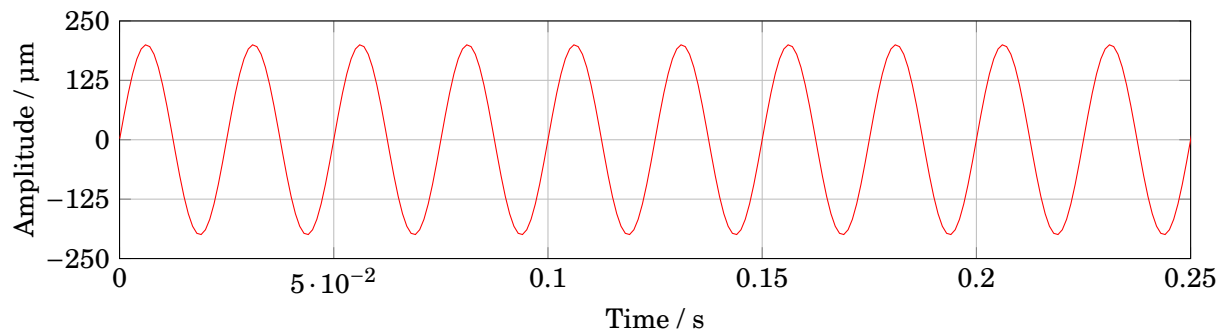
#### 5.4.1.2 Testing Modelled PC Response

The parameters (frequencies and amplitudes) of the two mechanical stimuli for the modelled PC are listed on table 5.6, as well as the documented resulting SPC [16] and the modelled SPC. The modelled membrane potential ( $V(t)$ ) resulting from each of the two tested mechanical stimuli is illustrated in Figure 5.4. Panel (a) shows the mechanical stimulus 1, which produced one SPC in average (as noted in panel (b)). Panel (c) shows the mechanical stimulus 2, which induced two SPC on average (as depicted in panel (d)).  $V_{rest}$  is shown in green in both panels (b) and (d), where it is observed that the membrane potential goes back to this resting potential value after a spike is produced.

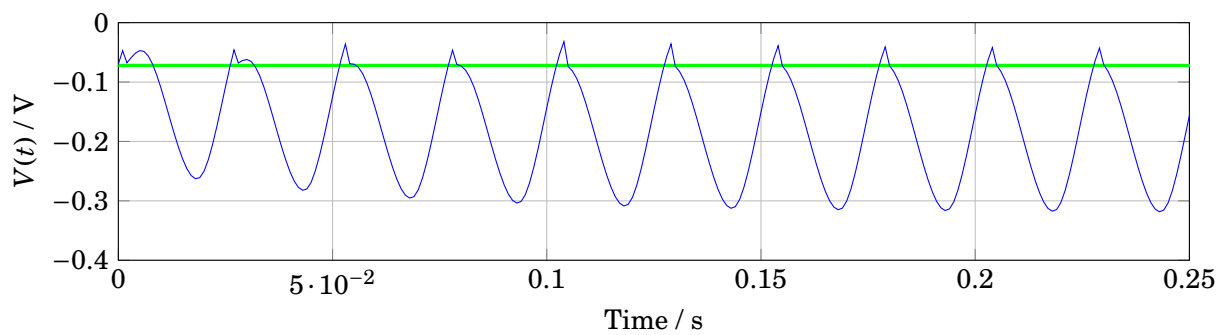
Table 5.6: Mechanical stimuli used to test the modelled PC fibre response.

Stimulus	Frequency / Hz	Amplitude / $\mu\text{m}$	Documented SPC	Modelled SPC
1	20	65	1	1
2	40	75	2	2

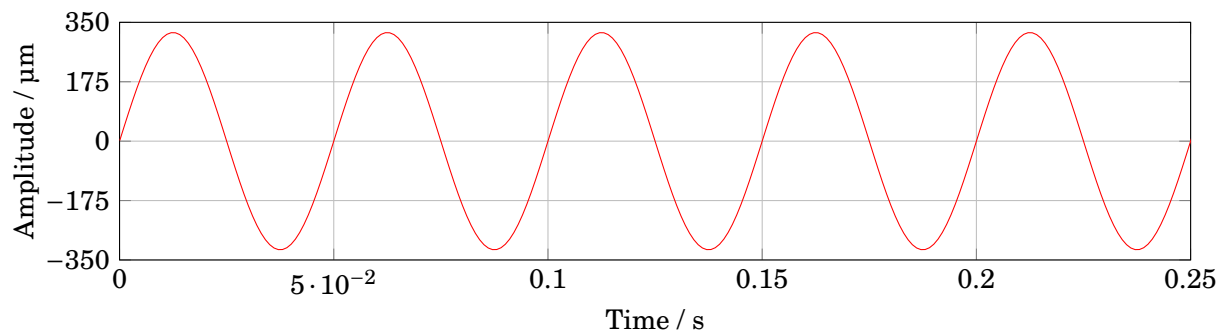
CHAPTER 5. COMPARISON BETWEEN ELECTRICAL AND MECHANICAL STIMULATION  
SIMULATION ENVIRONMENTS



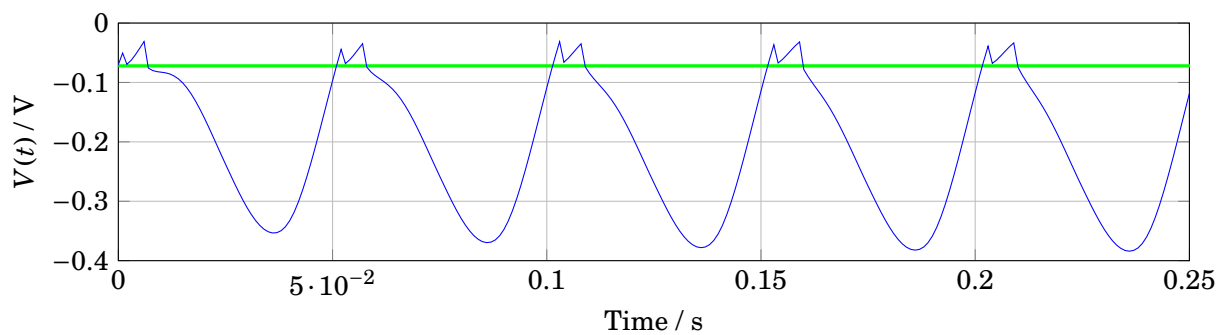
(a) Modelled mechanical stimulus 1



(b) Membrane potential  $V(t)$  of the modelled SA1 fibre when stimulus 1 is presented

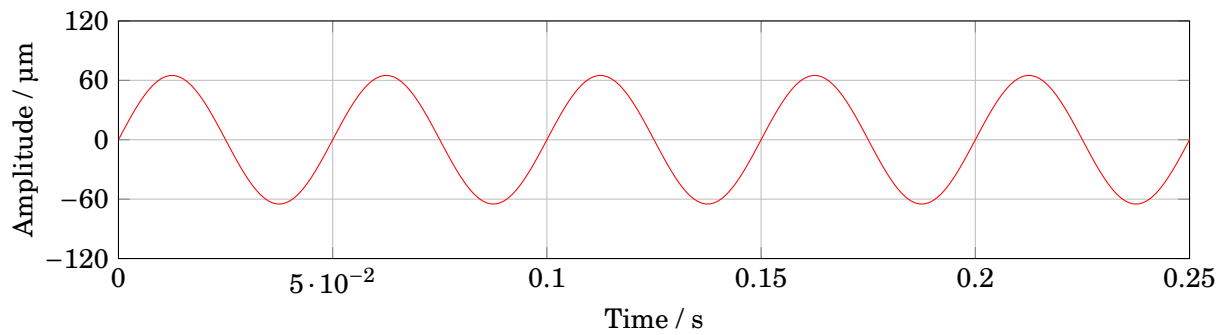


(c) Modelled mechanical stimulus 2

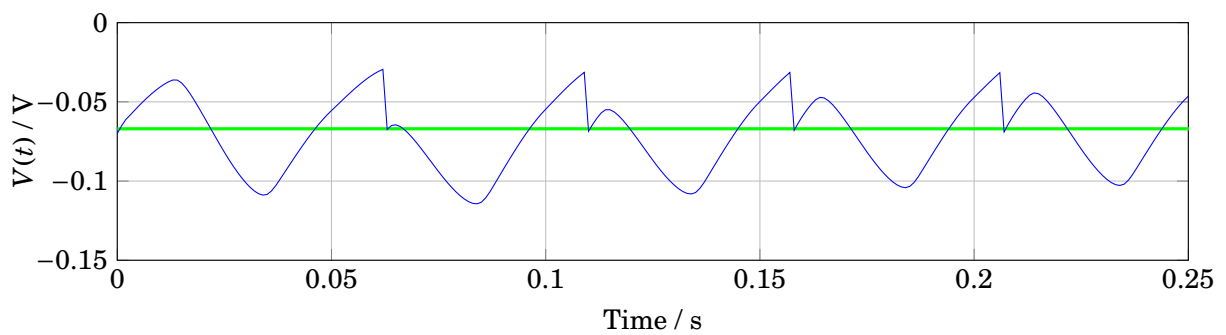
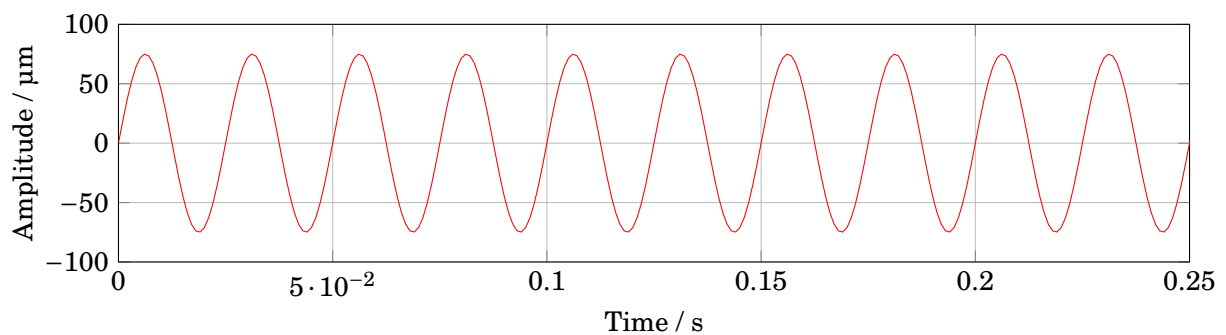


(d) Membrane potential  $V(t)$  of the modelled SA1 fibre when stimulus 2 is presented

Figure 5.3: Mechanical stimuli presented for verification of the modelled membrane potential of a SA1 fibre. Panels (a) and (c) show the mechanical stimulus waveforms, and panels (b) and (d) the corresponding membrane potential, with  $V_{rest}$  shown in green.



(a) Modelled mechanical stimulus 1

(b) Membrane potential  $V(t)$  of the modelled PC fibre when stimulus 1 is presented

(c) Modelled mechanical stimulus 2

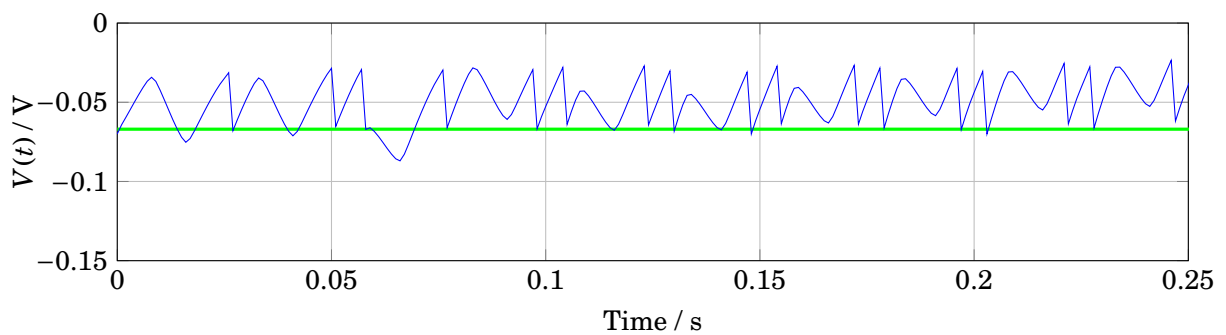
(d) Membrane potential  $V(t)$  of the modelled PC fibre when stimulus 2 is presented

Figure 5.4: Mechanical stimuli presented for verification of the modelled membrane potential of a SA1 fibre. Panels (a) and (c) show the mechanical stimulus waveforms, and panels (b) and (d) the corresponding membrane potential, with  $V_{rest}$  shown in green.

### 5.4.2 Spike Train Comparison

After analysing all 500 cases matching the MS set  $MS_{SA1}$  to the ES set  $ES_s$ , it was found that the 20 fittest pairs corresponded to the stimuli listed on table 5.7, where it is noted that some mechanical stimuli were optimally matched to more than one electrical stimulus (e.g., stimuli 10, 2, 4, 3 and 1). Similarly, some electrical stimuli were optimally matched to more than one mechanical stimulus (e.g., stimuli 25, 5 and 23).

Table 5.7: Fittest pairs of MS and ES when matching  $MS_{SA1}$  to  $ES_s$ .

Mechanical stimulus	Electrical stimulus	Fitness
10	25	9756.5
10	5	9700.3
10	22	9606.1
2	25	9599.7
2	21	9580.9
5	25	9464.0
15	7	9439.0
1	10	9379.0
4	15	9291.3
3	5	9273.2
8	14	9167.4
4	10	9138.9
3	19	9136.4
1	3	9132.0
18	23	9105.3
1	4	9099.5
1	19	9058.3
1	23	9046.8
16	3	9039.0
8	12	9022.3

Five matched pairs were chosen from table 5.7 (marked in red) to be implemented on a MS system (further described in chapter 6) and on the previously described TENS system chapter 3 in order to investigate the perceived tactile sensations produced with the corresponding stimuli. The selection of the pairs was conditioned to the MS hardware limitations regarding the amplitude of the modelled mechanical stimulus (i.e., the modelled amplitudes had to match the displacement range of the vibrotactile stimulator), which will be described in chapter 6.

Evaluating the 500 cases matching the MS set  $MS_{PC}$  to the ES set  $ES_d$ , the 20 fittest pairs corresponded to the stimuli listed on table 5.8. It is also noted (similarly to the matching of the other two sets) that some mechanical stimuli were optimally matched to more than one electrical stimulus (e.g., stimuli 1, 4, 3, 7 and 13). Similarly, some electrical stimuli were optimally matched to more than one mechanical stimulus (e.g., stimuli 2, 3 and 25). The fittest five matched pairs were selected from table 5.8 (marked in red) to be used on the MS system chapter 6 and on the

previously presented TENS system chapter 3 to study the perceived tactile sensations produced with the corresponding stimuli.

Table 5.8: **Fittest pairs of MS and ES when matching  $MS_{PC}$  to  $ES_d$ .**

Mechanical timulus	Electrical stimulus	Fitness
6	3	9941.2
1	8	9929.8
4	15	9799.1
8	9	9647.6
2	20	9646.0
4	17	9566.5
15	2	9537.5
13	22	9537.3
7	12	9536.9
11	25	9430.7
3	19	9423.9
4	5	9421.3
17	20	9418.8
10	3	9410.6
4	23	9406.1
3	14	9399.0
9	9	9376.7
16	25	9315.7
7	2	9315.7
13	25	9213.2

Each matched pair from tables 5.7 and 5.8 showed multiple optimised frequencies and amplitudes (highly fitted individuals) for the electrical stimulus in question. The values of these parameters to test on the TENS system were chosen following the condition that, if possible, the selected frequency could be coupled with multiple amplitude values to result in highly fitted modelled individuals. This was considered because, for the next round of psychophysical experiments, each participant would calibrate the amplitude of the electrical stimuli. Therefore, it was prioritised to have the fitness relying mostly on frequency than on modelled amplitude. Two examples of how the optimised frequencies were selected for each electrical stimulus are illustrated in Figures 5.5 to 5.8.

Figure 5.5 shows the optimisation results when matching mechanical stimulus 5 from set  $MS_{SA1}$  to electrical stimulus 25 from set  $ES_s$ . It can be seen that the fittest individuals are clustered around three frequencies: 20, 75 and 140 Hz. The largest cluster is highlighted in red, and it is additionally explored in Figure 5.6, where it is noted that multiple amplitudes are paired up with a mean frequency of 16 Hz; thus meeting the condition of a frequency that could be coupled with multiple amplitude values to result in highly fit individuals.

In the same way, Figure 5.7 shows the optimisation results when matching mechanical



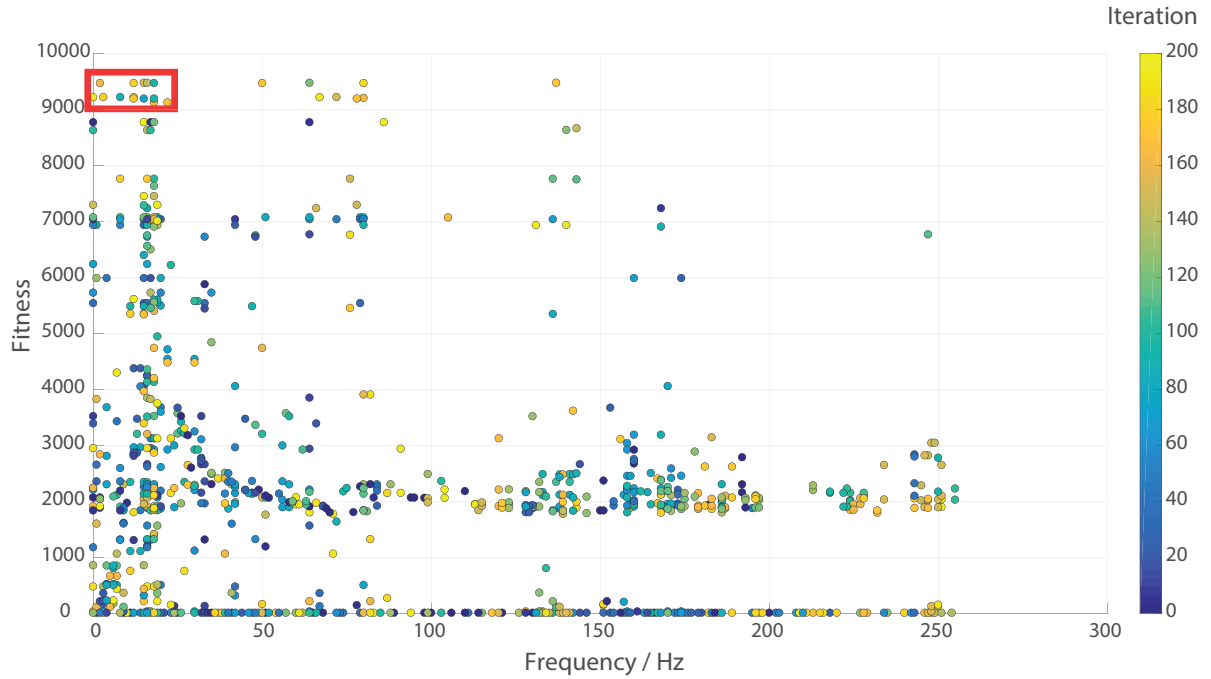


Figure 5.5: Optimisation results when matching mechanical stimulus 5 from  $MS_{SA1}$  to electrical stimulus 25 from  $ES_s$ . The colour of the data points corresponds to the iterations of the optimiser. The largest cluster of fittest individuals is highlighted in red.

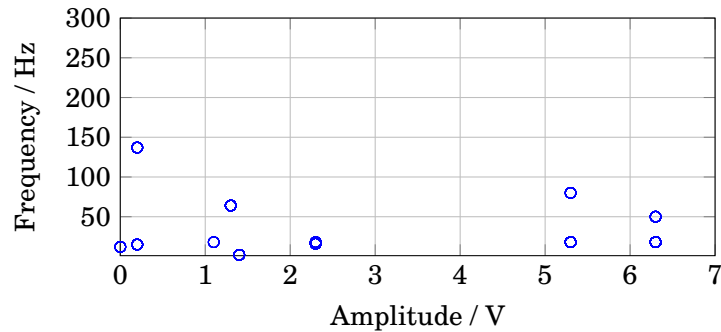


Figure 5.6: Optimised ES frequencies and amplitudes when matching mechanical stimulus 5 from  $MS_{SA1}$  to electrical stimulus 25 from  $ES_s$ .

stimulus 6 from set  $MS_{PC}$  to electrical stimulus 25 from set  $ES_s$ . In this case, the fittest individuals are clustered around 100 Hz, highlighted in red. Figure 5.8, illustrates that the majority of the fittest individuals are located around an amplitude of 5 V, with a mean frequency of 97 Hz.

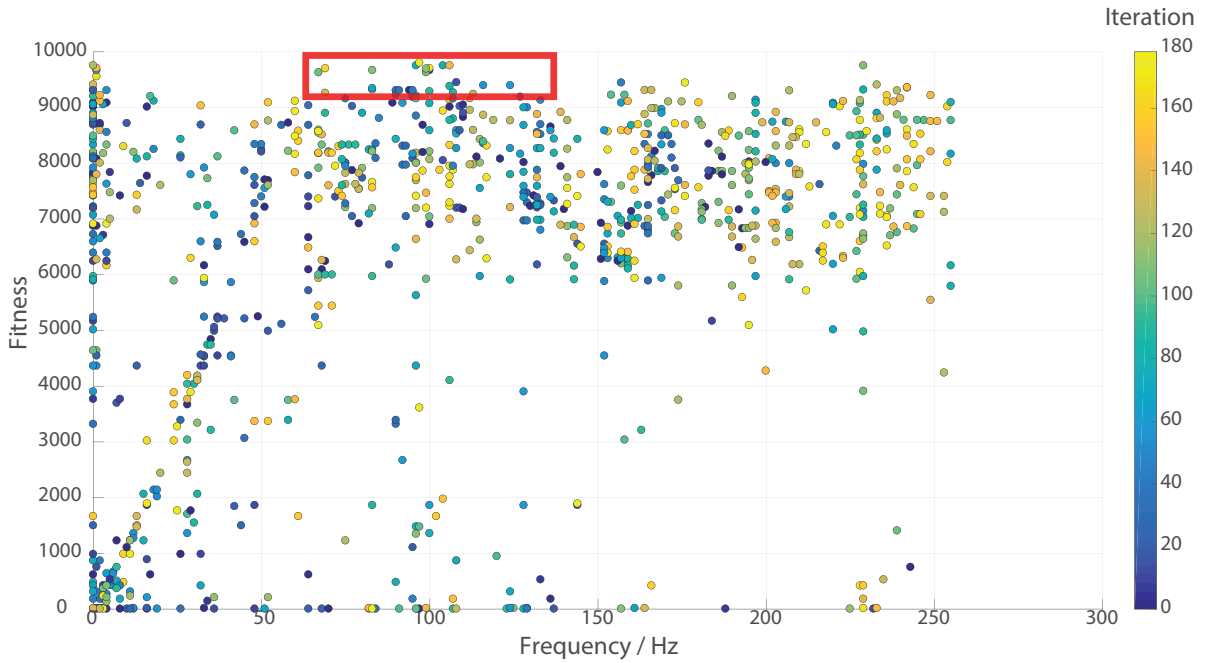


Figure 5.7: Optimisation results when matching mechanical stimulus 6 from  $MS_{PC}$  with electrical stimulus 3 from  $ES_d$ . The colour of the data points corresponds to the iterations of the optimiser. The largest cluster of fittest individuals is highlighted in red.

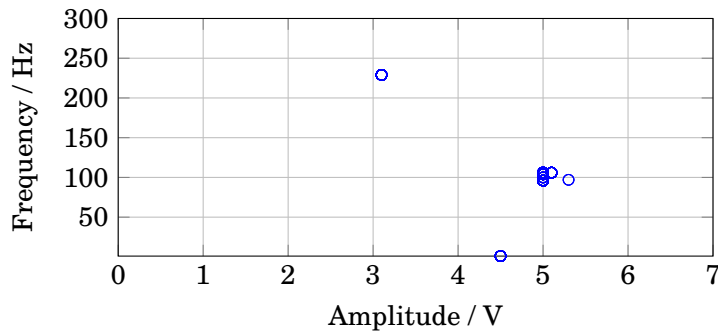


Figure 5.8: Optimised ES frequencies and amplitudes when matching mechanical stimulus 6 from  $MS_{PC}$  to electrical stimulus 3 from  $ES_d$ .

## 5.5 Discussion

The results obtained from the verification of the MS model were consistent with those documented by Dong et al [16]. For both modelled fibres (SA1 and PC), stimulus 1 induced an average of one SPC, and stimulus 2 an average of two SPC. The spikes are counted when the membrane potential is reset to  $V_{rest}$ ; i.e., when the modelled  $V(t)$  reaches the green line in panels (b) and (d) in Figures 5.3 and 5.4.

Once the model was verified, the use of the GVP distance to measure the dissimilarity between spike trains produced by modelled mechanical and electrical stimuli, implemented as the fitness

function of the genetic algorithm, resulted in multiple fit individuals (solutions) per optimised pair. The fittest individuals appear as clusters around certain frequencies and amplitudes, which allows the selection of the optimum parameters according to different criteria. For this case, the optimum frequencies were chosen to match multiple amplitudes when possible (as illustrated in Figure 5.6, where the selected frequency was 16 Hz), taking into account that the real amplitudes would be selected by the participants while calibrating the TENS system to run the next round of psychophysical tests, without sacrificing the fitness. Nevertheless, there were also some cases where the amplitudes were in a cluster, thus limiting the amplitude range for the selected frequency (e.g., Figure 5.8, where the selected frequency was 97 Hz).

The results from the genetic algorithm show that by changing the frequency and pulse amplitude of the electrical stimuli, and keeping constant the electrode currents, some electrical stimuli can be adjusted to produce the equivalent number of SPC to that induced by a specific mechanical stimulus. One example involves electrical stimulus 3 from  $ES_s$ , which was present twice in table 5.7 matching mechanical stimulus 1 (known to produce one SPC) and mechanical stimulus 16 (known to produce two SPC) from  $MS_{SA1}$ . Analogously, electrical stimulus 20 from  $ES_d$  matched mechanical stimulus 2 from  $MS_{PC}$  producing one SPC, and also matched mechanical stimulus 17 from  $MS_{PC}$  producing two SPC.

## 5.6 Conclusion

In order to find an electrical stimulus whose output (spike train) would match that of a mechanical stimulus, an optimiser can be implemented, such as a genetic algorithm. In this chapter, the implementation of the GVP distance in a genetic algorithm (approach used to measure the dissimilarity between the responses produced by a specific mechanical and electrical stimuli) resulted in highly fitted values for the frequency and amplitude pulse of electrical stimuli to match the output (spike train) of specific mechanical stimuli (as observed in tables 5.7 and 5.8).

The next comparison task involves 10 optimum matched mechanical and electrical stimuli (marked in red in tables 5.7 and 5.8), which were selected to further test in the hardware implementation of the MS system and the TENS system (previously described in chapter 3), through a series of psychophysical tests to evaluate their performance and similarity, detailed in chapter 6.

## COMPARISON BETWEEN ELECTRICAL AND MECHANICAL STIMULATION HARDWARE SYSTEMS

In this chapter, the final stage of this project is presented. It involves the comparison between the perceived tactile sensations produced by the TENS system (described in chapter 3) and those produced by a mechanical stimulation, further characterised in this chapter. Similar to the experiments introduced in chapter 4, a series of psychophysical experiments are detailed, with the aim to analyse the relationship between the perceived sensations produced by both mechanical and electrical stimulation systems. The selected stimuli (both electrical and mechanical) are the optimum matching pairs originated from the comparison between the spike trains resulting from the electrical and mechanical simulation environments (presented in chapter 5).

Multiple examples of systems combining electrical and mechanical stimulation have been documented [51, 65, 100]. Mizuhara et al. presented a tactile stimulation system that produced "strong and natural" sensations, enhancing the mechanical stimulation by adding electrical stimulation [65]. Komurasaki et al. proposed an integrated tactile display using electrovibration and electrical stimulation using the micro-fabrication process, studying if multiple stimuli could be perceived [51]. Yem et al. documented a system combining cathodic electrical stimulation and mechanical damped sinusoidal vibration to reproduce sensations of softness or hardness [100]. These examples show a growing interest in studying the combined effect of both stimulation techniques, contrary to the direct comparison between electrical and mechanical stimulation.

Yem et al. investigated the relationship between the intensity sensation of electrical and mechanical stimulation [99]. During their experiments, the participants used their middle finger to get an electrical stimulus of 30 Hz (presented every one second), and were asked to match the perceived intensity to that of an adjustable mechanical stimulus attached to their index finger. The hardware used to control the waveform of the electrical stimulus during the experiments

involved a microcontroller, a high-speed DAC and a VI converter. The electrode array consisted of a 3x3 matrix of circular electrodes, where the middle electrode was the active electrode and the other eight were neutral electrodes. The mechanical system consisted of a microcontroller, two DC motors and a motor driver to control the end-effector, which had a 0.5 mm in diameter and was located in the centre of a hole with 8 mm in diameter. The surface of the hole served as a base to support the fingertip, allowing a constant contact with the end-effector. Their system is shown in Figure 6.1. Their results indicated that anodic stimulation resulted mainly in the sensation of vibration, and cathodic stimulation resulted in both pressure and vibration sensations.

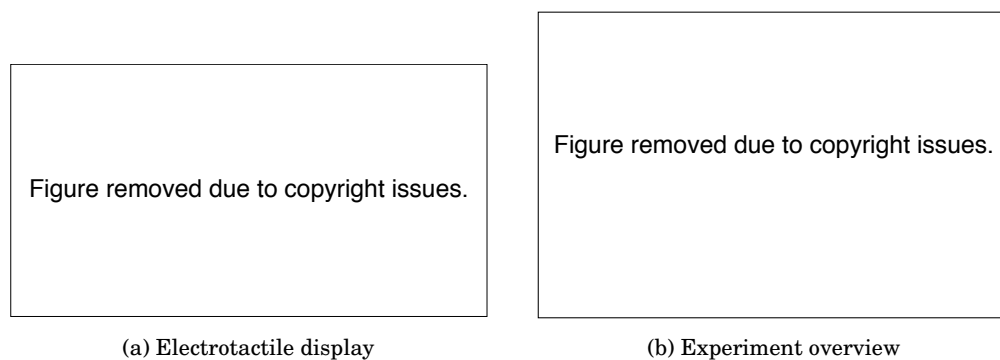


Figure 6.1: Hardware implementation to compare the intensity sensation of electrical and mechanical stimulation. Panel (a) shows the electro tactile display with the 3x3 electrode matrix. Panel (b) shows the experiment setup, where the index and middle fingers of the right hand were presented with mechanical and electrical stimulation, respectively. Taken from [99].

Contrary to the correlation in [99], the comparison presented in this chapter regards the similarity between the perceived tactile sensations produced by a TENS system (described in chapter 3) and those produced by a mechanical stimulation system, with all stimuli targeting modelled selective stimulation of either a shallower fibre (SA1) or deeper fibre (PC).

## 6.1 Materials and Methods

### 6.1.1 Mechanical Stimulators

#### 6.1.1.1 Brüel & Kjær Minishaker 4810

The Brüel & Kjær Minishaker 4810 (shown in panel (a) in Figure 6.2) is a compact electrodynamic exciter with a suspension system that guarantees a rectilinear motion and a permanent field magnet. The force rating of this stimulator is up to 10 N, its frequency range is 0 to 18 kHz and the maximum displacement it presents is equal to 4 mm (peak-to-peak) [50]. It is 76 mm in diameter and 75 mm in height, and its end effector is 14 mm. The performance of this minishaker is optimised using the Brüel & Kjær Power Amplifier 2718 (illustrated in panel (b) in Figure 6.2), which drives the stimulator safely to its full rating.

The amplifier shows a flat frequency response within the range of 10 Hz to 20 kHz ( $\pm 0.5$  dB). This is illustrated in Figure 6.3, where both the input (channel 2 in blue) and output (channel 1 in orange) signals are 10 V<sub>pp</sub> at 50 Hz. The maximum voltage gain of the amplifier is 40 dB, the power output capability is equal to 75 VA and it has a continuously variable current limit of 1 A to 5 A(RMS) [49].

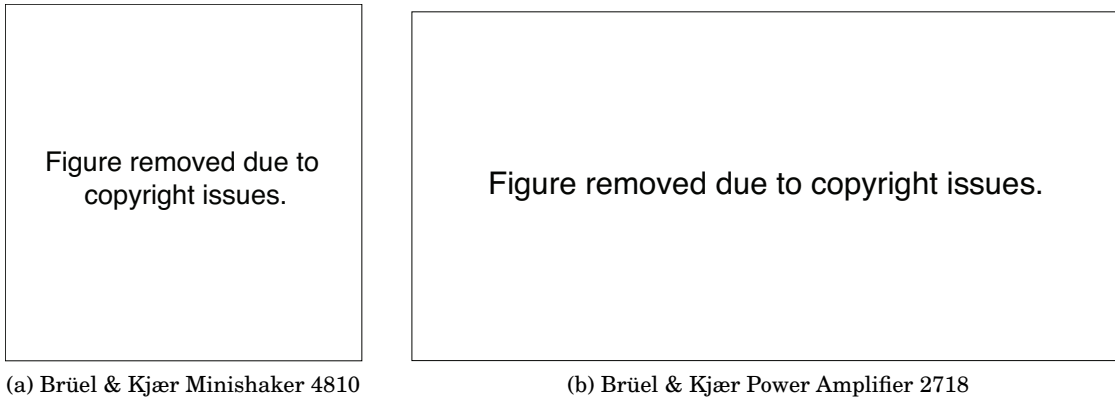


Figure 6.2: Brüel & Kjær mechanical stimulation system. Panel (a) shows the mechanical stimulator and panel (b) shows the corresponding amplifier to drive the stimulator. Taken from [49, 50].

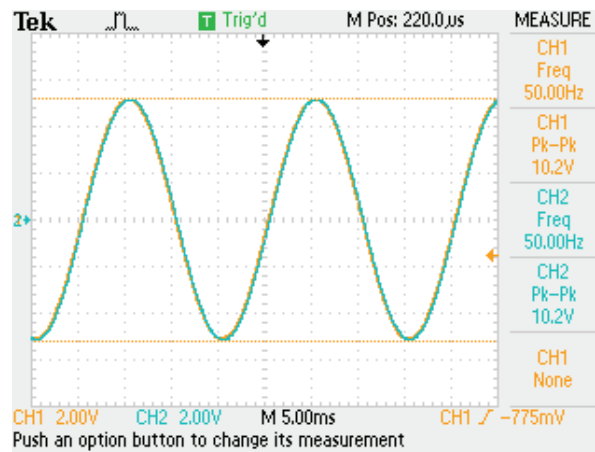


Figure 6.3: Brüel & Kjær Power Amplifier output voltage when using an input signal of 10 V<sub>pp</sub> at 50 Hz. Channel 1 corresponds to the output and channel 2 to the input signal.

### 6.1.1.2 Dancer Design Tactor

The Dancer Design tactor (displayed in Figure 6.4, with the end effector coloured in red) is a miniature vibrotactile electromagnetic solenoid-type stimulator, with a shape that allows it to be attached to the skin with adhesive rings. The Tactor measures 18 mm in diameter and 12 mm in height, and its end-effector 2 mm in diameter by 3.5 mm in height. Its frequency range is 0

to 300 Hz, with a maximum displacement of 3.5 mm when driven at 12 Vpp [15]. The tactor is driven by a Dancer Design Amplifier. The amplifier attenuates the input signal from 10 Vpp to 6 Vpp, and shifts the phase by 172.8 degrees. This performance can be observed in Figure 6.5, where the input signal corresponds to 10 Vpp at 50 Hz shown in channel 2 (blue), and the output of the amplifier corresponds to 6 Vpp shown in channel 1 (orange).

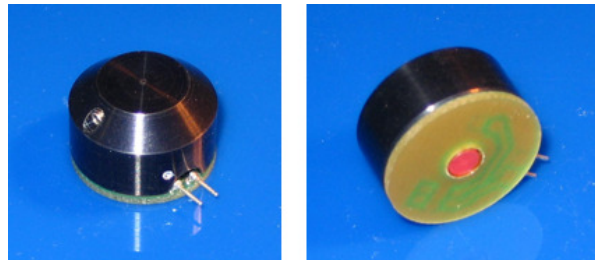


Figure 6.4: Dancer Design Tactor (mechanical stimulator). Taken from [15], used with the author's permission.

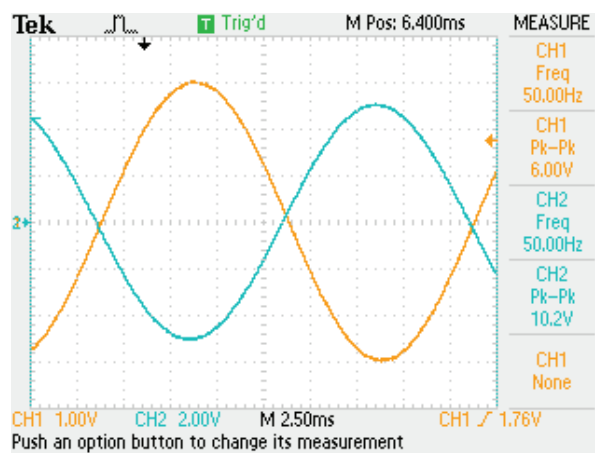


Figure 6.5: Design Dancer Amplifier output voltage when using an input signal of 10 Vpp at 50 Hz. Channel 1 (orange) corresponds to the output and channel 2 (blue) to the input signal.

### 6.1.2 Hardware Characterisation

Two different MS systems (Brüel & Kjør Minishaker and Dancer Design Tactor) were characterised in order to decide which of them was the most appropriate to use during the psychophysical tests, comparing the perceived tactile sensations resulting from the MS and the ES systems. Both mechanical systems comprise an amplifier and a vibrotactile stimulator. For both cases, the input (driving) signal was a sine wave generated by an Arduino Due DAC unit, and fed to the amplifiers.

The first step was to use a driving signal of 10 Vpp (peak-to-peak voltage) for a frequency sweep within the range of [2,300] Hz, measuring the output voltage of both amplifiers. Since the

amplitude of the output voltage decreased as the frequency of the input signal was increased, the amplitude of the input signal had to increase to compensate the drop at the output. Therefore, two compensation tables (one per amplifier) were hard-coded in the Arduino Due, which allowed it to modify the amplitude of the sine wave in order to ensure a constant output voltage of 10 Vpp for all tested frequencies in both amplifiers. The input signal with each frequency value was presented for three seconds, followed by one second where no signal was fed into the amplifier, ensuring that the measured position of the stimulators would reset before each frequency value was tested.

Using the constant 10 Vpp output, the displacement of both stimulators was estimated using a frequency sweep within the range of [2,300] Hz. The displacement was measured with a Keyence laser displacement sensor. The laser was connected to a Multifunction DAQ NI USB-6002, which was used to acquire the data and send the digital values to Matlab.

After testing both stimulators by placing a participant's finger on top of them, it was noted that the Minishaker stimulation resulted in the vibration of not only the finger, but the whole arm, regardless of the position or surface where the arm was resting on. Since the Tactor was able to produce a more localised stimulation; i.e., with less intensity than the Minishaker and without producing any vibrating movement on the participant's arm, this stimulator was chosen to run the new set of psychophysical experiments.

The force produced by the displacement of the Tactor was measured using a force load cell of 20 N during a frequency sweep within the range of [2,300] Hz with a 10 Vpp sine wave. Similar to the laser, the load cell was connected to a Multifunction DAQ NI USB-6002 to feed the measured force values to Matlab. The input signal with each frequency value was presented for three seconds, followed by one second where no signal was fed into the amplifier. Three cases where the contact between the end-effector of the Tactor and the load cell was different were analysed to compare the resulting force. The first case involved a 1 mm gap between the end-effector and the load cell, measuring the force only when the end-effector would displace and make contact with it. The second case regarded the load cell finely touching the end-effector and the third case regarded the load cell making full contact with the end-effector and the base of the Tactor.

### **6.1.3 Method of Triads**

The method of triads is a psychophysical procedure that uses judgement of relative perceived similarity or dissimilarity [48]. In this method, the participants are asked to decide which of two stimuli (comparison stimuli) is more similar to a third one (reference stimulus); i.e., the participant is asked to choose either "one" or "two". The term "similar" is meant to be vague because neither the experimenter nor the participant are able to verbalise what it specifically refers to; i.e., there is no precise idea regarding what psychological similarity can mean in terms of physical properties of the presented stimuli [60].

As mentioned in chapter 5, 10 optimum matched mechanical and electrical stimuli pairs were



selected to study further through the method of triads. The same five participants who took part in the previous rounds of psychophysical experiments (chapter 4) were chosen to take part in the method of triads. The 10 stimuli are listed in table 6.1, where the first five were modelled to activate a shallower fibre (or SA1), thus corresponding to the matching of the sets  $MS_{SA1}$  to  $ES_s$ ; whilst the last five were modelled to activate a deeper fibre (or PC), corresponding to the matching of the sets  $MS_{PC}$  to  $ES_d$  (marked in red in tables 5.7 and 5.8, respectively).

**Table 6.1: Parameters of the selected pairs of mechanical and electrical stimuli to use in the method of triads.**

Mechanical stimulus		Electrical stimulus								
$f$ / Hz	$A$ / $\mu\text{m}$	$f$ / Hz	$I_{el,1}$	$I_{el,2}$	$I_{el,3}$	$I_{el,4}$	$I_{el,5}$	$I_{el,6}$	$I_{el,7}$	$I_{el,8}$
18	140	16	0.06	-0.07	-0.05	0.05	-0.08	0.04	0.07	-0.02
45	351	39	-0.76	-0.54	0.37	0.75	0.55	-0.62	0.69	-0.45
27	211	32	-0.14	-1.69	1.63	1.16	0.69	-0.81	1.05	-1.90
25	195	156	-1.36	1.18	-1.28	1.55	-0.24	0.74	-0.30	-0.29
31	242	29	-0.15	0.01	0.09	0.01	0.05	0.01	0.01	-0.01
64	13	97	-1.31	1.01	-0.68	-0.56	1.10	2.16	-1.10	-0.63
47	18	40	-0.29	0.37	0.18	0.33	-0.07	-0.45	0.29	-0.35
77	10	104	0.02	-0.59	-0.33	1.16	0.68	-0.04	-0.66	-0.25
73	11	128	-0.29	0.38	-0.03	-0.11	0.32	0.33	-0.27	-0.33
54	16	108	0.22	1.08	-1.01	0.22	-0.49	0.80	-0.71	-0.11

The experiment was divided into 10 trials, where each trial comprised 25 triads. Each triad comprises one mechanical stimulus (reference stimulus) and two electrical stimuli (comparison stimuli). The 250 triads were under the condition that one of the comparison stimuli had to belong to the same class; i.e., either targeting a shallower fibre (stimulus labelled  $S_{SA1}$ ), or targeting a deeper fibre (stimulus labelled  $S_{PC}$ ); and the other comparison stimulus had to belong to the opposite class. The 25 triads per trial were randomly selected from the 250 without replacement. The order of presentation of the stimuli per triad was first the mechanical stimulus followed by the two electrical. Each stimulus was presented for one second, the interstimulus interval was fixed to one second and the interval between each triad to five seconds, therefore giving a total of 250 seconds per trial. All stimuli had a 50% duty cycle. All participants used the index fingers from both hands during this experiment. The index finger from the non-dominant hand was placed on the Tactor, whilst the index finger from their dominant hand was placed on the eight electrode array. At the beginning of each trial, the fingertip and the electrode array were cleaned with isopropyl alcohol.

The sets of 25 triads per trial were generated using Matlab, then sent to the Arduino Due Master (through serial communication) and finally to each of the Arduino Due Slaves (using I<sup>2</sup>C). Four Arduino Due Slaves controlled the electrical stimulation (as described in chapter 3), and a fifth Arduino Due Slave controlled the mechanical system (generating the corresponding sine wave and feeding it to the Dancer Design Amplifier).

## 6.2 Results

### 6.2.1 Hardware Characterisation

#### 6.2.1.1 Brüel & Kjær Minishaker

The displacement of the Minishaker proved to have its maximum amplitude at 2 Hz, followed by a somewhat constant amplitude until 40 Hz to then decrease as the frequency increased, as observed in the Bode diagram in Figure 6.6. The Bode diagram was computed in Matlab using a plant estimation from the obtained displacement readings (with the Matlab functions ‘iddata’ and ‘tfest’). The chosen plant ( $P_M$ ) representing the Minishaker was:

$$(6.1) \quad P_M = \frac{11.58s^2 - 7808s + 9.734e^4}{s^3 + 156.5s^2 + 5.782e^4s + 8.006e^4}.$$

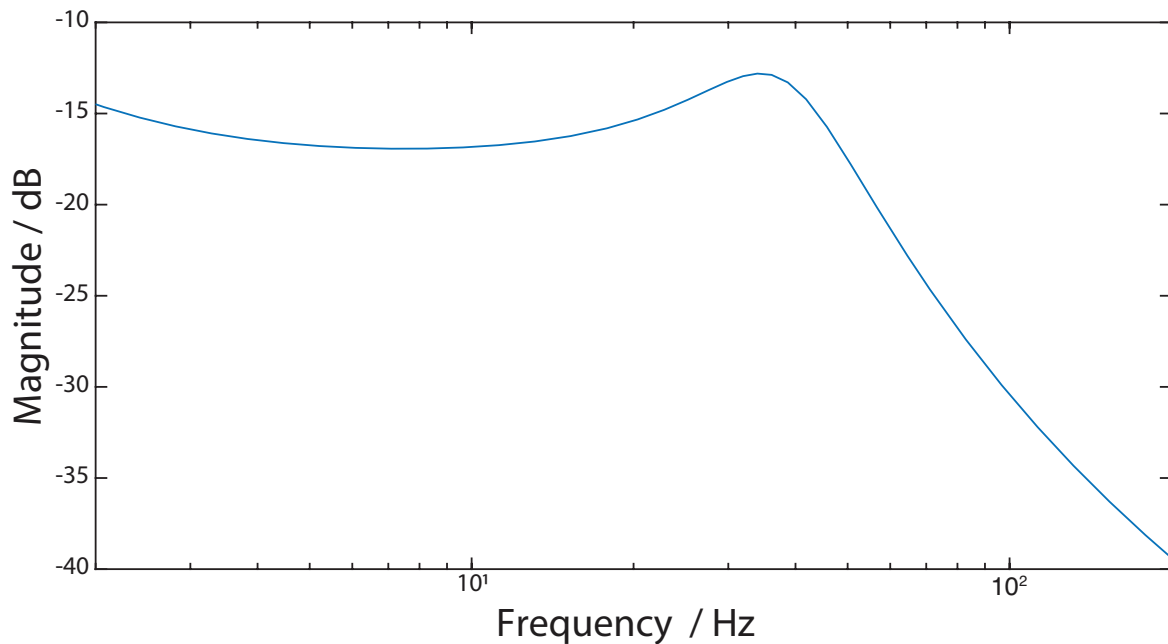


Figure 6.6: Bode diagram for the displacement of the Minishaker using a frequency sweep of [2, 200] Hz.

#### 6.2.1.2 Dancer Design Tactor

The tracking of the displacement of the Tactor is illustrated as a Bode diagram in Figure 6.7, where it can be seen that it is somewhat constant until 20 Hz. The displacement peaks around two frequencies: 55 and 105 Hz, reaching the documented maximum amplitude of -1 to 3.5 mm. Furthermore, the displacement drastically drops after 125 Hz. The Bode diagram was computed

in Matlab using a plant estimation from the obtained displacement readings (with the Matlab functions 'iddata' and 'tfest'). The chosen plant ( $P_T$ ) describing the Tactor was:

$$(6.2) \quad P_T = \frac{-70.23s^4 - 590.9s^3 - 3.048e07s^2 - 6.4e^9s + 3.049e^{11}}{s^5 + 352.2s^4 + 6.008e^5s^3 + 1.384e^8s^2 + 5.988e^{10}s + 1.13e^{11}}.$$

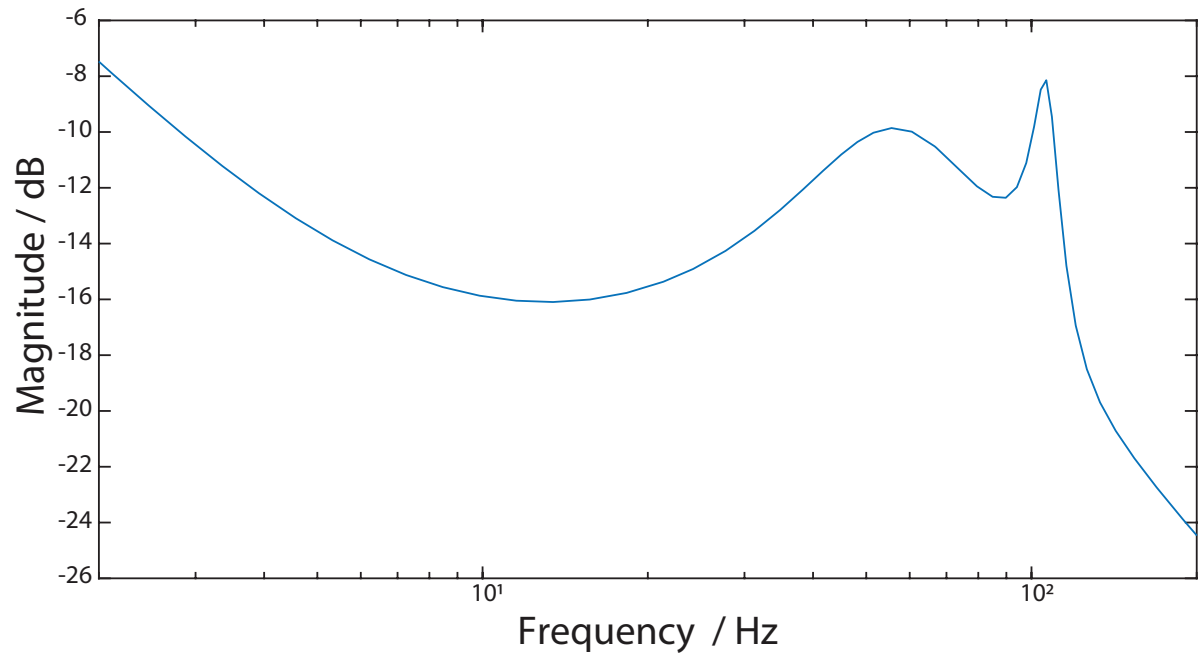


Figure 6.7: Bode diagram for the displacement of the Tactor using a frequency sweep of [2, 200] Hz.

The results obtained from all three cases evaluating the force produced by the end-effector when the load cell was set at different locations (thus changing the contact area with the end-effector of the Tactor), are shown in Figure 6.8. The data in blue corresponds to the first case, where a 1 mm gap was set between the load cell and the end-effector. Similarly, the data in green corresponds to the second case, where the load cell was lightly touching the end-effector; and the data in red corresponds to the third case, where the load cell was fully making contact with the base of the Tactor and the end-effector.

It is noted that regarding the first case, the resulting force peaks around 50 and 140 Hz, to then dramatically drop after 145 Hz. On the other hand, the force measured in the second case peaks around 125 Hz, to then stay somewhat constant throughout the rest of the frequencies. The last case shows that the produced force peaks around 105 Hz, approximating to the maximum documented value of 0.35 N. During this third case, it is noted that the force does not change drastically throughout all the frequency sweep range, having a mean value of 0.22 N.

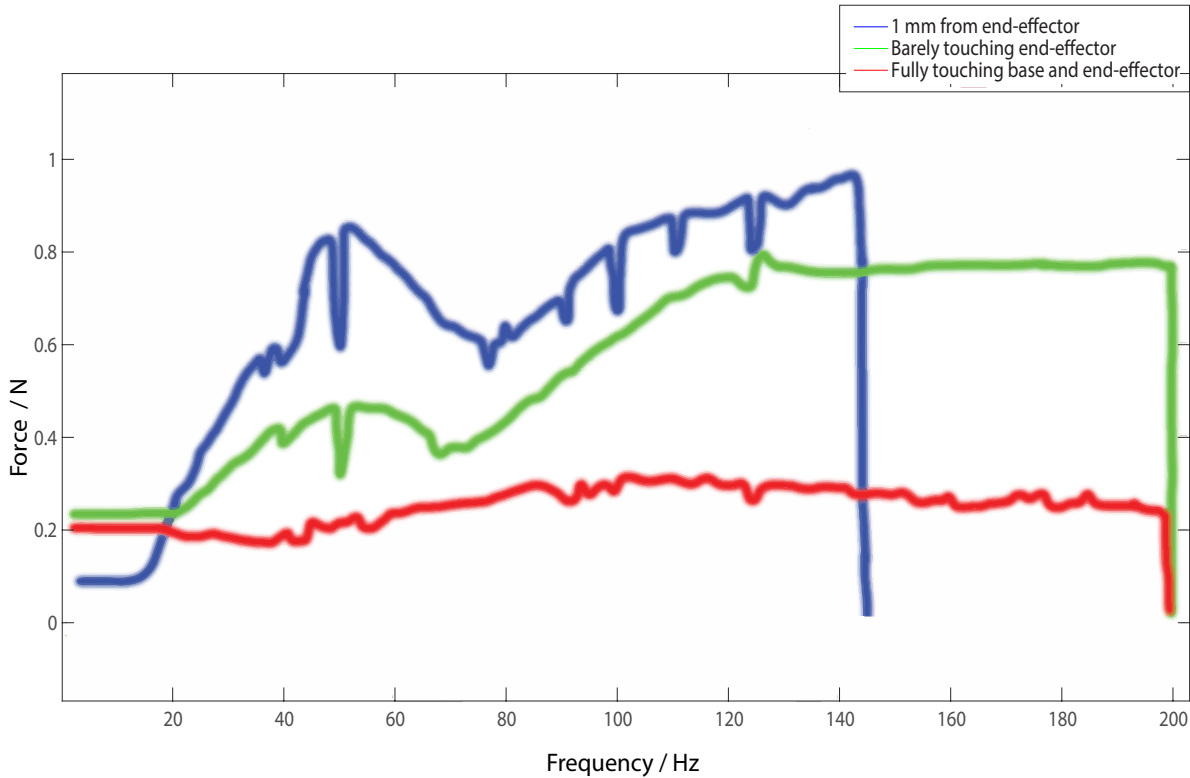


Figure 6.8: Measured forces of the Tactor using a frequency sweep of [2, 200] Hz. The data in blue corresponds to the measured force where there was a 1 mm gap between the load cell and the end-effector of the Tactor. The data in green represents the case where the load cell was barely making contact with the end-effector, and the data in red corresponds to when the load cell was fully making contact with all the end-effector and base of the Tactor.

## 6.2.2 Method of Triads

### 6.2.2.1 Discrimination Between Stimuli Classes

The discrimination between classes  $S_{SA}$  and  $S_{PC}$  was evaluated defining the triads as listed on tables 6.2 and 6.3. Class  $S_{SA}$  involves the mechanical stimuli  $M_A$  to  $M_E$  (which correspond to the first five mechanical stimuli listed on table 6.1), as well as the electrical stimuli  $E_A$  to  $E_E$  (matched to the mechanical  $M_A$  to  $M_E$ , respectively). Similarly, class  $S_{PC}$  involves the mechanical stimuli  $M_F$  to  $M_J$  (which correspond to the last five mechanical stimuli listed on table 6.1), as well as the electrical stimuli  $E_F$  to  $E_J$  (matched to the mechanical  $M_F$  to  $M_J$ , respectively).

The triads with answer "one" (where the first electrical stimulus corresponded to the same class as the mechanical stimulus, as depicted in Figure 6.9) are listed on table 6.2, whilst the ones with answer "two" (where the second electrical stimulus corresponded to the same class as the mechanical stimulus, as illustrated in Figure 6.10) are listed on table 6.3. The computed  $d'$ ,  $\beta$  and  $c$  of all five participants are presented on table 6.4.

The performances of the five participants on the discrimination between stimuli classes

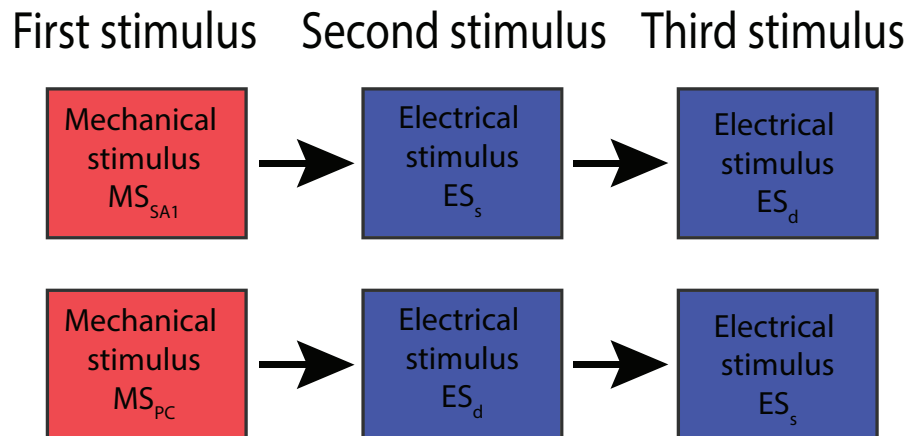


Figure 6.9: Triads where the correct discrimination is given by the participant answering "one", for the first ES corresponds to the same class as the MS firstly presented.

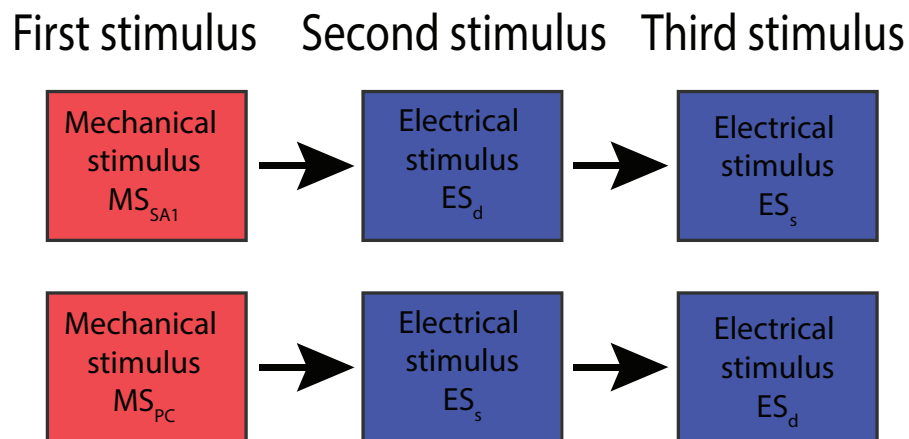


Figure 6.10: Triads where the correct discrimination is given by the participant answering "two", for the second ES corresponds to the same class as the MS firstly presented.

Table 6.2: **Triads with answer "one" for discrimination between stimuli classes.**

First stimulus	Second stimulus	Third stimulus
$M_A$	$E_{A,B,C,D,E}$	$E_{F,G,H,I,J}$
$M_B$	$E_{A,B,C,D,E}$	$E_{F,G,H,I,J}$
$M_C$	$E_{A,B,C,D,E}$	$E_{F,G,H,I,J}$
$M_D$	$E_{A,B,C,D,E}$	$E_{F,G,H,I,J}$
$M_E$	$E_{A,B,C,D,E}$	$E_{F,G,H,I,J}$
$M_F$	$E_{F,G,H,I,J}$	$E_{A,B,C,D,E}$
$M_G$	$E_{F,G,H,I,J}$	$E_{A,B,C,D,E}$
$M_H$	$E_{F,G,H,I,J}$	$E_{A,B,C,D,E}$
$M_I$	$E_{F,G,H,I,J}$	$E_{A,B,C,D,E}$
$M_J$	$E_{F,G,H,I,J}$	$E_{A,B,C,D,E}$

Table 6.3: Triads with answer "two" for discrimination between stimuli classes.

First stimulus	Second stimulus	Third stimulus
$M_A$	$E_{F,G,H,I,J}$	$E_{A,B,C,D,E}$
$M_B$	$E_{F,G,H,I,J}$	$E_{A,B,C,D,E}$
$M_C$	$E_{F,G,H,I,J}$	$E_{A,B,C,D,E}$
$M_D$	$E_{F,G,H,I,J}$	$E_{A,B,C,D,E}$
$M_E$	$E_{F,G,H,I,J}$	$E_{A,B,C,D,E}$
$M_F$	$E_{A,B,C,D,E}$	$E_{F,G,H,I,J}$
$M_G$	$E_{A,B,C,D,E}$	$E_{F,G,H,I,J}$
$M_H$	$E_{A,B,C,D,E}$	$E_{F,G,H,I,J}$
$M_I$	$E_{A,B,C,D,E}$	$E_{F,G,H,I,J}$
$M_J$	$E_{A,B,C,D,E}$	$E_{F,G,H,I,J}$

Table 6.4: Signal detection model parameters from discriminating between stimuli classes.

Participant	$d'$	$\beta$	$c$
$P_1$	1.425	1.110	0.073
$P_2$	0.654	0.996	-0.0067
$P_3$	0.306	1.023	0.074
$P_4$	0.411	1.024	0.058
$P_5$	1.108	1.054	0.048
Average	0.780	1.042	0.049

are depicted in panels (a), (c), (e), (g) and (i) in Figure 6.12, where each row corresponds to the probability density distributions of each participant. All corresponding plots and the estimated discrimination measures were computed using RscorePlus. The red markers represent the computed decision criterion ( $c_a$ ) and its standard error in each panel. According to the results listed on table 6.4, it can be observed that participant  $P_1$  presented the best performance when discriminating between stimuli classes  $S_{SA1}$  and  $S_{PC}$ . In average, all participants show a conservative decision.

The breakdown of the responses of  $P_1$ , who obtained the best performance when discriminating between stimuli classes, are shown in Figure 6.11. It is illustrated that a large amount of hits lead to a high performance.

### 6.2.2.2 Discrimination of True Stimuli Pairs

The discrimination of true stimuli pairs; i.e., where the reference is identical to one of the comparison stimuli, was evaluated defining the triads as listed on tables 6.5 and 6.6. The triads with answer "one" corresponded to the triplets listed on table 6.2, whilst the ones with answer "two" corresponded to the list of triplets listed on table 6.3. The computed  $d'$ ,  $\beta$  and  $c$  of all five participants are presented on table 6.7.

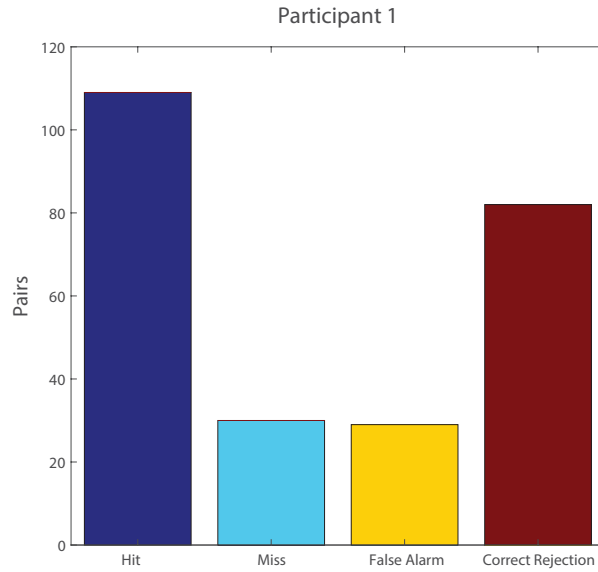


Figure 6.11: Number of hits, misses, false alarms and correct rejections of  $P_1$ , with the best performance of the five participants when discriminating between stimuli classes.

Table 6.5: "One" triads for discrimination of true stimuli pairs.

First stimulus	Second stimulus	Third stimulus
$M_A$	$E_A$	$E_{F,G,H,I,J}$
$M_B$	$E_B$	$E_{F,G,H,I,J}$
$M_C$	$E_C$	$E_{F,G,H,I,J}$
$M_D$	$E_D$	$E_{F,G,H,I,J}$
$M_E$	$E_E$	$E_{F,G,H,I,J}$
$M_F$	$E_F$	$E_{A,B,C,D,E}$
$M_G$	$E_G$	$E_{A,B,C,D,E}$
$M_H$	$E_H$	$E_{A,B,C,D,E}$
$M_I$	$E_I$	$E_{A,B,C,D,E}$
$M_J$	$E_J$	$E_{A,B,C,D,E}$

Panels (b), (d), (f), (h) and (j) in Figure 6.12 illustrate the probability density distributions corresponding to the performance of the participant during the discrimination of true stimuli pairs. Each row describes the individual performance of all five participants. The red markers represent the computed decision criterion ( $c_d$ ) and its standard error in each panel. The results listed on table 6.7 show that participant  $P_5$  had the best performance while being the most liberal of all five. It is also noted that participant  $P_4$  had the poorest performance, showing that they could not distinguish the true stimulus pairs when presented within triads. Overall, all participants show a liberal decision; i.e., when little evidence of the signal is needed in order to make a decision regarding whether the signal was presented or not.

The breakdown of the responses of  $P_5$ , who presented the best performance when discriminating the true stimuli pairs, are shown in Figure 6.13. It is illustrated that a large amount of

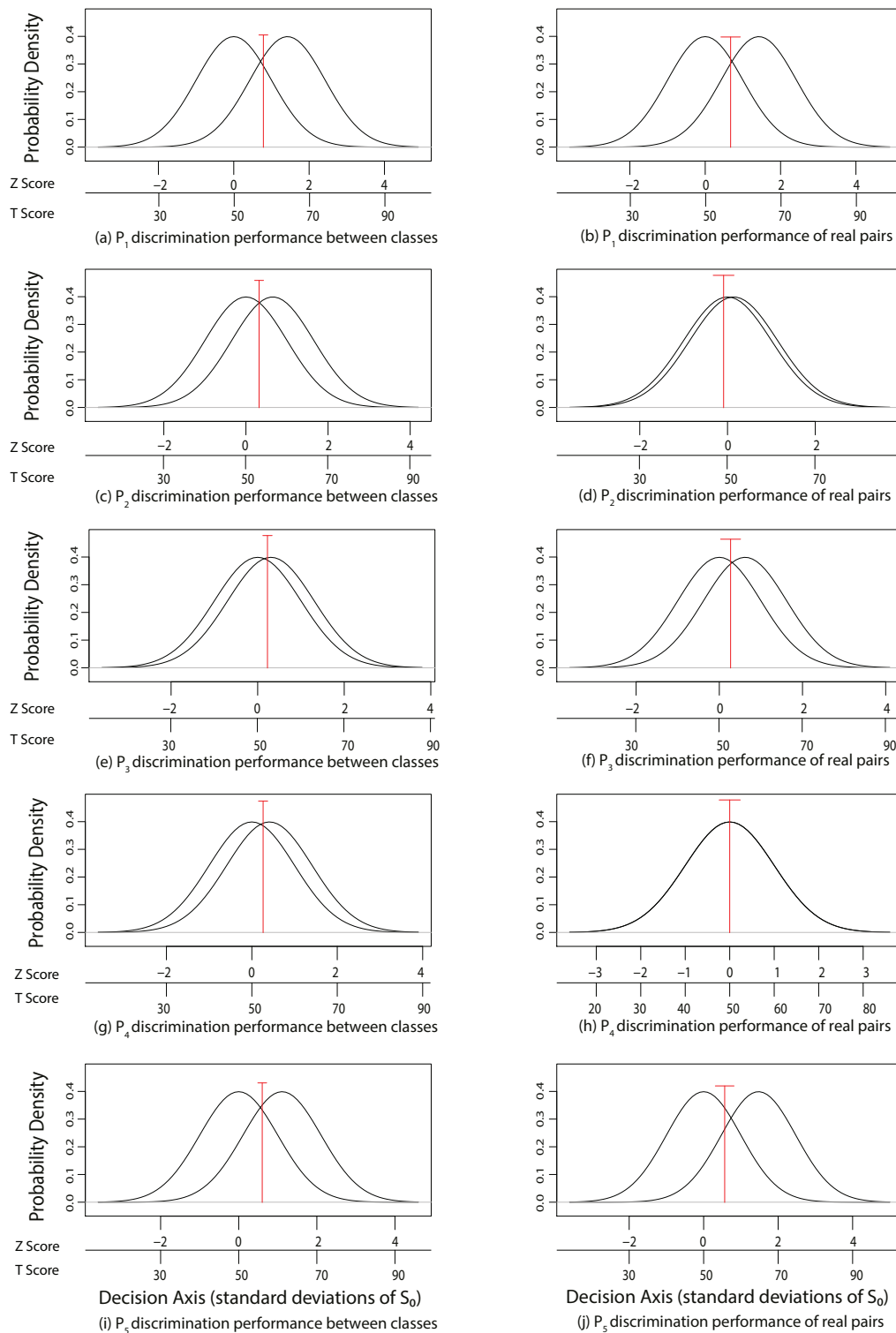


Figure 6.12: Probability density distributions of the discrimination performances between stimuli classes and of true stimuli pairs of the five participants ( $P_1$  to  $P_5$ ). Panels (a), (c), (e), (g) and (i) correspond to the responses of  $P_1$  to  $P_5$  regarding the comparison between stimuli classes. Panels (b), (d), (f), (h) and (j) represent the responses of  $P_1$  to  $P_5$  when comparing true stimuli pairs. All computed decision criteria ( $c_a$ ) and their standard errors are marked in red in each panel. The corresponding T score values to the Z score values are shown in each panel.



Table 6.6: "Two" triads for discrimination of true stimuli pairs.

First stimulus	Second stimulus	Third stimulus
$M_A$	$E_{F,G,H,I,J}$	$E_A$
$M_B$	$E_{F,G,H,I,J}$	$E_B$
$M_C$	$E_{F,G,H,I,J}$	$E_C$
$M_D$	$E_{F,G,H,I,J}$	$E_D$
$M_E$	$E_{F,G,H,I,J}$	$E_E$
$M_F$	$E_{A,B,C,D,E}$	$E_F$
$M_G$	$E_{A,B,C,D,E}$	$E_G$
$M_H$	$E_{A,B,C,D,E}$	$E_H$
$M_I$	$E_{A,B,C,D,E}$	$E_I$
$M_J$	$E_{A,B,C,D,E}$	$E_J$

Table 6.7: Signal detection model parameters from discriminating the true stimuli pairs.

Participant	$d'$	$\beta$	$c$
$P_1$	1.422	0.950	0.073
$P_2$	0.140	0.978	-0.159
$P_3$	0.620	0.976	-0.039
$P_4$	0	1	0
$P_5$	1.474	0.776	-0.172
Average	0.731	0.936	-0.102

hits and correct rejections lead to a high performance.

The added performance of all five participants is observed in Figure 6.14. Panel (a) corresponds to the discrimination between stimuli classes task and panel (b) to the discrimination of true stimuli pairs. It is shown that the difference between those added performances is minimum, presenting no evident pattern.

### 6.3 Discussion

The Minishaker showed variations in its displacement as the frequency sweep was presented, but these changes were not as drastic as the ones observed with the Tactor. Nevertheless, as previously mentioned, the Minishaker was discarded for the psychophysical experiments (method of triads). This decision was taken when it was observed that the Minishaker would induce vibration of the whole hand and arm of the participants. The Tactor was chosen as the mechanical stimulator to use in the experiments because its shape allows the stimulation to be perceived as finely localised (on the fingertip only), similar to the effect of the electrical stimulation using the eight electrode array.

Since it was foreseen that the displacement of the Tactor would be damped by the participants' fingertips, it was noted that this parameter could not be directly matched to the modelled

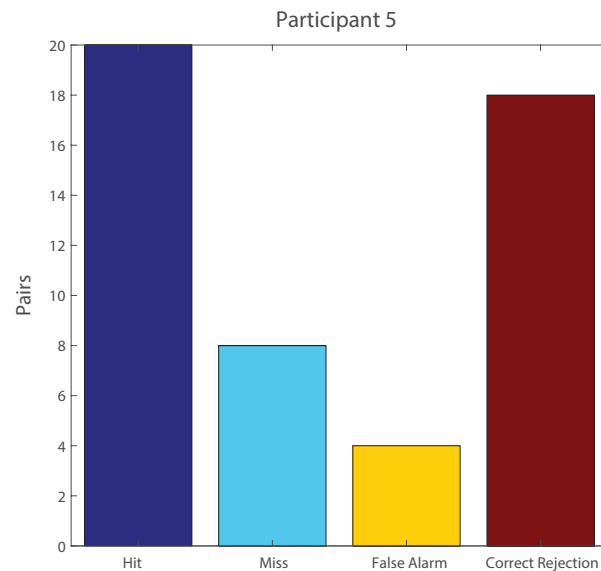


Figure 6.13: Number of hits, misses, false alarms and correct rejections of  $P_5$ , with the best performance of the five participants when discriminating between true stimuli pairs.

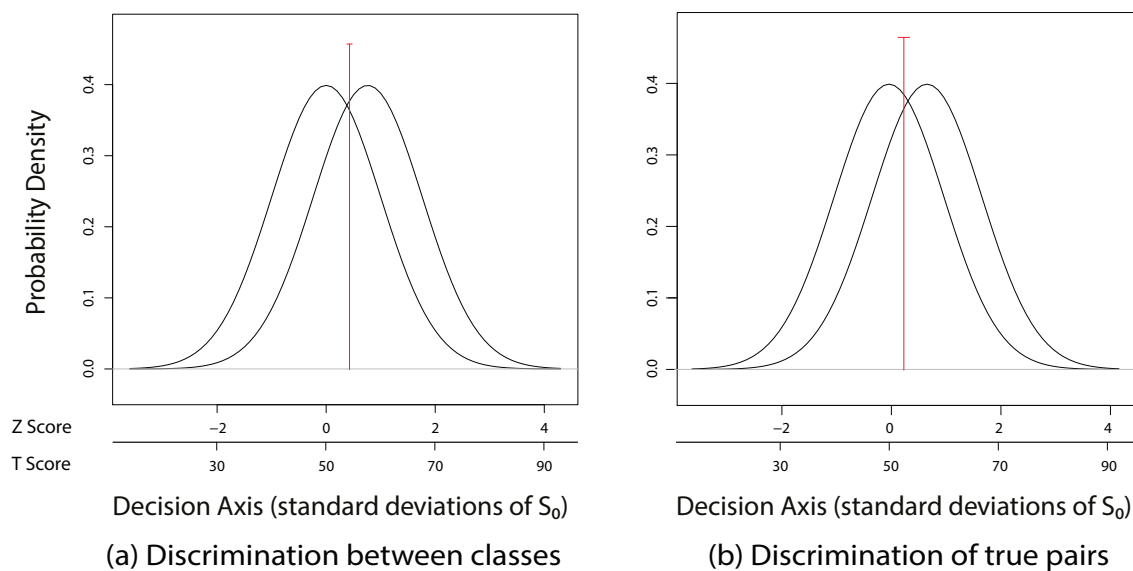


Figure 6.14: Probability density distributions of the added discrimination performances using the method of triads of the five participants ( $P_1$  to  $P_5$ ). Panel (a) illustrates the discrimination between stimuli classes and panel (b) the discrimination of true stimuli pairs. All computed decision criteria ( $c_a$ ) and their standard errors are marked in red in each panel. The corresponding T score values to the Z score values are shown in each panel.

amplitude of the mechanical stimuli presented in chapter 5. Therefore, the force produced by the Tactor was analysed to verify its relation to the amplitude of the input signal (fed to the amplifier). The first setting to measure the force (with the 1 mm gap between the load cell and the end-effector of the Tactor) showed a significant drop after 145 Hz; this effect was expected since the displacement has decreased, leading to the end-effector not reaching the load cell. In this test, the load cell essentially recorded essentially impacts from the Tactor.

The first and second cases (data in blue and green in Figure 6.8) showed that the produced force followed the shape of the displacement. This was also expected, for the location of the load cell with respect to the Tactor (either not touching or barely touching the end-effector) lead to the measured force to be directly dependent on the displacement. On the contrary, the third case served as a realistic representation of how the fingertips of the participants would make contact with the Tactor, showing that the resulting force was directly dependent on the amplitude of the input signal (fed to the amplifier and previously modelled in chapter 5).

Regarding the psychophysical experiments presented in this chapter, it was observed that there is no general pattern of results throughout both discriminations (i.e., between classes and of the true stimuli pairs). Participants  $P_3$  and  $P_5$  showed a better individual performance during the discrimination of the true stimuli pairs, while participants  $P_1$  and  $P_2$  had better results at discriminating between stimuli classes  $S_{MS}$  and  $S_{PC}$ . On average, the discrimination between stimuli classes was conservative (where more evidence of the signal is needed in order to decide whether it was presented on the pair of stimuli or not), whilst the discrimination of true stimuli pairs was liberal (as shown in tables 6.4 and 6.7). It can be observed that participants  $P_1$  and  $P_5$  can discriminate between stimuli classes and true pairs of stimuli, which suggests that the tactile sensations produced by both mechanical and electrical are somewhat similar between stimuli of the same class and between the stimuli pairs, where the modelled mechanical stimulus (reference) is identical to one of the modelled electrical stimuli (comparison stimuli).

## 6.4 Conclusion

The results from the psychophysical experiments in this chapter demonstrate that it is possible to perceive similarities between mechanical stimuli given by the Tactor and electrical stimuli given by the TENS system (presented in chapter 3), allowing the participants to correctly discriminate between stimuli classes (one targeting a shallower fibre and another targeting a deeper fibre) and to discriminate pairs of stimuli (one mechanical and one electrical) previously modelled and optimised in chapter 5. It is also observed that not every participant has the same ability to differentiate between stimuli classes and true pairs of stimuli, since their perception of the resulting tactile sensations varies individually. The Tactor proved to be a valuable mechanical stimulation system to compare the perceived tactile sensations produced by the previously mentioned TENS system, both matching in size and in producing perceived finely localised

sensations.



## CONCLUSIONS

The aim of this project is to develop a TENS system for a human finger and compare it to a mechanical stimulation system in both a simulated environment and through psychophysical tests (using the respective hardware implementations) to evaluate the similarity of the resulting tactile sensations. It was observed that the selective stimulation of fibres located at different depths is directly dependent on the TENS design, particularly on the excitation patterns given by the individual electrode currents, which has not been documented in literature.

The simulation environment presented in chapter 2, allowed the design of particular electrical stimulation patterns for an eight electrode array. These stimuli belonged to two classes, one designed to selectively stimulate a shallower fibre (representing one SA1 fibre) and the other designed to selectively stimulate a deeper fibre (representing one PC fibre). The stimuli were tested (documented in chapter 4) using the hardware implementation of the TENS system (described in chapter 3), resulting in the participants showing a better performance in the psychophysical tests when discriminating between classes than within classes in two of the three tested frequencies (10 and 50 Hz). This shows that different tactile sensations were perceived when using the designed classes of stimuli.

Taking into account that the perceived sensations and action potentials resulting from mechanical stimuli have been meticulously documented in literature, a known mechanical stimulation model [16] was implemented to compare its output with that obtained from the developed TENS simulation environment (presented in chapter 5). The aim was to minimise the difference between both spike trains, thus optimising the frequency and amplitude of the monophasic square pulse excitation signal of the modelled TENS system, using the GVP distance implemented in a genetic algorithm. This led to the development of two optimised sets of electrical stimuli matched to known mechanical stimuli (that selectively stimulated one SA1 and a PC

fibre), which were further used in a second round of psychophysical tests to compare the perceived tactile sensations between a mechanical stimulator and the TENS system. The results showed that there was no evident pattern in the results of all participants. Nevertheless, it was also observed that it was possible to perceive certain similarities between the tactile sensations produced by the mechanical system and those resulting from the electrical system (presented in chapter 6); this was indicated through the ability of some of the participants to discriminate between classes of stimuli and to differentiate when the optimised pair (designed electrical stimulus to match the response obtained from a specific mechanical stimulus) was presented.

Therefore, all particular aims for the project were met, from building the simulation environment representing a multi-layered human finger tissue with the electrode array for ES, integrating the respective ES hardware, implementing and comparing the TENS system to a MS system in a simulation environment and running psychophysical tests to study the similarity between the tactile sensations produced by both mechanical and electrical stimulation systems.

## 7.1 Future Work

The finger FEM developed for this work does not consider the capacitive and dielectric properties of the skin, fat, bone and the electrode system. Future versions of the simulation environment may include these aspects, which would improve the modelling of transients and other high-frequency effects. This would be useful for investigating the effect of frequency and width of the current pulses, but such an implementation would require data on the electrical properties of a real human finger that are at present unavailable. The environment could also be improved by including variable electrode geometries in the FEM, instead of having the eight linear electrodes as the current design, allowing electrode shape to be included when optimising the design of the array. Regarding the improvement of the nerve-fibre model, a non-linear double cable model [54] could be implemented to provide a more realistic nerve response. However, this would involve a higher computational cost because the number of sections in which the fibre is divided would be tripled, due to consideration of the paranodal and internodal sections of the fibre. This increased computational cost could be addressed by running the simulation environment for less than one second or allowing Matlab to use more memory in the computer where the environment is run. The environment could also be coded in a different language, aiming to speed up the computation of the results.

Different saturation tests (with variable setups) could also be performed using more participants to search for possible patterns that could help explain this effect in detail when using specific electrical stimuli. This would allow a better understanding of the relation between the duration of the electrical stimulation and the comfortable perception of the resulting sensation. Nevertheless, it should be considered that it is possible for these tests to require a long time to run. The skin impedance of the fingertip could also be measured before each test in order to

investigate the relation between this parameter and the fibres saturation when using electrical stimuli (e.g., using two golden electrodes testing the human skin in water solutions of KCl). Another alternative could involve the implementation of microneedle arrays to neglect the influence of the stratum corneum on the skin impedance and allowing a more stable contact between the fingertip and the electrode array [10].

One of the main limitations of the current setup of the experiments was the limited number of participants who presented constant values for the amplitude ranges of the electrical stimuli when running the calibration test throughout different days. As previously discussed, this finding was thought to be related to nerve saturation. Microneedle arrays could also be used to allow a more localised and controlled effect on specific nerves when using electrical stimulation than surface electrodes. Similarly, microneedle arrays could also be implemented for signal recording (specific nerve activity resulting from the electrical stimulation) as a minimally invasive technique, as documented by Chen et al. [10], to complement the results obtained from the psychophysical tests.

Regarding the TENS hardware implementation, the design could be improved by scaling down the size of the hardware (mainly using smaller transistors), thus allowing it to be more portable. Similarly, a better fan could be used, replacing the current three and providing a better airflow. Furthermore, different electrode shapes and sizes could be tested, as well as materials for the electrodes (e.g., flexible electrodes) to develop multiple prototypes to include this type of haptic feedback in teleoperation or virtual reality systems, introducing the described selective stimulation. The main challenge the electrical stimulation used for tactile sensations presents is the proper calibration for each user, for the currents have to be finely controlled not to produce uncomfortable sensations. Further work could investigate the possibility of including a constant measurement of the skin impedance while using the TENS system, in order to provide a feedback to control the amplitude of the current pulse (thus adapting the system to the changes in the skin capacitive properties), or using either the aforementioned microneedle arrays or implanted electrodes that penetrate the skin.

In summary, the work presented in this thesis introduced a system that can provide selective stimulation of fibres located at different depths using electrical stimulation. This is observed in both the simulation environment and the hardware implementation. This principle has the potential to be used in teleoperation systems, providing haptic feedback through a system characterised by its simple hardware design (e.g., adding electrodes to a glove to have more than one contact points with the skin and produce diverse tactile sensations). It was also noted that the tactile sensations produced by the electrical stimulation system were not equal to those resulting from mechanical stimulation (for there was no evident pattern found through the psychophysical tests); however, the potential users could be trained to associate the tactile sensations from the TENS system to certain information (e.g., coupling electrical stimulation with visual information) in order to be able to have a better performance while discriminating between electrical stimuli.







## HARDWARE SCHEMATICS AND ETHICAL APPROVAL

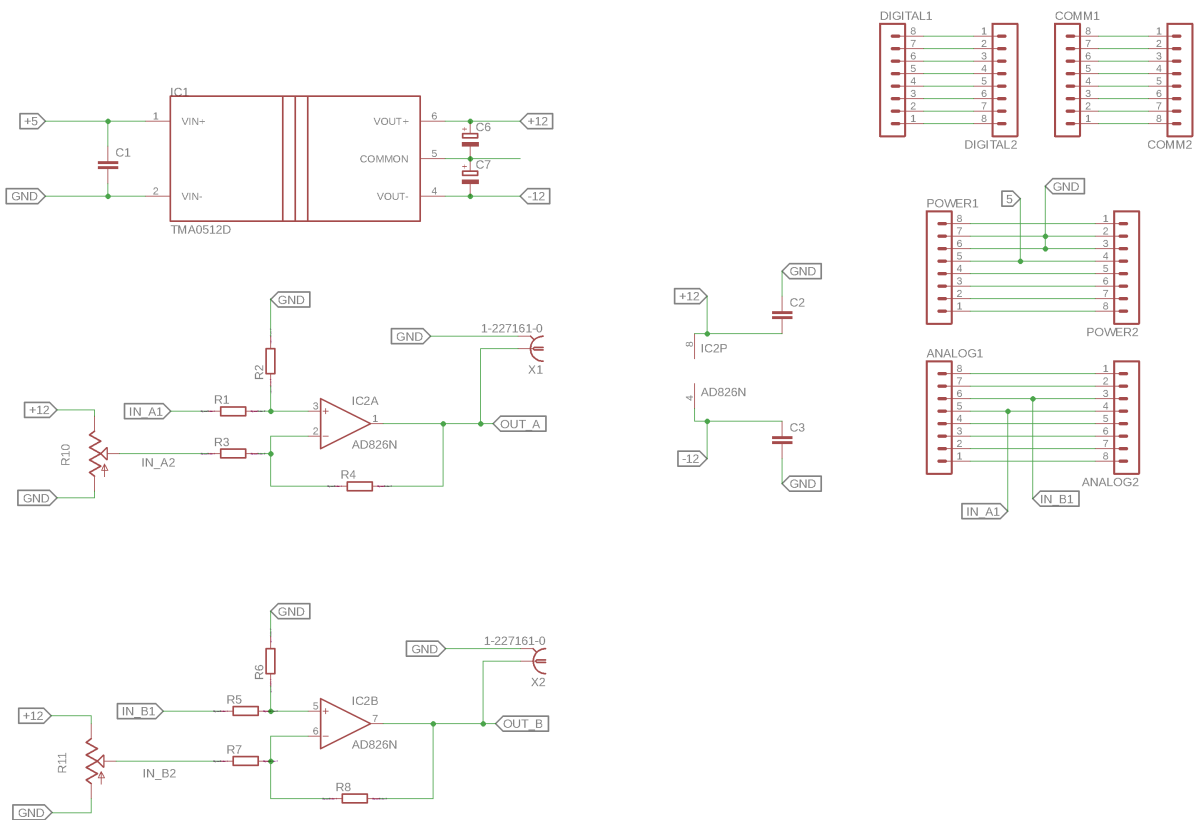


Figure A.1: Full schematic of the DAC circuit board.

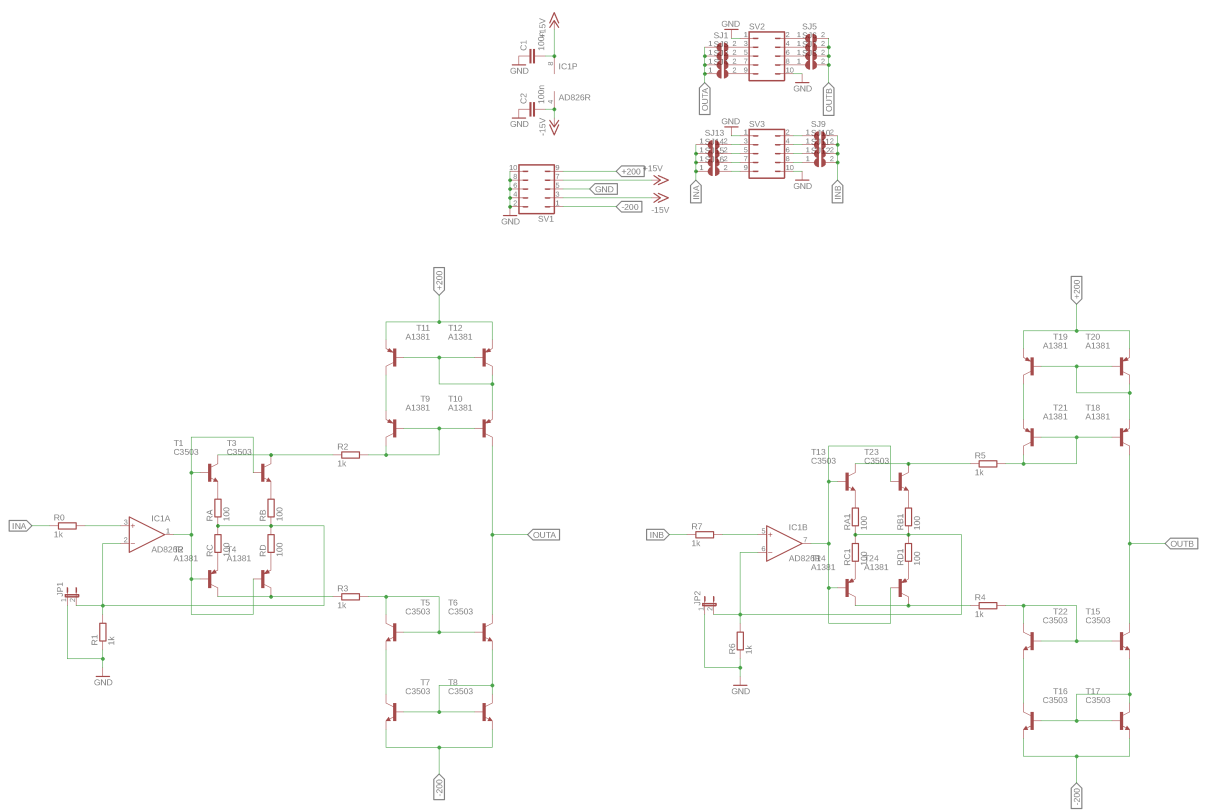


Figure A.2: Full schematic of the VI converter circuit board.

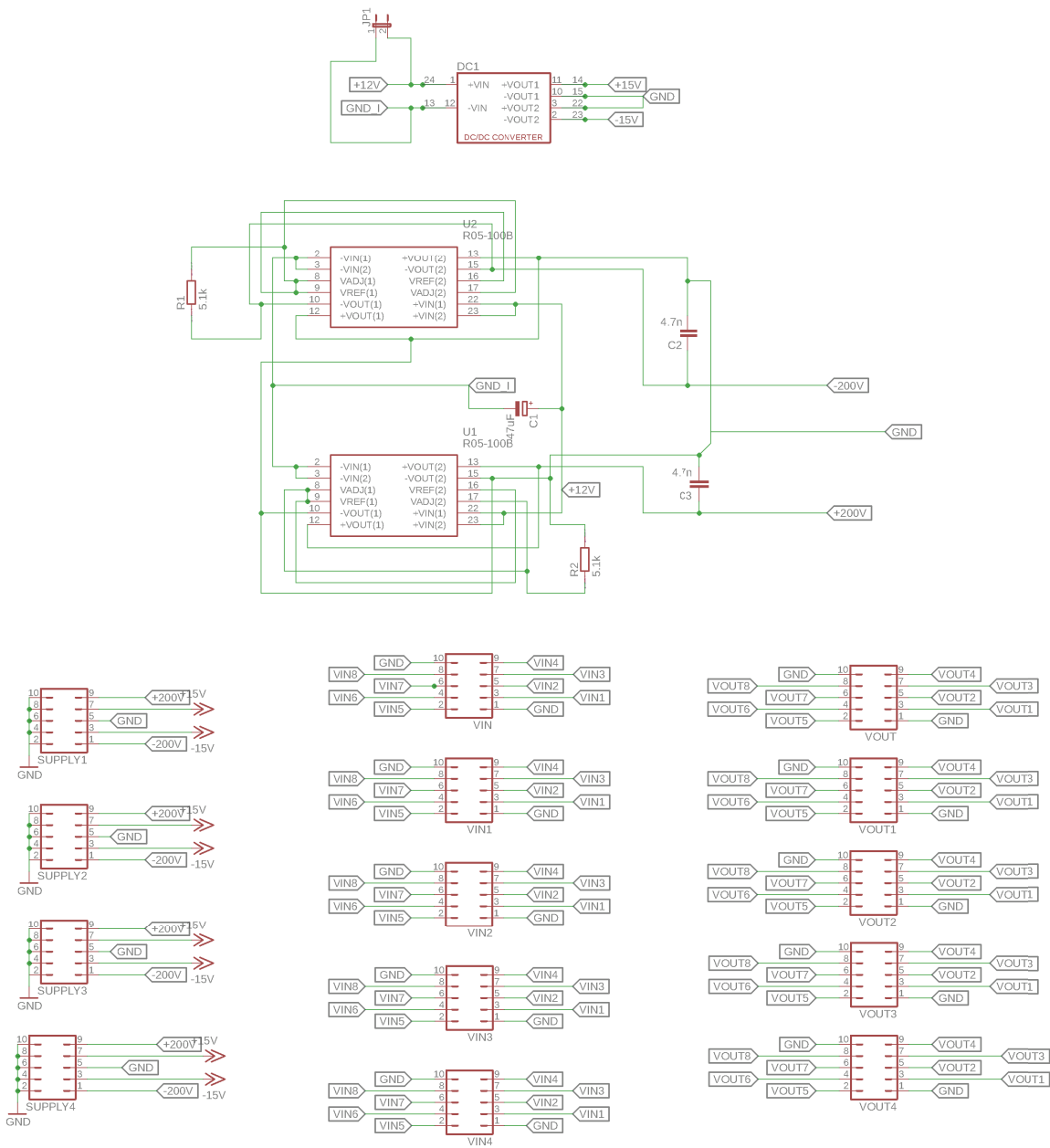


Figure A.3: Full schematic of the power supply circuit board.

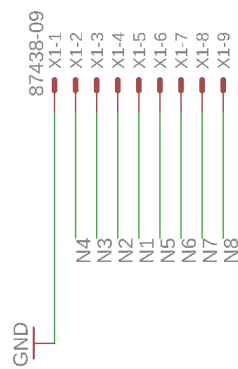


Figure A.4: Full schematic of the electrode array.

University of  
BRISTOL

Research and Enterprise Development

[RED home](#) | [About RED](#) | [Contact RED](#) | [People](#) | [Events](#)

RED [Logout](#)

University home > RED > [Ethics On-line Tool](#) > Archived or 'signed off' applications

### 🔍 Archived or 'signed off' applications

---

**Add a new application**

Show/hide search criteria

View open applications

Archived or 'signed off' applications.

▲ Project title ▼	▲ Submitter ▼	▲ On behalf of ▼	▲ Faculty ▼	▲ Department ▼	▲ Supervisor ▼	▲ Status ▼	☑
Model-based Transcutaneous Electrical Nerve Stimulation <a href="#">[update]</a> <a href="#">[comment]</a>	Gloria Araiza Illan		Faculty of Engineering	Aerospace Engineering	Jonathan Rossiter	Signed off	Yes

Users guides
[Submitter](#)
[Approver](#)
[Reviewer](#)
[Signatory](#)

Figure A.5: Logged ethical approval from the University of Bristol.

UWE REC REF No: FET.17.07.057

27 October 2017

Gloria Araiza Illan  
Research Bay 6,  
Bristol Robotics Lab,  
T Block,  
Frenchay Campus

Dear Gloria

**Application title: Model-based Transcutaneous Electrical Nerve Stimulation**

I am writing to confirm that the Faculty Research Ethics Committee are satisfied that you have addressed all the conditions relating to our previous letter sent on 3<sup>rd</sup> October 2017 and the study has been given ethical approval to proceed.

Please note that any information sheets and consent forms should have the UWE logo. Further guidance is available on the web: <https://intranet.uwe.ac.uk/tasks-guides/Guide/writing-and-creating-documents-in-the-uwe-bristol-brand>

The following standard conditions also apply to all research given ethical approval by a UWE Research Ethics Committee:

1. You must notify the relevant UWE Research Ethics Committee in advance if you wish to make significant amendments to the original application: these include any changes to the study protocol which have an ethical dimension. Please note that any changes approved by an external research ethics committee must also be communicated to the relevant UWE committee.  
<http://www1.uwe.ac.uk/research/researchethics/applyingforapproval.aspx>
2. You must notify the University Research Ethics Committee if you terminate your research before completion;
3. You must notify the University Research Ethics Committee if there are any serious events or developments in the research that have an ethical dimension.

Please note: The UREC is required to monitor and audit the ethical conduct of research involving human participants, data and tissue conducted by academic staff, students and researchers. Your project may be selected for audit from the research projects submitted to and approved by the UREC and its committees.

We wish you well with your research.

Yours sincerely

*Alistair Clark*

Dr Alistair Clark  
Chair, Faculty Research Ethics Committee

c.c. Prof. Angelika Peer





## REFERENCES

- [1] ADVANCED COMPUTING RESEARCH CENTRE, U. O. B.  
High performance computing (hpc), August 2015.
- [2] ARAIZA ILLAN, G., STÜBER, H., FRIEDL, K. E., SUMMERS, I. R., AND PEER, A.  
A simulation environment for studying transcutaneous electrotactile stimulation.  
*PLOS ONE* 14, 2 (2019), 1–30.
- [3] BROWN, E. N., KASS, R. E., AND MITRA, P. P.  
Multiple neural spike train data analysis: state-of-the-art and future challenges.  
*Nature Neuroscience* 7, 5 (2004), 456–461.
- [4] BUCHHOLZ, B., ARMSTRONG, T. J., AND GOLDSTEIN, S. A.  
Anthropometric data for describing the kinematics of the human hand.  
*Ergonomics* 35, 3 (1992), 261–273.  
PMID: 1572336.
- [5] BURYANOV, A., AND KOTIUK, V.  
Proportions of hand segments.  
*International Journal of Morphology* 28, 3 (2010), 755–758.
- [6] BUSCHART, R. J.  
*Electrical and instrumentation safety for chemical processes*.  
Springer Science & Business Media, 2012.
- [7] CARABELLI, R., AND KELLERMAN, W.  
Phantom limb pain: relief by application of TENS to contralateral extremity.  
*Archives of Physical Medicine and Rehabilitation* 66, 7 (1985), 466–467.
- [8] CAUNA, N.  
Nerve supply and nerve endings in meissner’s corpuscles.  
*Developmental Dynamics* 99, 2 (1956), 315–350.
- [9] CAUNA, N., AND MANNAN, G.  
Organization and development of the preterminal nerve pattern in the palmar digital tissues of man.

## REFERENCES

---

- Journal of Comparative Neurology* 117, 3 (1961), 309–327.
- [10] CHEN, K., REN, L., CHEN, Z., PAN, C., ZHOU, W., AND JIANG, L.  
Fabrication of micro-needle electrodes for bio-signal recording by a magnetization-induced self-assembly method.  
*Sensors (Basel)* 16, 9 (Sep 2016).
- [11] CHIU, S., RITCHIE, J., ROGART, R., AND STAGG, D.  
A quantitative description of membrane currents in rabbit myelinated nerve.  
*The Journal of Physiology* 292, 1 (1979), 149–166.
- [12] CHOUVARDAS, V., MILIOU, A., AND HATALIS, M.  
Tactile displays: Overview and recent advances.  
*Displays* 29, 3 (2008), 185–194.
- [13] DANDEKAR, K., RAJU, B. I., AND SRINIVASAN, M. A.  
3-D Finite-Element Models of Human and Monkey Fingertips to Investigate the Mechanics of Tactile Sense .  
*Journal of Biomechanical Engineering* 125, 5 (10 2003), 682–691.
- [14] DELMAS, P., HAO, J., AND RODAT-DESPOIX, L.  
Molecular mechanisms of mechanotransduction in mammalian sensory neurons.  
*Nature Reviews Neuroscience* 12, 3 (2011), 139–153.
- [15] DESIGN, D.  
Tactor, 2019.
- [16] DONG, Y., MIHALAS, S., KIM, S. S., YOSHIOKA, T., BENSMAIA, S., AND NIEBUR, E.  
A simple model of mechanotransduction in primate glabrous skin.  
*Journal of Neurophysiology* 109, 5 (03 2013), 1350–1359.
- [17] DUBBS, A. J., SEILER, B. A., AND MAGNASCO, M. O.  
A fast  $\mathcal{L}_p$  spike alignment metric.  
*Neural Computation* 22, 11 (2010), 2785–2808.
- [18] FRANKENHAEUSER, B., AND HUXLEY, A.  
The action potential in the myelinated nerve fibre of *xenopus laevis* as computed on the basis of voltage clamp data.  
*The Journal of Physiology* 171, 2 (1964), 302–315.
- [19] FREEMAN, A. W., AND JOHNSON, K. O.  
Cutaneous mechanoreceptors in macaque monkey: temporal discharge patterns evoked by vibration, and a receptor model.  
*The Journal of Physiology* 323 (Feb 1982), 21–41.

- [20] FREEMAN, A. W., AND JOHNSON, K. O.  
A model accounting for effects of vibratory amplitude on responses of cutaneous mechanoreceptors in macaque monkey.  
*The Journal of Physiology* 323 (Feb 1982), 43–64.
- [21] FRIEDLANDER, G. D.  
Electricity in hospitals: elimination of lethal hazards.  
*IEEE Spectrum* 8, 9 (1971), 40–51.
- [22] GERMANI, M., MENGONI, M., AND PERUZZINI, M.  
Electro-tactile device for material texture simulation.  
*International Journal of Advanced Manufacturing Technology* 68 (2013), 2185–2203.
- [23] GESCHEIDER, G. A.  
*Psychophysics: the fundamentals*.  
Psychology Press, 2013.
- [24] GRÜN, S., DIEMANN, M., GRAMMONT, F., RIEHLE, A., AND AERTSEN, A.  
Detecting unitary events without discretization of time.  
*Journal of Neuroscience Methods* 94, 1 (1999), 67 – 79.
- [25] HALATA, Z., GRIM, M., AND BAUMAN, K. I.  
Friedrich sigmund merkel and his “merkel cell”, morphology, development, and physiology:  
Review and new results.  
*The Anatomical Record Part A: Discoveries in Molecular, Cellular, and Evolutionary Biology*  
271A, 1 (2003), 225–239.
- [26] HALL, J. E.  
*Guyton and Hall textbook of medical physiology*.  
Elsevier Health Sciences, 2010.
- [27] HANSSON, P., AND EKBLÖM, A.  
Transcutaneous electrical nerve stimulation (TENS) as compared to placebo TENS for the  
relief of acute oro-facial pain.  
*Pain* 15, 1 (1983), 157–165.
- [28] HARVEY, L.  
Parameter estimation of signal detection models: Rscoreplus user’s manual (version 5.9.8),  
2018.
- [29] HASGALL, P., NEUFELD, E., GOSSELIN, M., KLINGENBÖCK, A., AND KUSTER, N.  
IT’IS Database for thermal and electromagnetic parameters of biological tissues, 2017.

## REFERENCES

---

- [30] HE, B.  
*Modeling & Imaging of Bioelectrical Activity: Principles and Applications.*  
Bioelectric Engineering. Springer US, 2010, p. 308.
- [31] HERRAIZ, C., TOLEDANO, A., AND DIGES, I.  
Trans-electrical nerve stimulation (TENS) for somatic tinnitus.  
*Progress in Brain Research 166* (2007), 389–553.
- [32] HODGKIN, A. L., AND HUXLEY, A. F.  
A quantitative description of membrane current and its application to conduction and excitation in nerve.  
*The Journal of Physiology 117*, 4 (1952), 500–544.
- [33] HOSHI, T., TAKAHASHI, M., IWAMOTO, T., AND SHINODA, H.  
Noncontact tactile display based on radiation pressure of airborne ultrasound.  
*IEEE Transactions on Haptics 3*, 3 (July 2010), 155–165.
- [34] HOUGHTON, C., AND VICTOR, J.  
*Measuring Representational Distances: The Spike-Train Metrics Approach.*  
Computational neuroscience. MIT Press, 2012, pp. 391–416.
- [35] JOHANSSON, R. S., AND VALLBO, A.  
Tactile sensibility in the human hand: relative and absolute densities of four types of mechanoreceptive units in glabrous skin.  
*The Journal of Physiology 286*, 1 (1979), 283–300.
- [36] KACZMAREK, K. A.  
The tongue display unit (TDU) for electrotactile spatiotemporal pattern presentation.  
*Scientia Iranica 18*, 6 (2011), 1476–1485.
- [37] KACZMAREK, K. A., TYLER, M. E., BRISBEN, A. J., AND JOHNSON, K. O.  
The afferent neural response to electrotactile stimuli: preliminary results.  
*IEEE Transactions on Rehabilitation Engineering 8*, 2 (2000), 268–270.
- [38] KACZMAREK, K. A., TYLER, M. E., OKPARA, U. O., AND HAASE, S. J.  
Interaction of perceived frequency and intensity in fingertip electrotactile stimulation: Dissimilarity ratings and multidimensional scaling.  
*IEEE Transactions on Neural Systems and Rehabilitation Engineering 25*, 11 (Nov 2017), 2067–2074.
- [39] KAJIMOTO, H.  
Electrotactile display with real-time impedance feedback using pulse width modulation.  
*IEEE Transactions on Haptics 5*, 2 (April 2012), 184–188.

- [40] KAJIMOTO, H., KAWAKAMI, N., MAEDA, T., AND TACHI, S.  
Tactile feeling display using functional electrical stimulation.  
In *Proc. 1999 ICAT* (1999), p. 133.
- [41] KAJIMOTO, H., KAWAKAMI, N., MAEDA, T., AND TACHI, S.  
Electro-tactile display with tactile primary color approach.  
*Graduate School of Information and Technology, The University of Tokyo* (2004).
- [42] KAJIMOTO, H., KAWAKAMI, N., AND TACHI, S.  
Optimal design method for selective nerve stimulation and its application to electrocutaneous display.  
In *Proceedings 10th Symposium on Haptic Interfaces for Virtual Environment and Teleoperator Systems (HAPTICS)* (2002), IEEE, pp. 303–310.
- [43] KAJIMOTO, H., SUZUKI, M., AND KANNO, Y.  
Hamsatouch: Tactile vision substitution with smartphone and electro-tactile display.  
In *Proceedings of the Extended Abstracts of the 32Nd Annual ACM Conference on Human Factors in Computing Systems* (New York, NY, USA, 2014), CHI EA '14, ACM, pp. 1273–1278.
- [44] KAPLAN, B., RABINERSON, D., LURIE, S., BAR, J., KRIESER, U., AND NERI, A.  
Transcutaneous electrical nerve stimulation (TENS) for adjuvant pain-relief during labor and delivery.  
*International Journal of Gynecology & Obstetrics* 60, 3 (1998), 251–255.
- [45] KIM, L. H., CASTILLO, P., FOLLMER, S., AND ISRAR, A.  
Vps tactile display: Tactile information transfer of vibration, pressure, and shear.  
*Proc. ACM Interact. Mob. Wearable Ubiquitous Technol.* 3, 2 (June 2019), 51:1–51:17.
- [46] KIM, S.-C., KIM, C. H., YANG, T.-H., YANG, G.-H., KANG, S.-C., AND KWO, D.-S.  
Salt: Small and lightweight tactile display using ultrasonic actuators.  
In *RO-MAN 2008 - The 17th IEEE International Symposium on Robot and Human Interactive Communication* (Aug 2008), pp. 430–435.
- [47] KIM, S. S., SRIPATI, A. P., AND BENSMAIA, S. J.  
Predicting the timing of spikes evoked by tactile stimulation of the hand.  
*Journal of Neurophysiology* 104, 3 (2010), 1484–1496.
- [48] KINGDOM, F., AND PRINS, N.  
*Psychophysics: A Practical Introduction*.  
Academic Press, 2010.

## REFERENCES

---

- [49] KJÆR, B. .  
Product data: Power amplifier type 2718, 2011.
- [50] KJÆR, B. .  
Product data: Mini-shaker type 4810, 2014.
- [51] KOMURASAKI, S., KAJIMOTO, H., AND ISHIZUKA, H.  
Fundamental perceptual characterization of an integrated tactile display with electrovi-  
bration and electrical stimuli.  
*Micromachines* 10, 5 (May 2019), 301.
- [52] KRAMER, O.  
*Genetic Algorithm Essentials*, 1st ed.  
Springer Publishing Company, Incorporated, 2017.
- [53] KRUGER, L., FRIEDMAN, M., AND CARTERETTE, E.  
*Pain and Touch*.  
Handbook of Perception and Cognition. Elsevier Science, 1996, ch. 2. The Psychophysics of  
Tactile Perception and Its Peripheral Physiological Basis.
- [54] KUHN, A.  
*Modeling transcutaneous electrical stimulation*.  
PhD thesis, Diss., Eidgenössische Technische Hochschule ETH Zürich, Nr. 17948, 2008,  
2008.
- [55] KUHN, A., KELLER, T., LAWRENCE, M., AND MORARI, M.  
A model for transcutaneous current stimulation: simulations and experiments.  
*Medical & Biological Engineering & Computing* 47, 3 (2009), 279–289.
- [56] KUHN, A., KELLER, T., LAWRENCE, M., AND MORARI, M.  
The influence of electrode size on selectivity and comfort in transcutaneous electrical  
stimulation of the forearm.  
*IEEE Transactions on Neural Systems and Rehabilitation Engineering* 18, 3 (2010), 255–  
262.
- [57] LEDERMAN, S. J., AND KLATZKY, R. L.  
Haptic perception: A tutorial.  
*Attention, Perception, & Psychophysics* 71, 7 (Oct 2009), 1439–1459.
- [58] LEE, C.-H., AND JANG, M.-G.  
Virtual surface characteristics of a tactile display using magneto-rheological fluids.  
*Sensors* 11, 3 (2011), 2845–2856.

- [59] LEE, J., AND LEE, G.  
Designing a non-contact wearable tactile display using airflows.  
In *Proceedings of the 29th Annual Symposium on User Interface Software and Technology*  
(New York, NY, USA, 2016), UIST '16, ACM, pp. 183–194.
- [60] LUCE, R. D., AND GALANTER, E.  
Psychophysical scaling.  
*Handbook of mathematical psychology 1* (1963), 245–307.
- [61] M. J. PETERS, G. STINSTRA, M. H.  
Estimation of the electrical conductivity of human tissue.  
*Electromagnetics 21*, 7-8 (2001), 545–557.
- [62] MACMILLAN, N. A., AND CREELMAN, C. D.  
*Detection theory: A user's guide*.  
Psychology press, 2004.
- [63] MAINEN, Z., AND SEJNOWSKI, T.  
Reliability of spike timing in neocortical neurons.  
*Science 268*, 5216 (1995), 1503–1506.
- [64] MCNEAL, D. R.  
Analysis of a model for excitation of myelinated nerve.  
*IEEE Transactions on Biomedical Engineering*, 4 (1976), 329–337.
- [65] MIZUHARA, R., TAKAHASHI, A., AND KAJIMOTO, H.  
Enhancement of subjective mechanical tactile intensity via electrical stimulation.  
In *Proceedings of the 10th Augmented Human International Conference 2019* (New York,  
NY, USA, 2019), AH2019, ACM, pp. 9:1–9:5.
- [66] NARA, T., TAKASAKI, M., MAEDA, T., HIGUCHI, T., ANDO, S., AND TACHI, S.  
Surface acoustic wave tactile display.  
*IEEE Computer Graphics and Applications 21*, 6 (Nov 2001), 56–63.
- [67] PELLI, D. G., AND FARELL, B.  
Psychophysical methods.  
*Handbook of optics 1* (1995), 29–21.
- [68] PHILLIPS, J. R., AND JOHNSON, K. O.  
Tactile spatial resolution. iii. a continuum mechanics model of skin predicting mechanore-  
ceptor responses to bars, edges, and gratings.  
*Journal of Neurophysiology 46*, 6 (1981), 1204–1225.  
PMID: 7320743.



## REFERENCES

---

- [69] PHILPOTT, M., AND SUMMERS, I. R.  
Surface-Roughness-Based Virtual Textiles: Evaluation Using a Multi-Contactor Display.  
*IEEE Transactions on Haptics*, 2 (2015), 240–244.
- [70] PROVITERA, V., NOLANO, M., PAGANO, A., CAPORASO, G., STANCANELLI, A., AND SANTORO, L.  
Myelinated nerve endings in human skin.  
*Muscle & Nerve: Official Journal of the American Association of Electrodiagnostic Medicine* 35, 6 (2007), 767–775.
- [71] QUEK, Z. F., SCHORR, S. B., NISKY, I., PROVANCHER, W. R., AND OKAMURA, A. M.  
Sensory substitution and augmentation using 3-degree-of-freedom skin deformation feedback.  
*IEEE Transactions on Haptics* 8, 2 (April 2015), 209–221.
- [72] RANCK JR, J. B.  
Which elements are excited in electrical stimulation of mammalian central nervous system: a review.  
*Brain Research* 98, 3 (1975), 417–440.
- [73] RATTAY, F.  
Modeling the excitation of fibers under surface electrodes.  
*IEEE Transactions on Biomedical Engineering* 35, 3 (1988), 199–202.
- [74] RATTAY, F.  
*Electrical nerve stimulation*.  
Springer, 1990, ch. 7. Extracellular stimulation of fibers.
- [75] REILLY, J. P.  
*Applied bioelectricity: from electrical stimulation to electropathology*.  
Springer Science & Business Media, 2012, pp. 87 – 88.
- [76] SAUNDERS, F.  
Recommended procedures for electrocutaneous displays.  
In *Functional electrical stimulation: Applications in neural prostheses*. Marcel Dekker, 1977, pp. 303–309.
- [77] SAUNDERS, F. A.  
Information transmission across the skin: High-resolution tactile sensory aids for the deaf and the blind.  
*International Journal of Neuroscience* 19, 1-4 (1983), 21–28.

- [78] SCHANING, M. A., AND KACZMAREK, K. A.  
A high-voltage bipolar transconductance amplifier for electrotactile stimulation.  
*IEEE Transactions on Biomedical Engineering* 55, 10 (Oct 2008), 2433–2443.
- [79] SCHWARZ, J. R., AND EIKHOF, G.  
Na currents and action potentials in rat myelinated nerve fibres at 20 and 37 c.  
*Pflügers Archiv* 409, 6 (1987), 569–577.
- [80] SMIT, J., HANEKOM, T., AND HANEKOM, J. J.  
Predicting action potential characteristics of human auditory nerve fibres through modification of the Hodgkin-Huxley equations.  
*South African Journal of Science* 104, 7-8 (2008), 284–292.
- [81] SNELL, R. S.  
*Clinical anatomy by regions*.  
Lippincott Williams and Wilkins, 2011.
- [82] SRIPATI, A. P., BENSMAIA, S. J., AND JOHNSON, K. O.  
A continuum mechanical model of mechanoreceptive afferent responses to indented spatial patterns.  
*Journal of Neurophysiology* 95, 6 (2006), 3852–3864.
- [83] STRONG, R. M., AND TROXEL, D. E.  
An electrotactile display.  
*IEEE Transactions on Man-Machine Systems* 11, 1 (1970), 72–79.
- [84] STÜBER, H.  
Electrical field model for transcutaneous electrical nerve stimulation.  
Master’s thesis, Technische Universität München, 2014.
- [85] SUMMERS, I. R., AND CHANTER, C. M.  
A broadband tactile array on the fingertip.  
*The Journal of the Acoustical Society of America* 112, 5 (2002), 2118–2126.
- [86] TAI, C., DE GROAT, W. C., AND ROPPOLO, J. R.  
Simulation of nerve block by high-frequency sinusoidal electrical current based on the Hodgkin-Huxley model.  
*IEEE Transactions on Neural Systems and Rehabilitation Engineering* 13, 3 (2005), 415–422.
- [87] TALBOT, W. H., DARIAN-SMITH, I., KORNHUBER, H. H., AND MOUNTCASTLE, V. B.  
The sense of flutter-vibration: comparison of the human capacity with response patterns of mechanoreceptive afferents from the monkey hand.

## REFERENCES

---

- Journal of Neurophysiology* 31, 2 (1968), 301–334.
- [88] TEZUKA, M., KITAMURA, N., TANAKA, K., AND MIKI, N.  
Presentation of various tactile sensations using micro-needle electrotactile display.  
*PLOS ONE* 11, 2 (02 2016), 1–14.
- [89] VAN BOXTEL, A.  
Skin resistance during square-wave electrical pulses of 1 to 10 ma.  
*Medical and Biological Engineering and Computing* 15, 6 (1977), 679–687.
- [90] VAN ROSSUM, M.  
A novel spike distance.  
*Neural Computation* 13 (04 2001), 751–763.
- [91] VICTOR, J. D., AND PURPURA, K. P.  
Nature and precision of temporal coding in visual cortex: a metric-space analysis.  
*Journal of Neurophysiology* 76, 2 (1996), 1310–1326.
- [92] VICTOR, J. D., AND PURPURA, K. P.  
Metric-space analysis of spike trains: theory, algorithms and application.  
*Network: Computation in Neural Systems* 8, 2 (01 1997), 127–164.
- [93] WAGNER, H., BRILL, S., KEMPTER, R., AND CARR, C. E.  
Microsecond precision of phase delay in the auditory system of the barn owl.  
*J Neurophysiol* 94, 2 (Aug 2005), 1655–1658.
- [94] WESOŁOWSKI, S., CONTRERAS, R. J., AND WU, W.  
A new framework for euclidean summary statistics in the neural spike train space.  
*Ann. Appl. Stat.* 9, 3 (09 2015), 1278–1297.
- [95] WHITLEY, D.  
A genetic algorithm tutorial.  
*Statistics and Computing* 4, 2 (Jun 1994), 65–85.
- [96] WILLIS, W., AND COGGESHALL, R.  
*Sensory Mechanisms of the Spinal Cord: Volume 1 Primary Afferent Neurons and the Spinal Dorsal Horn.*  
Sensory Mechanisms of the Spinal Cord. Springer US, 2004, ch. 1. Introduction.
- [97] WILSON, B.  
Current mirrors, amplifiers and dumpers.  
*Wireless world* 87 (1981), 47–48.

- 
- [98] WOLFSON, A. B., HENDEY, G. W., LING, L. J., ROSEN, C. L., SCHAIDER, J. J., AND SHARIEFF, G. Q.  
*Harwood-Nuss' clinical practice of emergency medicine.*  
Lippincott Williams and Wilkins, 2012.
- [99] YEM, V., AND KAJIMOTO, H.  
Comparative evaluation of tactile sensation by electrical and mechanical stimulation.  
*IEEE Transactions on Haptics* 10, 1 (2017), 130–134.
- [100] YEM, V., AND KAJIMOTO, H.  
Combination of cathodic electrical stimulation and mechanical damped sinusoidal vibration to express tactile softness in the tapping process.  
In *2018 IEEE Haptics Symposium (HAPTICS)* (March 2018), pp. 84–88.
- [101] YOSHIMOTO, S., KURODA, Y., IMURA, M., AND OSHIRO, O.  
Material roughness modulation via electrotactile augmentation.  
*IEEE Transactions on Haptics* 8, 2 (April 2015), 199–208.
- [102] ZELENÁ, J.  
*Nerves and mechanoreceptors: the role of innervation in the development and maintenance of mammalian mechanoreceptors.*  
Springer Science & Business Media, 1994.
- [103] ZENKER, W., AND NEUHUBER, W. L.  
*The Primary afferent neuron: a survey of recent morpho-functional aspects.*  
Springer Science & Business Media, 2012.

